Ph.D. Dissertation of Health Science and Technology

A Deep Learning Approach for CT-free Organ Quantification and Tumour Dosimetry with SPECT/CT

-CT-free organ quantification and tumour dosimetry-

SPECT/CT 영상을 이용한 딥러닝 기반 CT 미사용 장기 정량화 및 종양 선량 측정

February 2025

Graduate School of Convergence Science and Technology
Seoul National University
Health Science and technology Major

Kyounghyoun Kwon

A Deep Learning Approach for CT-free Organ Quantification and Tumour Dosimetry with SPECT/CT

-CT-free organ quantification and tumour dosimetry-

Won Woo Lee

Submitting a Ph.D. Dissertation of
Health Science and Technology

February 2025
Graduate School of Convergence Science and Technology
Seoul National University
Health Science and technology Major

Kyounghyoun Kwon

Confirming the Ph.D. Dissertation written by
Kyounghyoun Kwon
February 2025

Chair	Jae Sung Lee (Seal)
Vice Chair	Won Woo Lee (Seal)
Examiner	Jae Hoon Moon (Seal)
Examiner	Yoo Sung Song (Seal)
Examiner	Wonmo Sung (Seal)

Abstract

Introduction: Single-photon emission computed tomography/computed tomography (SPECT/CT) is a promising nuclear medicine imaging tool for the accurate quantification of radioactivity in vivo and tumour dosimetry. Recent advancements in SPECT/CT technology have enabled highly accurate and reliable measurements of %injected dose, standardized uptake value, and radioactivity concentration (μCi/g). These parameters are valuable for both diagnosis and therapy. In this study, we present two diagnostic studies and one I-131-related therapeutic study. The diagnostic studies focus on deep-learning-based attenuation correction (AC) and organ segmentation, while the therapeutic study aims to enable personalized treatment planning for radioactive iodine (RAI).

Method and Result: We developed the networks, using thyroid SPECT/CT, to generate synthetic attenuation maps (μ-maps) and enable automatic thyroid segmentation. These networks were trained using primary emission SPECT and scattering SPECT for μ-map generation, followed by the use of generated μ-maps and primary emission SPECT for automatic thyroid segmentation. The %uptake in the thyroid, a critical parameter of assessing functional thyroid diseases, was derived using primary emission SPECT and scattering SPECT as input, effectively eliminating the need for CT and achieving CT-free SPECT. In the second part, we optimized the AC process for CT-free SPECT in kidney SPECT/CT, which measures the %uptake in the kidneys. Performance enhancements were achieved through logarithmic maximum normalization, gradient difference loss optimization, and conducting nearest-neighbor interpolation. Lastly, we investigated I-131 pre-therapeutic SPECT/CT. Blood pool I-131 radioactivity measured by SPECT/CT corresponded closely with blood sample gamma counting. Blood absorbed dose obtained through Monte-Carol simulation shows similar trends with conventional method. Tumour I-131 radioactivity concentrations were directly converted to absorbed dose rates. Therefore, pre-therapeutic planning of RAI administration guided by the SPECT/CT demonstrated promising potential.

Conclusion: SPECT/CT is a reliable and accurate imaging modality for quantifying radioactivity in vivo. Deep-learning-based CT-free SPECT holds promise as diagnostic approach by reducing unnecessary radiation exposure to patients. Additionally, pre-therapeutic SPECT/CT may provide valuable insights into the therapeutic efficacy of RAI administration for advanced thyroid cancer.

Keyword : Quantitative SPECT/CT, Deep learning, Synthetic μ-map, Attenuation correction, Organ segmentation, I-131 therapy, Tumour absorbed dose

Student Number : 2021-33651

CONTENTS

LIST OF TABLES

LIST OF FIGURES

Chapter 1. Introduction

Quantitative single-photon emission computed tomography / computed tomography (SPECT/CT) is a hybrid imaging technique that simultaneously provides functional and structural imaging. It is widely used in medical diagnostics and treatment planning by combining the strengths of both SPECT and CT for more precise evaluations. Currently, quantitative SPECT is being actively studied in various conditions, including bone/articular (*1-6*), parathyroid (*7*), kidney (*8,9*), salivary gland disease (*10*), and Monte-Carlo simulation for dosimetry (*10*).

SPECT uses radioactive tracers to detect gamma radiation emitted from the body. It primarily provides functional imaging, enabling the assessment of metabolic activity and cellular function in specific tissues or organs. A radioactive isotope is injected into the patient, and its distribution is measured to generate images. The tracer accumulates in specific organs, allowing the visualization of functional changes in those areas.

CT, on the other hand, is an imaging technique that uses X-rays and computational technology to create cross-sectional images of the body. It provides detailed anatomical information and plays a critical role in SPECT attenuation correction (AC) and organ segmentation (OS). Furthermore, CT enables the estimation of tissue density, which is essential for accurate AC and the precise characterization of geometry in Monte Carlo simulations. This capability is crucial for improving the accuracy of dose calculations and enhancing the reliability of simulation results. As a result, CT is indispensable in refining simulations used for both treatment planning and diagnostic assessments. However, CT has its limitations, including radiation exposure, which increases the risk of adverse health effects, and the time-consuming process of OS using CT images.

Recent advancements in deep learning have made it possible to perform CT-free AC and OS with remarkable accuracy. Deep learning algorithms, particularly convolutional neural networks (CNNs), can now generate synthetic attenuation maps (μ-maps) directly from SPECT images and perform organ segmentation using these synthetic μ-maps. This approach reduces radiation exposure and significantly decreases the time and resources required for organ segmentation.

As the first topic, we utilized deep learning algorithms to eliminate the need for CT scans in AC by generating synthetic μ-maps (Chapters 2 and 3). Additionally, we demonstrate how deep learning automates organ segmentation, reducing the associated time and resources, ultimately enhancing both patient safety and operational efficiency (Chapter 2).

In I-131 radioiodine therapy for thyroid cancer, the European Association of Nuclear Medicine (EANM) dosimetry guidelines primarily focus on estimating blood

absorbed dose using blood gamma counting and whole-body planar imaging. However, these guidelines do not provide a method for estimating tumour absorbed dose.

As the second topic, we investigate a direct transformation equation that calculates tumour absorbed dose from integrated I-131 concentration (Chapter 4).

Chapter 2. CT-free quantitative SPECT for automatic evaluation of %thyroid uptake based on deep-learning

Background

Single-photon emission computed tomography/computed tomography (SPECT/CT) is a nuclear imaging technique that has evolved to generate accurate quantitative radionuclide information (*11*). Technetium-99m (Tc-99m) is one of the most widely used radionuclides. Currently, quantitative SPECT/CT, which employs Tc-99m, is being actively studied in various conditions, including bone/articular (*1-6*), parathyroid (*7*), kidney (*8,9*), and salivary gland diseases (*10,12*).

Tc-99m pertechnetate uptake in the thyroid gland has been accurately measured using same principle of quantitative SPECT/CT (*13*). Graves' disease (*14*), chronic thyroiditis (*15*), and autonomic functional thyroid nodules (*16*) were evaluated using quantitative thyroid SPECT/CT. However, several limitations exist in clinical application of thyroid SPECT/CT since the thyroid is one of the most sensitive organs to ionizing radiation. Therefore, nuclear imaging technique of Tc-99m thyroid uptake measurement can find a broader clinical use if CT is removed according to ALARA (as low as reasonably achievable) principle without compromising quantitative ability of thyroid SPECT/CT.

CT has two-fold application in quantitative thyroid SPECT/CT as follows: attenuation map (μ-map), crucial for attenuation correction of 140keV photons to accurately quantify Tc-99m thyroid uptake, and thyroid segmentation, which is necessary for automated thyroid uptake evaluation. Here, we developed convolutional neural networks (CNNs) that can remove CT from thyroid SPECT/CT. Specifically, this study aimed to develop a deep learning-based CT-free quantitative SPECT for %thyroid uptake measurement.

Materials and methods

Dataset

In this study, two datasets of thyroid SPECT/CT cases were used. The first SPECT/CT dataset (n = 298) was obtained between February 2016 and April 2020, and SPECT and CT covered same axial field of view (FOV) of 38 cm from the mid-skull to upper mediastinum with the thyroid in centre. The second SPECT/CT dataset (n = 352) was obtained between June 2020 and December 2021, and CT did not cover the full but partial axial FOV (approximately 1/2 to 2/3) of SPECT to reduce redundant radiation exposure. The demographic characteristics of the two datasets were comparable (Table 1.1). The clinical diagnosis, which was cause of thyroid SPECT/CT referral, was determined by a nuclear medicine physician (DGO) in consideration of thyroid function tests and medical records.

The first dataset was used for generation of synthetic μ-map (268 and 30 for training and validation, respectively), whereas the second dataset was employed for automatic thyroid segmentation (280 and 36 for training and validation, respectively). The remaining 36 cases in the second dataset were used for an internal verification test to validate both synthetic μ-map generation and automatic thyroid segmentation.

In addition to thyroid SPECT/CT, 29 salivary gland SPECT/CT cases were enrolled from the same hospital. The acquisition protocols for thyroid SPECT/CT and salivary SPECT/CT were similar, except for fasting state (no diet restriction vs. fasting for at least 2 h), Tc-99m pertechnetate activity (185 MBq vs. 555 MBq), and organ at the central FOV (thyroid vs. salivary glands). Salivary SPECT/CT cases were used as external verification tests for deep-learning algorithms trained by thyroid SPECT/CT.

The details of the 650 thyroid SPECT/CT cases within individual datasets based on the training and validation are shown in Tables 1.2 and 1.3. In addition, details of 29 salivary SPECT/CT cases are presented in Table 1.4.

Table 1.1. Detailed demographics of thyroid SPECT/CT cases with full CT for attenuation map generation (n = 298)

		For training (n = 268)	For validation (n = 30)	*P*-value
Age [years] (mean±std[a])		47.5 ± 15.1	51.6 ± 17.6	0.1724
Sex (male:female)		81:187	10:20	0.7263
Clinical diagnosis	Graves' disease/hyperthyroidism	156	18	0.0956
	Painless/subacute thyroiditis	88	8	
	SNG[b]/MNG[c]	11	4	
	Others	13	0	

a: standard deviation

b: single nodular goiter

c: multi-nodular goiter

Table 1.2. Detailed demographics of thyroid SPECT/CT cases with partial CT for automatic thyroid segmentation and internal verification (n = 352)

		For training (n = 280)	For validation (n = 36)	For internal verification (n = 36)	*P*-value
Age [years] (mean±std[a])		48.0 ± 15.6	46.0 ± 16.5	44.0 ± 14.9	0.2488
Sex (male:female)		77:203	11:25	11:25	0.8761
Clinical diagnosis	Graves' disease/hyperthyroidism	162	18	18	0.8073
	Painless/subacute thyroiditis	94	15	14	
	SNG[b]/MNG[c]	13	1	3	
	Others	11	2	1	

a: standard deviation,

b: single nodular goiter

c: multi-nodular goiter

Table 1.3. Detailed demographics of salivary SPECT/CT cases for external verification (n = 29)

		For external verification (n = 29)
Age [years] (mean±std[a])		53.1 ± 13.7
Sex (male:female)		11:18
Clinical diagnosis	Xerostomia	11
	Salivary gland tumour	7
	Head and neck cancer	9
	Others	2

a: standard deviation

Quantitative thyroid single-photon emission computed tomography/computed tomography (SPECT/CT) protocol

The preparation required no diet control. First, Tc-99m pertechnetate (185 MBq) was eluted from the Mo-99/Tc-99m generator (Unitech Technetium-99m generator, Samyoung Unitech) and was intravenously injected into the patients. Twenty minutes later, an anterior planar image was obtained for 1 min with neck extension. Immediately after planar image acquisition, SPECT and CT were consecutively performed without neck extension using SPECT/CT scanners (NMCT670 or NMCT670pro, GE) equipped with low-energy high-resolution collimators. The SPECT acquisition conditions were as follows: primary energy window peak at 140 keV (20% window of 126 keV–154 keV), scatter window peak at 120 keV (10% window of 115 keV–125 keV), and continuous mode acquisition for 1 min without body contour option. The acquisition zoom factor was set to 1.5. The CT acquisition parameters were as follows: tube voltage 120 kVp, tube current 30 mA, helical mode acquisition with detector collimation (16×1.25 = 20 mm), helical thickness 2.5 mm, table speed 37 mm/sec, table feed per rotation 18.75 mm/rot, tube rotation time 0.5 sec, and pitch 0.938:1.

The radioactivity and its measurement time were recorded before and after the injection of Tc-99m pertechnetate to quantify %thyroid uptake. We used a dose calibrator (CRC-15R, CAPINTEC) that had been daily calibrated using the National Institute of Standards and Technology traceable Co-57 source to measure radioactivity. Human experts who had been working on thyroid segmentation for 2 years (JHK and JHY) carefully segmented the thyroid on the CT images of the thyroid SPECT/CT upon dedicated quantitative software (Q.Metrix, GE), generating segmentation maps of the thyroid. System sensitivity of SPECT/CT scanners for Tc-99m was 152.5 cpm/μCi (from October 2015 to August 2017) and subsequently 151.8 cpm/μCi (since September 2017) for NMCT670, and 152.8 cpm/μCi (from December 2016 to August 2019) and then 149.3 cpm/μCi (since September 2019) for NMCT670pro.

Quantitative salivary gland SPECT/CT protocol

Patients fasted for at least 2 hours before SPECT/CT. Subsequently, Tc-99m pertechnetate (555 MBq), eluted from the Mo-99/Tc-99m generator (Unitech Technetium-99m generator, Samyoung Unitech), was intravenously injected. SPECT/CT was performed 20 min later. The same SPECT/CT scanners (NMCT670 or NMCT670pro, GE) equipped with LEHR collimators were used to perform a 1-min continuous mode SPECT without the body contour option. The primary peak and scatter peak energies were 140 keV with a 20% window (126 keV–154 keV) and 120 keV with a 10% window (115 keV–125 keV), respectively. The acquisition

zoom factor was set to 1.5. CT acquisition parameters were tube voltage 120 kVp, tube current 30 mA, detector collimation 16×1.25 = 20 mm, helical thickness 2.5 mm, table speed 37 mm/sec, table feed per rotation 18.75 mm/rot, tube rotation time 0.5 sec, and pitch 0.938:1. SPECT and CT acquisition/reconstruction conditions were exactly the same as thyroid SPECT/CT.

Study scheme

The overall scheme of study is shown in Figure 1. Two deep-learning algorithms were applied to μ-map generation (blue arrows) and automatic thyroid segmentation (red arrows). The SPECT input of the first deep-learning algorithm for μ-map generation was either only primary emission SPECT (p) or a combined primary emission and scattering SPECTs (ps). The label was original μ-map created with helical CT of SPECT/CT. The generated μ-map was used for attenuation correction (AC) of primary emission SPECT. In addition to AC, scatter correction (SC) and resolution recovery (RR) were applied, which resulted in quantitative ACSCRR SPECT (Q.VolumetrixMI, GE). The second deep-learning algorithm was trained for automatic thyroid segmentation using synthetic μ-map input with SPECT support. The SPECT support was investigated for p, ps, and CT-free quantitative ACSCRR SPECT. The label for automatic thyroid segmentation was the thyroid segmentation map drawn on CT by two human experts (JHK and JHY). Finally, the CT-free quantitative ACSCRR SPECT and automatically segmented thyroid map were combined to calculate the %thyroid uptake.

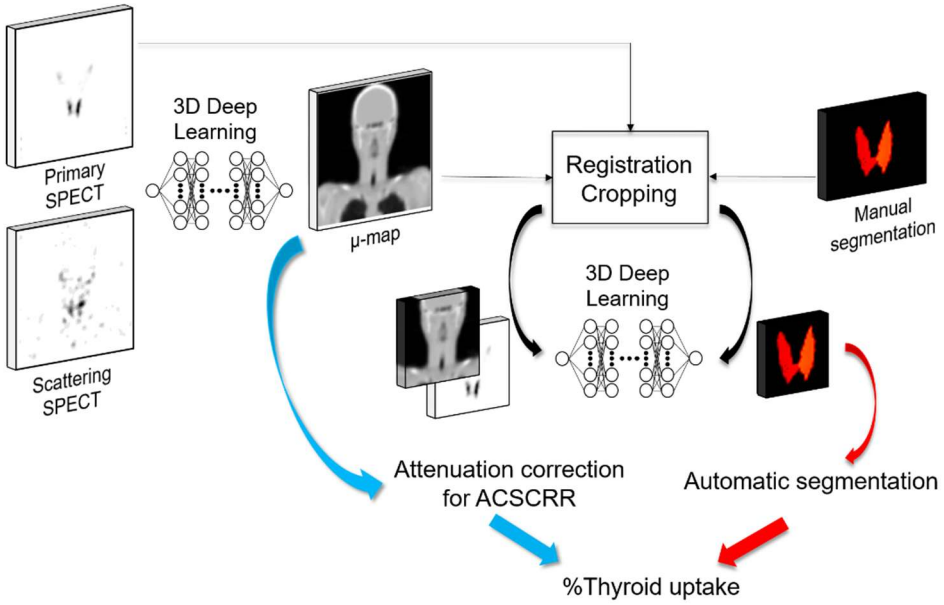

Figure 1.1. study scheme

Pre-processing for deep learning

The thyroid SPECT/CT acquisition protocol and quantification process have already been published in previous studies (*13-16*).

SPECT reconstruction processes were conducted using vendor-provided quantitative software (Q.VolumetrixMI, GE) and the ordered-subsets expectation-maximization (OSEM) iteration algorithm (4 iterations and 10 subsets). The matrix and voxel sizes were 128×128×128 and 2.95×2.95×2.95 mm^3, respectively, for the SPECT images. The primary emission and scattering SPECTs were not corrected for attenuation or scattering but rather for collimator-detector response (that is, resolution recovery, RR), resulting in NCRR SPECT. In addition, a post-reconstruction Butterworth low-pass filter (order of 10 and cutoff frequency of 0.48) was used for scattering SPECT to reduce statistical noise.

For a μ-map generation, primary emission and scattering SPECT images were normalized by the maximum of two SPECTs' summed images. The voxel value was set to 0 in case of a negative voxel value due to the post-reconstruction filter in scattering SPECT image. For automatic thyroid segmentation, synthetic μ-map and SPECT support were cropped from 128×128×128 to 64×64×64 to save training time and resources and subsequently normalized by maximum value to the input range of [0,1]. The manual thyroid segmentation map's initial matrix and voxel sizes were 256×256×slice and 1.47×1.47×1.47 mm^3, respectively, which were down-sampled to 128×128×128 and 2.95×2.95×2.95 mm^3 and subsequently cropped to 64×64×64 for consistency with the synthetic μ-map and SPECT support.

Network architecture and loss function for μ-map generation

We used a standard 3D U-Net with 64 initial neurons and 4 skip connections. The 3D U-Net learns end-to-end for μ-map generation between SPECTs (primary emission and scattering) and original μ-map. During the contraction path, 3×3×3 convolution blocks were applied, followed by 2×2×2 stride max-pooling. Individual 3×3×3 convolution blocks comprised two times 3×3×3 convolutions, instance normalization, and rectified linear unit activation. During the extraction path, 3×3×3 convolution blocks were followed by 2×2×2 up-convolution. Notably, the last 3×3×3 convolution block led to 1×1×1 convolution without an activation function (Figure 1.2).

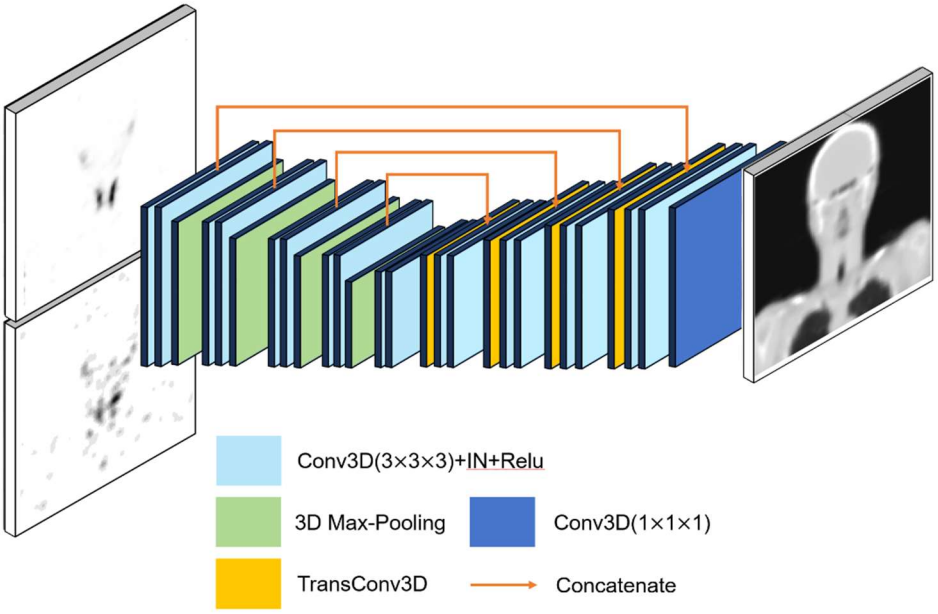

Figure 1.2. 3D U-Net architecture for the μ-map generation

The loss function for μ-map generation was defined as follows:

$$L(G(X),Y) = L_{error}(G(X,Y) + L_{GDL}(G(X),Y)$$

where *Y* is the target (that is, original CT-based μ-map) and *G(X)* are synthetic μ-maps generated from SPECT input X. L_{error} is either L_1 loss (that is, sum of the absolute differences between the target and generated) or L_2 loss (that is, sum of the squared differences between the target and generated). L_{GDL} is gradient difference loss (GDL) term for sharpening the generated μ-maps.

The L_1 and L_2 loss functions were defined as follows:

$$L_1 = \sum |G(X) - Y|$$

$$L_2 = \sum (G(X) - Y)^2$$

The gradient difference loss (GDL) term used to compensate for image blurring by L_2 loss effects is defined as follows:

$$L_{GDL} = \sum (|\nabla G(X)| - |\nabla Y|)^2$$

where ∇ is the image gradient operator.

Network architecture and loss function for automatic thyroid segmentation

A similar 3D U-Net was used for automatic thyroid segmentation. The 3D U-Net used batch normalization rather than instance normalization and had an additional softmax activation following the last 1×1×1 convolution (Figure 1.3). Since the right and left thyroid lobes were individually segmented, the loss function for automatic thyroid segmentation was a categorical cross-entropy (CCE) loss. The CCE loss was defined as follows:

$$CCE = \frac{1}{n}\sum_{i=1}^{n}[y_i\, log(\hat{y}_i) + (1 - y_i) log(1 - \hat{y}_i)]$$

where y_i is 0 or 1 as the ground truth, $\hat{y}_i$ is probability of a prediction, and n is number of classes in the segmentation model. Here, we used three classes: background, the left, and right thyroid.

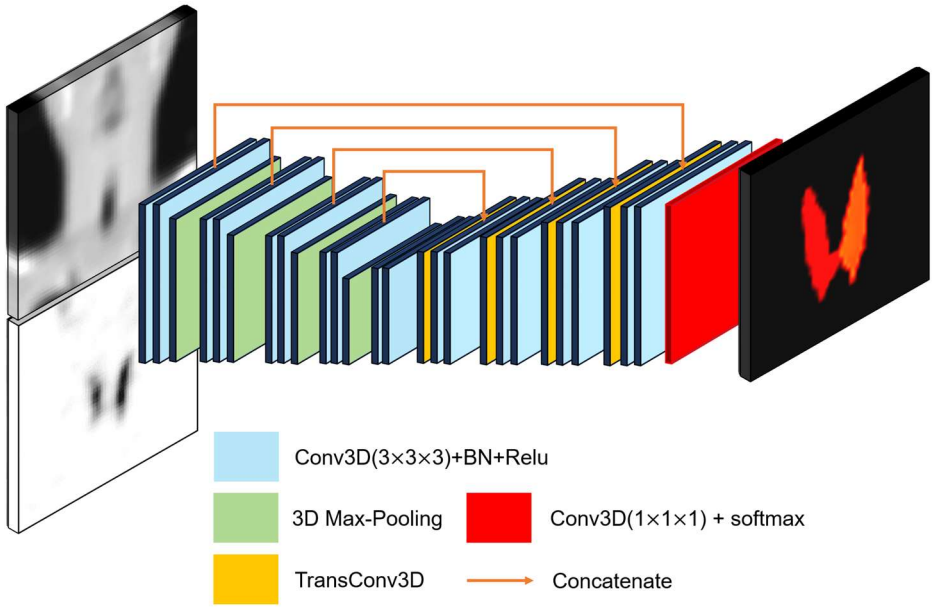

Figure 1.3. 3D U-Net for the automatic thyroid segmentation.

We implemented our networks using TensorFlow (*17*) and Keras framework (*18*).

Training hyper-parameters

Both μ-map generation and automatic thyroid segmentation used similar training hyper-parameters. The batch size was 8. Furthermore, an adaptive moment estimation optimizer was used. As the learning rate scheduler, the initial learning and exponential decay rates were 0.001 and 0.99, respectively. We also applied data

augmentation through flips. For μ-map generation, the SPECT input images were flipped along the x, y, and z axes, while, for automatic thyroid segmentation, the input images (synthetic μ-map and primary emission SPECT) were flipped along the x and z axes. The intended total number of epochs was 100, and early stopping was applied. The training time was approximately 15 min/epoch and 5 min/epoch for μ-map generation and automatic thyroid segmentation, respectively, with an AMD Ryzen7 5800X CPU and an RTX 3090 GPU.

Evaluation of outcomes

The attenuation coefficient has units of cm^{-1}, and the correlations of attenuation coefficients between the synthetic μ-map and original μ-map were evaluated as R^2, mean square error (MSE), and %normalized mean absolute error (%NMAE).

$$R^2 = 1 - \frac{\sum((G(X) - Y)^2}{\sum(Y - \bar{Y})^2}$$

$$MSE = \frac{1}{No.of\ \ Voxels}\sum((G(X) - Y)^2$$

$$\%NMAE = \frac{1}{No.of\ \ Voxels}\sum\frac{|G(X) - Y|}{max(Y) - min(Y)}$$

where Y is the target (i.e.). original μ-map), $\bar{Y}$ is the mean of Y, and G(X) is the synthetic μ-map from the SPECT input X.

The manual and automatic thyroid segmentation agreement was analysed using the Dice similarity coefficient (DSC). In addition, the thyroid volume difference (automatic thyroid volume – manual thyroid volume) was calculated, and the 95% Hausdorff distance was used to indicate surface contour difference. Finally, the %thyroid uptake of Tc-99m pertechnetate, the ultimate parameter of quantitative SPECT, was compared between CT-free thyroid SPECT (attenuation correction by synthetic μ-map and automatic thyroid segmentation) and conventional thyroid SPECT/CT (attenuation correction by original μ-map and manual thyroid segmentation).

Dice similarity coefficient (DSC) was defined as follows:

$$DSC(Y, Z) = \frac{2 \times |Y \cap Z|}{|Y| + |Z|}$$

where $Y \cap Z$ is the element-wise product of Y (manual segmentation) and Z

(automatic thyroid segmentation).

95% Hausdorff distance was defined as follows:

$$d_{H9}\ (Y,Z) = max(d_{YZ}, d_{ZY})$$

where d_{H95} is the 95th percentile of the maximum distance between the Y (manual segmentation map) and Z (automatic segmentation map).

Statistical analysis

Parametric analyses (paired t, unpaired t, and analysis-of-variance tests) were performed for continuous variables when Shapiro–Wilk test did not reject normal distribution features. Otherwise, non-parametric tests (ex. Wilcoxon rank-sum test) were performed. Furthermore, categorical variables were compared using chi-squared test. Statistical significance was set at $p < 0.05$. All analyses were performed using statistical software (MedCalc, version 20.110).

Results

µ-map generation

Among 298 thyroid SPECT/CT cases with full CT coverage, 268 and 30 were used for training and validation, respectively. There were no age, sex, or clinical diagnosis differences between the training and validation groups (Table 1.1). We tested different loss functions (L_1 + L_{GDL} vs. L_2 + L_{GDL}) and SPECT inputs (p vs. ps). Consequently, the 3D U-Net produced almost identical µ-maps as the original. Furthermore, applying the L_1 loss function and primary emission and scattering SPECTs (ps SPECTs) input yielded the highest R^2 and lowest MSE/%NMAE (Table 1.4). Therefore, the 3D U-Net trained with the L_1 loss function and ps SPECT inputs was subsequently used to generate the µ-map. Figure 1.4 shows the strong correlation between the ground truth (original µ-map) and the synthetic µ-map in one of the 30 validation cases.

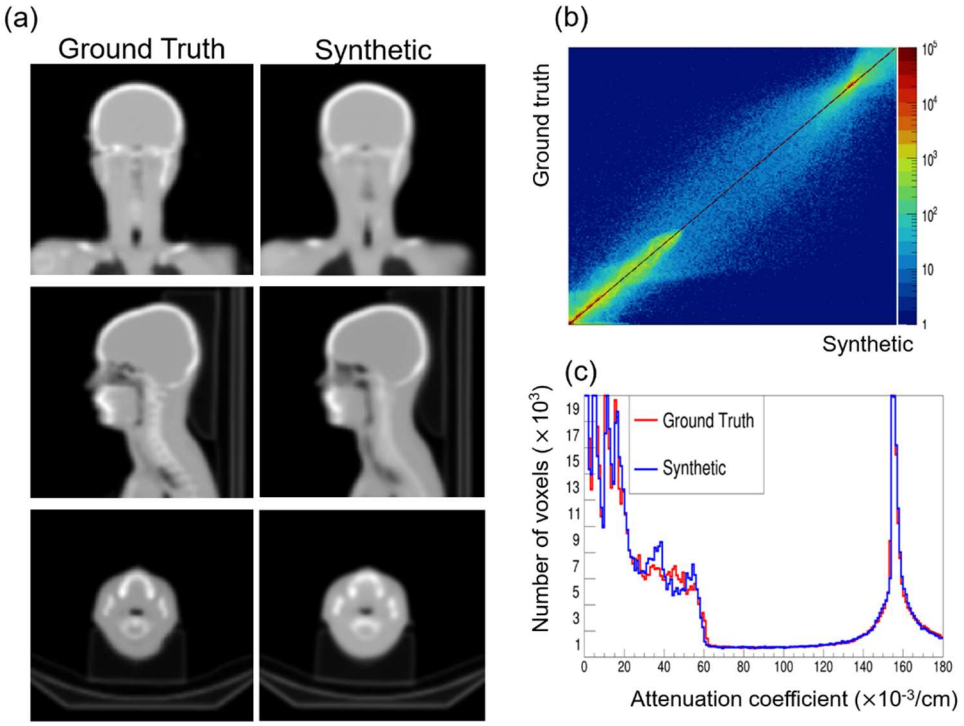

Figure 1.4 The generation of attenuation map (μ-map) by deep-learning. (a) The ground truth (original μ-map from CT) and synthetic μ-map. (b) Correlation plot and (c) Histogram of attenuation coefficients

Table 1.4. The correlations of attenuation coefficients between original attenuation map (μ-map) (ground truth) and synthetic μ-map (n = 30)

Metric	L_1[c]+L_{GDL}[i] loss with ps[g]			L_1+L_{GDL} loss with p[h]			L_2[d]+L_{GDL} loss with ps			L_2+L^{GDL} loss with p		
	R^2	MSE[e] ($\times 10^{-4}$)	%NMAE[f]	R^2	MSE($\times 10^{-4}$)	%NMAE	R^2	MSE($\times 10^{-4}$)	%NMAE	R^2	MSE($\times 10^{-4}$)	%NMAE
Mean	0.9721	0.9364	0.9994	0.9719	0.9391	1.0021	0.9712	0.9616	1.118	0.9708	0.9774	1.1426
STD[a]	0.0121	0.4249	0.2616	0.0127	0.4477	0.2744	0.0131	0.4494	0.272	0.0122	0.4263	0.2823
SER[b]	0.0022	0.0758	0.0478	0.0023	0.0817	0.0501	0.0024	0.0821	0.050	0.0022	0.0778	0.0516

a: standard deviation

b: standard error

c: the sum of the absolute differences between the target and generated

d: the sum of the squared differences between the target and generated

e: mean square error

f: normalized mean absolute error

g: primary emission SPECT + scattering SPECT

h: primary emission SPECT

i: Gradient difference loss

Automatic thyroid segmentation

Automatic thyroid segmentation was performed on 316 (280 and 36 for network training and validation, respectively) of the 352 thyroid SPECT/CT cases with partial CT coverage. No differences in age, sex, or clinical diagnosis between the training and validation groups were observed, which is similar to that in the μ-map generation (Table 1.3). We examined the synthetic μ-map input with SPECT support, which comprised p, ps, and CT-free quantitative ACSCRR SPECT.

The results showed that synthetic μ-map input with p was sufficient for the automatic thyroid segmentation with a large DSC of 0.7666, the least absolute thyroid volume difference of -0.7195 mL, and the shortest 95% Hausdorff distance of 9.4159 mm (Table 1.5). Both ps SPECTs and ACSCRR SPECT were inferior to p, particularly for the thyroid volume difference and 95% Hausdorff distance (Table 1.5). Both the hyperthyroidism and thyroiditis cases readily exhibited successful thyroid segmentation (Figure 1.5) Notably, the surface of the segmentation map became smooth through deep-learning. Furthermore, human experts spent approximately 40–60 min per case on manual thyroid segmentation, whereas automatic thyroid segmentation took less than a minute.

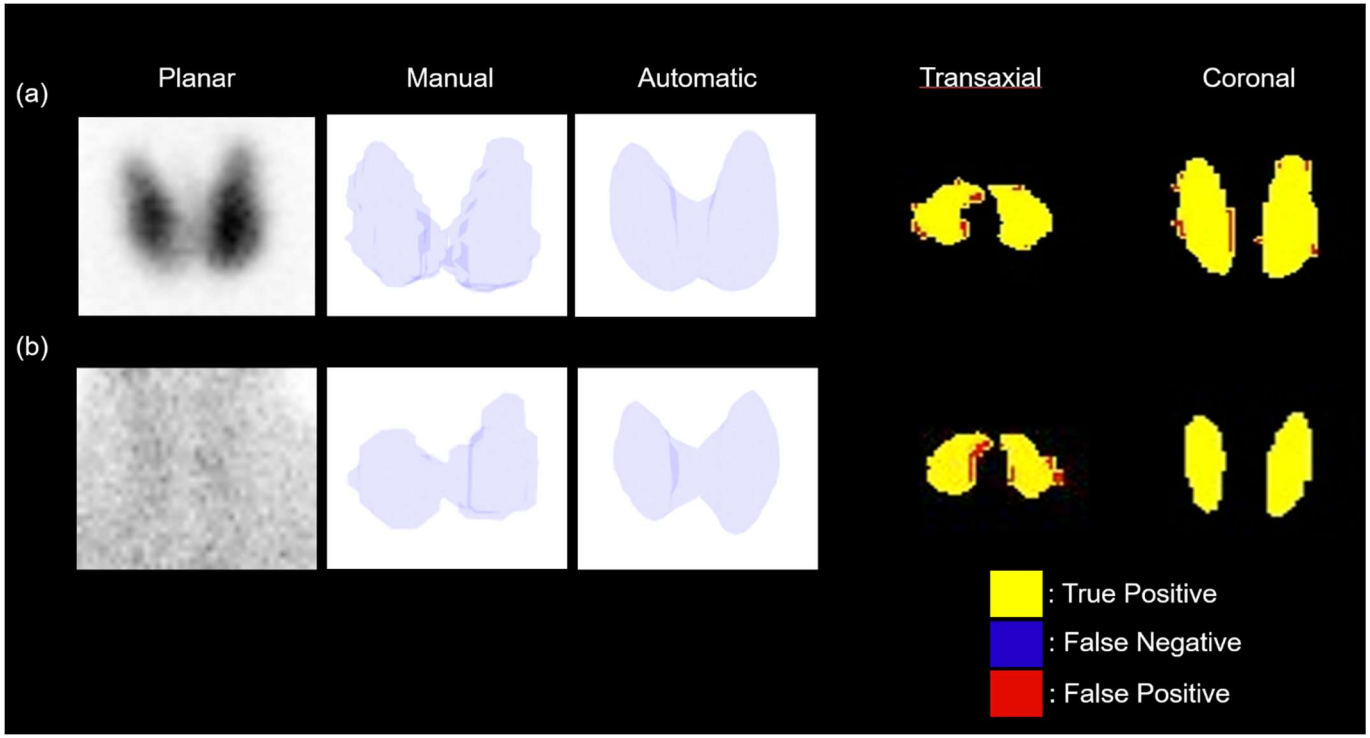

Figure 1.5. The automatic thyroid segmentation by deep-learning. (a) Patient with Graves' disease (F/32) with high uptake of Tc-99m pertechnetate. (b) Patient with subacute thyroiditis (F/25) with faint uptake of Tc-99m pertechnetate.

Table 1.5. The automatic thyroid segmentation outcomes according to SPECT input conditions, in addition to the attenuation map (μ-map) input (n = 36)

Metric	μ-map + p[g]			μ-map + ps[h]			μ-map + ACSCRR[f]			μ-map only		
	DSC[c]	VD[d] (mL)	95% HD[e] (mm)	DSC	VD (mL)	95% HD (mm)	DSC	VD (mL)	95% HD (mm)	DSC	VD (mL)	95% HD (mm)
Mean	0.7666	-0.7195	9.4159	0.7678	2.3447	10.0303	0.7690	1.4234	10.4414	0.7273	-5.2386	10.0499
STD[a]	0.0720	6.6606	3.6040	0.0767	6.9520	3.6237	0.0746	7.3629	5.5302	0.0667	8.0670	2.9156
SER[b]	0.0120	1.1101	0.6007	0.0128	1.1558	0.6039	0.0124	1.2271	0.9217	0.0111	1.3445	0.4859

a: standard deviation

b: standard error

c: Dice similarity coefficient

d: volume difference

e: Hausdorff distance

f: quantitative SPECT with attenuation correction, scatter correction, and resolution recovery

g: primary emission SPECT

h: primary emission SPECT + scattering SPECT

Internal verification

We recruited 36 thyroid SPECT/CT cases with partial CT that were not applied in the μ-map generation or automatic thyroid segmentation for the internal verification test (Table 1.2). Using the first deep-learning algorithm, the ps SPECTs generated μ-map. Subsequently, the generated μ-map and p SPECT produced thyroid segmentation map using the second deep-learning algorithm. Additionally, quantitative ACSCRR SPECT images were reconstructed using synthetic μ-map-based AC, SC, and RR. Then, the %thyroid uptake was calculated by applying the automatic thyroid segmentation map to quantitative ACSCRR SPECT. All processes were performed without CT assistance (that is, CT-free SPECT) (Figure 1.6). On the other hand, with CT assistance, the conventional quantitative ASCSRR SPECT was reconstructed using original μ-map-based AC, SC, and RR (SPECT/CT). Then, the thyroid was segmented by a human expert (JHK) on CT, and the ground truth %thyroid uptake was obtained.

As shown in Figure 1.4, the generated μ-maps were almost identical to those of the ground-truth, and the automatic thyroid segmentation was strongly correlated with the manual thyroid segmentation, as appreciated in Figure 1.5 and Table 1.5. Furthermore, the thyroid-specific ACSCRR SPECT counts were strongly correlated with each other (Table 1.6), and no significant difference was observed in the %thyroid uptake between CT-free SPECT and SPECT/CT (3.7722 ± 5.7348% vs. 3.6817 ± 5.5163%, p = 0.1088). Moreover, the % thyroid uptakes by both SPECTs were also strongly correlated, rarely biased, and easily differentiated thyroid diseases (Figure 1.7).

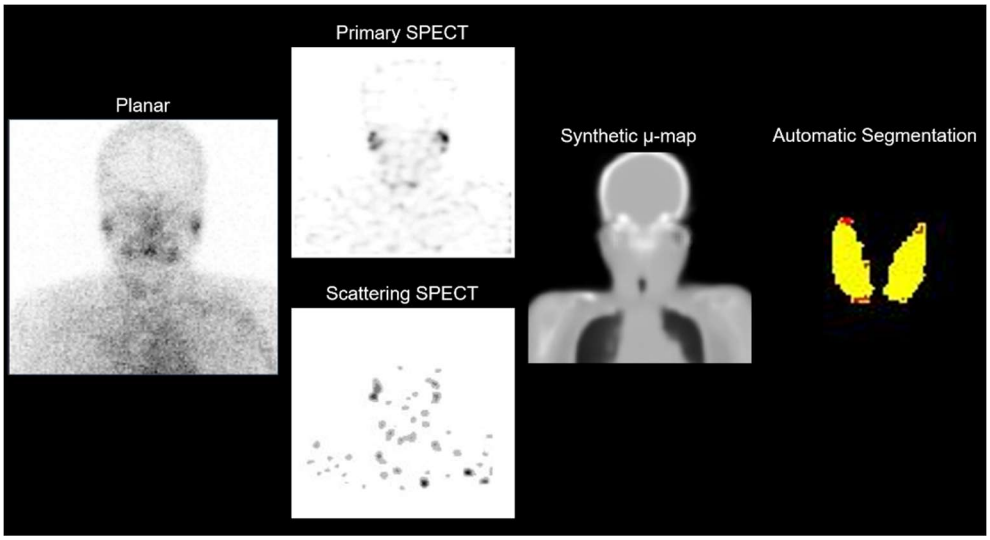

Figure 1.6. CT-free quantitative thyroid SPECT in a patient with thyroiditis (F/57). A planar scan shows a faint thyroid uptake. Primary emission SPECT and scattering SPECT were used for μ-map generation. Subsequently, the synthetic μ-map and primary emission SPECT were used for automatic thyroid segmentation. Yellow and red indicate true and false positives of the automatic thyroid segmentation, respectively, compared with manual segmentation. The %thyroid uptake by CT-free SPECT was 0.11%, whereas that by conventional SPECT/CT was 0.08%, consistent with the clinical condition of thyroiditis and faint uptake in the planar scan. The reported normal reference range was 0.78 ± 0.5%

Table 1.6. The internal verification of CT-free SPECT versus SPECT/CT (n = 36)

Metric	Thyroid segmentation			Thyroid-specific SPECT counts		
	DSC[c]	VD[d] (mL)	95% HD[e] (mm)	R^2	MSE[f] ($\times 10^{-4}$)	%NMAE[g]
Mean	0.7555	1.3713	12.0628	0.9632	0.0613	0.0024
STD[a]	0.0720	8.7320	6.4450	0.0258	0.1147	0.0007
SER[b]	0.0120	1.4553	1.0742	0.0043	0.0191	0.0001

a: standard deviation

b: standard error

c: Dice similarity score

d: volume difference

e: Hausdorff distance

f: mean square error

g: normalized mean absolute error

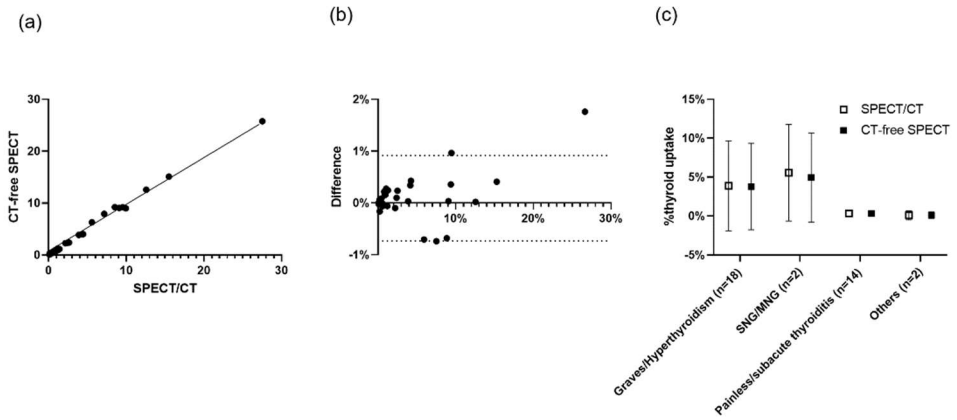

Figure 1.7. %thyroid uptake between CT-free SPECT and SPECT/CT as an internal verification test (n = 36 thyroid SPECT/CT). (a) The correlation is excellent with r = 0.9980, R^2 = 0.9959, and $p < 0.0001$. (b) The Bland–Altman plot shows no significant systemic deviation with bias = -0.09% point. (c) The %thyroid uptake readily differentiates the thyroid diseases. Data are mean ± standard deviation. The other two cases are drug-induced thyroiditis and lingual thyroid. The error bars for painless/subacute thyroiditis and the others are not obvious because of the limited size compared with the respective symbols. The normal reference range was reported as 0.78 ± 0.5% (*13*). SNG, single nodular goiter and NMG, multi-nodular goiter.

External verification

External verification tests were performed on the salivary gland SPECT/CT (n = 29) using the same radiotracer (Tc-99m pertechnetate) as in the thyroid SPECT/CT. Here, patients fasted for at least 2 hours, the injected radioactivity was three times as 555 MBq, and the salivary glands, instead of the thyroid, were located in the centre of the FOV. Otherwise, the acquisition protocol for the salivary SPECT/CT was the same as that for the thyroid SPECT/CT. Primary emission and scattering salivary SPECTs were reconstructed using the same reconstruction algorithms as the thyroid SPECT (Q.VolumetrixMI, GE) and were used as inputs to generate μ-maps (Figure 1.2). Then, the generated μ-maps were used with the primary emission salivary SPECT as input for automatic thyroid segmentation (Figure 1.3). Next, a human expert (JHK) manually segmented the thyroid from the CT of the salivary gland SPECT/CT. Quantitative ACSCRR SPECT images were reconstructed for CT-free SPECT and SPECT/CT.

Consequently, CT-free SPECT was successful in most salivary SPECT/CT cases through deep-learning which was trained using the thyroid SPECT/CT (Table 1.7 and Figure 1.8). The generated μ-map was identical to that shown in Figure 1.4, but automatic thyroid segmentation yielded a larger thyroid volume (26.252 ± 12.023 mL) than manual thyroid segmentation (18.772 ± 8.407 mL) ($p < 0.0001$). Accordingly, the %thyroid uptake on CT-free SPECT (0.939 ± 1.266%) was greater than that on SPECT/CT (0.851 ± 1.223%) ($p = 0.0035$). However, the strong correlation of %thyroid uptake between CT-free SPECT and SPECT/CT was still observed, and in various salivary diseases, the %thyroid uptakes by both SPECTs were highly comparable with only mild deviation (Figure 1.10). One patient had concomitant Graves' disease with high %thyroid uptake (4.862% and 4.662% on CT-free SPECT and SPECT/CT, respectively) (Figure 1.9), and the other 28 patients were euthyroid (0.828 ± 1.055% and 0.726 ± 1.024% by CT-free SPECT and SPECT/CT, respectively) ($p = 0.0002$). CT-free SPECT and SPECT/CT were similar in differentiating between hyperthyroidism and euthyroidism, considering the reported normal range of %thyroid uptake (0.78 ± 0.5%) (*13*).

Table 1.7. The external verification of CT-free SPECT versus SPECT/CT (n = 29 salivary gland SPECT/CT).

Metric	μ-map generation			Thyroid segmentation			Total SPECT counts			Thyroid-specific SPECT counts		
	R^2	MSE[c] ($\times 10^{-4}$)	%NMAE[d]	DSC[e]	VD[f] (mL)	95% HD[g] (mm)	R^2	MSE ($\times 10^{-4}$)	%NMAE	R^2	MSE ($\times 10^{-4}$)	%NMAE ($\times 10^{-4}$)
Mean	0.9419	1.8750	1.8345	0.6571	7.4804	13.5142	0.9835	0.0667	0.0436	0.9919	0.0107	0.7785
STD[a]	0.0197	0.6207	0.6138	0.0884	7.3833	7.2129	0.0096	0.0348	0.0249	0.0203	0.0296	0.6148
SER[b]	0.0036	0.1133	0.1121	0.0161	1.3480	1.3169	0.0017	0.0064	0.0045	0.0037	0.0054	0.1123

a: standard deviation

b: standard error

c: mean square error

d: normalized mean absolute error

e: Dice similarity coefficient

f: volume difference

g: Hausdorff distance

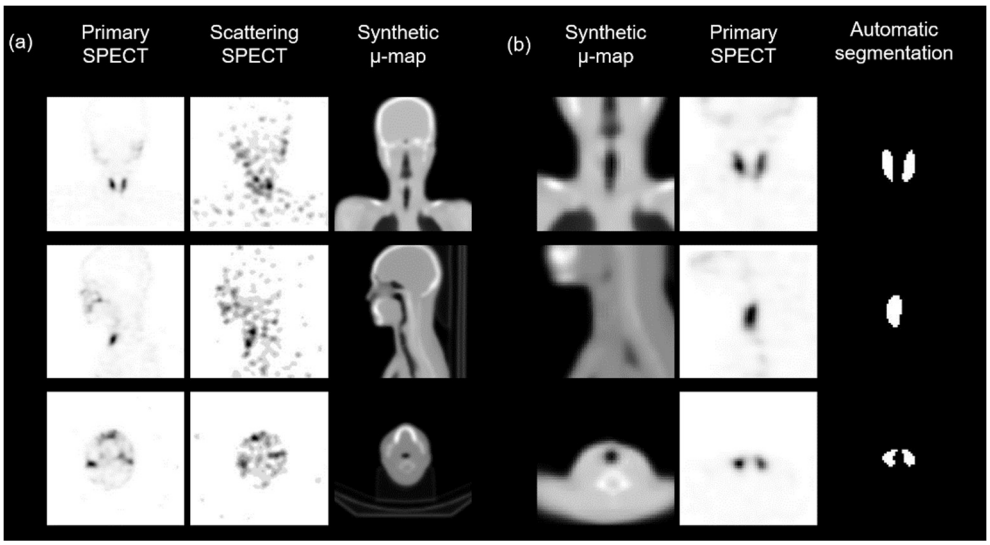

Figure 1.8. CT-free salivary SPECT in a euthyroid patient with left hypo-pharyngeal cancer (F/48). (a) Primary emission SPECT and scattering SPECT produced the synthetic μ map. (b) After cropping, the synthetic μ-map and the primary emission SPECT generated the thyroid segmentation map. The %thyroid uptake by deep-learning was normal at 0.886%, similar to 0.718% by conventional SPECT/CT. The normal reference range was 0.78 ± 0.5%.

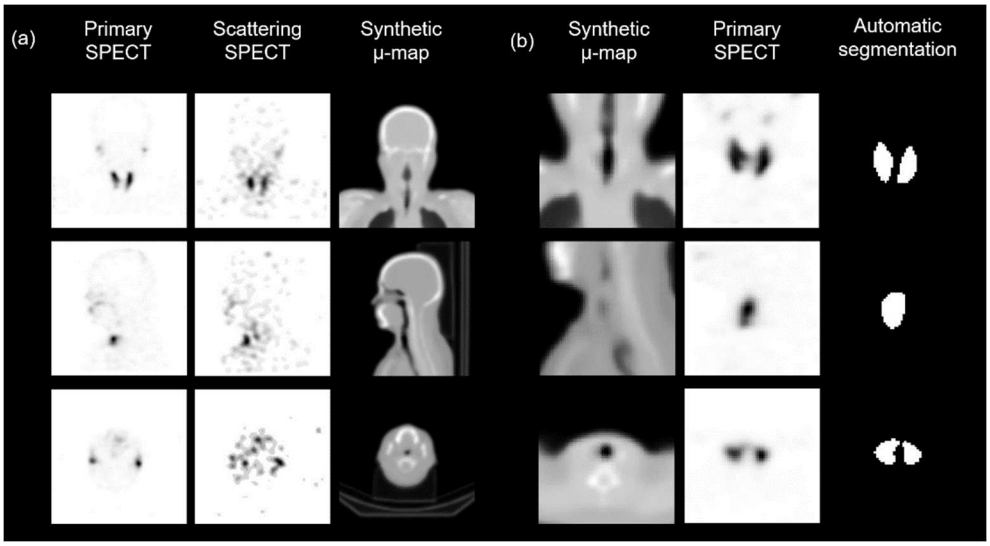

Figure 1.9. CT-free salivary SPECT in a patient with dry mouth and concomitant Graves' disease (F/56). (a) Primary emission SPECT and scattering SPECT generated the synthetic μ-map. (b) The synthetic μ-map and the primary emission SPECT produced the thyroid segmentation map after cropping. The %thyroid uptake by deep-learning was elevated as 4.862%, which corresponds to that by conventional SPECT/CT (4.662%). The normal reference range was 0.78 ± 0.5%.

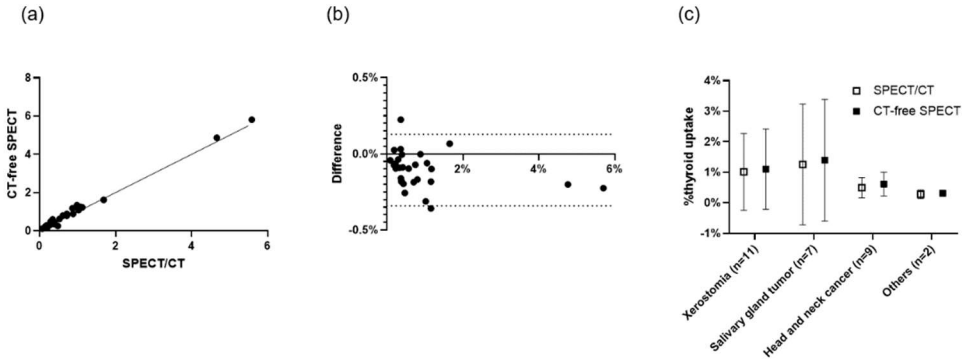

Figure 1.10. %thyroid uptake between CT-free SPECT and SPECT/CT as an external verification test (n = 29 salivary SPECT/CT). (a) The correlation is excellent with r = 0.9959, R2 = 0.9918, and p < 0.0001. (b) The Bland–Altman plot shows mild deviation (greater %thyroid uptake by CT-free SPECT) with bias = 0.106% point. (c) %thyroid uptakes between CT-free SPECT and SPECT/CT were similar in various salivary diseases. The normal reference range of %thyroid uptake was reported as 0.78 ± 0.5% (*13*).

DISCUSSION

Radioactive iodine uptake (RAIU) has been used for decades in conventional nuclear medicine practice to quantitatively evaluate thyroid function (*19*). Technetium thyroid uptake (TcTU) has been widely investigated as a surrogate for RAIU because it is facile, fast, and inexpensive with lower radiation exposure to patients than the RAIU (*20-23*). In contemporary nuclear medical practice, quantitative thyroid SPECT/CT, which employs AC, SC, and RR, has emerged as the most sophisticated method for measuring %thyroid uptake (*13*). Therefore, the %thyroid uptake and the standardized uptake value (SUV) could be examined for functioning thyroid diseases in the quantitative SPECT/CT era (*14-16*).

However, CT acquisition remains a significant barrier to the widespread clinical application of quantitative thyroid SPECT/CT because of CT-induced radiation exposure. In addition, the time-consuming manual thyroid segmentation on CT canvas is challenging for humans. Undoubtedly, AC using CT is essential for quantitative SPECT/CT. Therefore, this study attempted to address the CT-related issues associated with quantitative SPECT/CT.

We discovered that the deep learning-derived μ-maps are almost identical to those derived from CT. Notably, deep learning enabled the ps SPECTs to generate μ-map, as reported in a myocardial perfusion SPECT/CT study (*24*). The previous myocardial perfusion SPECT/CT study demonstrated the accuracy of deep-learning-based AC qualitatively (visual assessment), while we verified the accuracy quantitatively (%thyroid uptake). A similar concept was initially examined using positron emission tomography/computed tomography (PET/CT). Generating μ-map using deep-learning has been reported in fluorodeoxyglucose (FDG) brain PET/CT (*25*), fluoropropyl carbomethoxy iodophenyl tropane (FP-CIT) brain PET/CT (*26*), and FDG whole-body PET/CT (*27,28*), resulting in CT-free PET. Notably, only primary emission coincidence data were used to generate μ-map rather than scattering coincidence data in those PET studies (*25-28*). In PET, the scattering coincidence data cannot be properly estimated without μ-map. Therefore, using scattering information to predict the μ-map is challenging in principle. However, scattering information is relatively easy to obtain in SPECT by simply setting up an additional energy window. Therefore, if scattering information is essential for generating μ-map, CT-free SPECT by deep-learning would have technical advantages over CT-free PET. This would require further investigation.

Deep learning-based organ segmentation on CT has been actively investigated for single (*8,12*) or multiple organs (*29,30*). Thyroid segmentation has been a major concern by radio-oncologists seeking to save the thyroid from external radiation

therapy for head and neck cancer. CT with or without iodine contrast was generally used as the input for network training (*31-33*). It is of note that this study employed synthesized μ-map rather than CT as the input for thyroid segmentation. Low-resolution images, such as μ-map, can be used as input for deep learning-based automatic organ segmentation. The μ-map alone was clearly insufficient, and SPECT support was required to improve the segmentation results (Table 3), providing insight into the deep learning-based organ segmentation mechanism. We believe that the μ-map provides a silhouette of the head and neck for the approximate location of the thyroid, while the SPECT signal confirms its presence. Although Tc-99m pertechnetate uptake was low and faint in patients with thyroiditis, that was sufficient evidence of thyroid existence (Figs 3 and 4).

High-resolution images, such as synthetic CT (or pseudo-CT), can be generated as an intermediate canvas for thyroid segmentation rather than μ-map (*34,35*). Then, another μ-map generation process would have been necessary for the AC. In contrast, fully attenuation-corrected SPECT can be obtained without intermediate μ-map generation, such as direct conversion from non-attenuation-corrected PET to attenuation-corrected PET (*36*). In this case, another method for automatic thyroid segmentation is required. In this regard, we expect that using a μ-map as a bridge between two deep-learning networks (one for AC and the other for automatic organ segmentation) would minimize the overall effort required to evaluate %thyroid uptake.

In this study, we applied data augmentation, specifically flip augmentation, and implemented early stopping during training to minimize the risk of overfitting. These techniques helped ensure that the model generalized well to unseen data, despite the limited dataset available.

Limitation

This study was conducted using a limited dataset from a single institution (n=298 and 316 for μ-map generation and automatic segmentation, respectively), with both the validation and test sets also being limited. As a result, the developed algorithms may have been subject to overfitting. Addtionally, in external verification, thyroid volume may have been overestimated in patients with salivary gland disease, who were assumed to have normal thyroid function. This overestimation of thyroid volume likely led to an overestimation of %thyroid uptake.

Conclusion

Sequential application of two deep-learning algorithms (the former for synthetic μ-map generation from SPECT images and the latter for automatic thyroid segmentation from the generated μ-map with primary emission SPECT support) can realize CT-free quantitative SPECT for %thyroid uptake.

Chapter 3. Deep-learning-based attenuation map generation in kidney single photon emission computed tomography

Background

Quantitative methods used in nuclear medicine rely heavily on accurate attenuation corrections (AC). The AC assesses the attenuation coefficients of the matter of interest. Initially, these coefficients were mathematically determined for homogeneous organs, such as the brain (*37*). Later, transmission scans using external radionuclides generated attenuation maps (μ-maps) for non-homogeneous organs (*38*). X-ray computed tomography (CT) has become the preferred method for AC across organs because of its superior image quality, reduced imaging time, and precise tissue delineation compared to radionuclide transmission scans (*39*).

Quantitative single-photon emission computed tomography/computed tomography (SPECT/CT) is an emerging modality in nuclear medicine, where CT plays a crucial role in AC (*11*). The μ-map, based on CT Hounsfield units, integrates into the reconstruction of quantitative SPECT images. The results are clinically invaluable quantitative parameters, such as the percent injected dose (%ID) and standardized uptake value (SUV) of target organs (*3,13,14*).

Recent advancements in artificial intelligence (AI) have profoundly affected SPECT/CT imaging. Networks like convolutional neural network (CNN) or generative adversarial network (GAN) can create a synthetic μ-map without requiring a CT scan (*24,40*). These AI-driven innovations have been particularly effective in myocardial perfusion SPECT (*41*) and quantitative thyroid SPECT (*42*) imaging, leading to reduced radiation exposure in patients.

Technetium-99m diethylenetriaminepentaacetic acid (Tc99m-DTPA) renal scintigraphy is used to diagnose renal disorders because the renal uptake mechanism of Tc99m-DTPA is dependent on the glomerular filtration rate (GFR), a crucial biological measure of renal function (*43*). A correlation between the GFR and %ID of Tc99m-DTPA has been established in multiple studies (*44-46*). Although %ID measurement traditionally relied on 2-dimensional planar scintigraphy, 3-dimensional quantitative SPECT/CT imaging offers greater accuracy and consistency for renal %ID measurements and thus for GFR assessment (*9*).

Since 2017, our institution has been using Tc99m-DTPA SPECT/CT for GFR assessment (*9*). We developed an automatic kidney segmentation technique using CNNs (*8*). Our most recent development allows CNNs to generate a synthetic μ-map from SPECT data alone, eliminating the need for CT input, a method that has

been successfully applied to CT-free thyroid SPECT imaging (*42*).

In this study, our primary objective was to establish a CT-free quantification methodology in kidney SPECT. By exclusively using SPECT data, we aimed to train the CNNs to create μ-maps. The ultimate goal was to transition from conventional glomerular filtration rate (GFR) SPECT/CT to CT-free GFR SPECT.

Materials and method

Dataset

Tc99m-DTPA SPECT/CT data from January 2022 to January 2023 were used in this study (Table 2.1), which retrospectively comprised 1,000 SPECT/CT scans (male:female=662:338, age 55.740±12.967 years). Of these, 53.5% (535/1,000) were performed immediately after iodine contrast-enhanced CT in the Radiology Department. This was primarily because the patients underwent oncologic evaluations with a primary focus on renal tumours. Consequently, varying amounts of iodine contrast remain in the urinary system during SPECT/CT imaging in the nuclear medicine department. These 1,000 SPECT/CT images were allocated in an 8:1:1 ratio for training, validation, and testing. The proportions of contrast-enhanced CT scans were 54.0% (432/800), 53.0% (53/100), and 50.0% (50/100) for training, validation, and testing, respectively (Table 2.1).

Table 2.1. Characteristics of the datasets

		Training (n=800)	Validation (n=100)	Testing (n=100)	P value
Gender (male:female)		531:269	66:34	66:34	0.9950
Age (years)		56.3±12.9	54.5±13.2	53.4±13.3	0.0565
Height (cm)		166.1±8.9	167.4±9.2	168.6±8.7	0.0303
Weight (kg)		69.2±12.9	70.7±12.7	73.3±13.9	0.0217
BSA* (m^2)		1.8±0.2	1.8±0.2	1.8±0.2	0.0138
Proportion of contrast-enhanced CT		54.0% (=432/800)	53.0% (=53/100)	50.0% (=50/100)	0.7171
Reason for SPECT/CT	Normal (kidney donor)	37	2	1	0.0239
	Renal tumour	73	12	19	
	Urinary stone	126	20	9	
	Post partial nephrectomy	534	65	70	
	Post total nephrectomy	17	0	0	
	Hydronephrosis	8	0	0	
	Other	5	1	1	

* Body surface area by the Dubois formula:

BSA (m2) = $0.007184 \times (\text{weight in kg})^{0.425} \times (\text{height in cm})^{0.725}$

Data are mean ± standard deviation.

Acquisition and reconstruction of kidney SPECT/CT

No dietary restrictions were imposed during the acquisition of the Tc99m-DTPA kidney SPECT/CT imaging. Half an hour before the SPECT/CT imaging, 500 mL of water was provided to the patients for hydration. Patients were positioned on the table of one of two dual-head SPECT/CT scanners (NMCT670 or NMCT670pro; GE Healthcare, Chicago, IL, USA) equipped with low-energy high-resolution collimators. Tc99m-DTPA (TechneScan^R DTPA; Mallinckrodt Pharmaceuticals, Dublin, Ireland) was intravenously injected via the antecubital vein at an activity of 370 MBq.

SPECT images were acquired–2-3 minutes post-injection of Tc99m-DTPA under the following conditions: primary emission energy at 140 keV (20% window: 126-154 KeV), scatter energy at 120 keV (10% window: 115-125 KeV), 1-minute continuous acquisition mode with counter-clockwise rotation, no body contour option, and acquisition zoom factor of 1.28. Immediately after the SPECT scan, a

helical CT scan was performed using the following parameters: tube voltage of 120 KVp, tube current of 60-210 mA with autoMa function at a noise level of 20, detector collimation of 20 mm (= 16×1.25 mm), helical thickness of 2.5 mm, table speed of 37 mm/sec, table feed per rotation of 18.75 mm/rot, tube rotation time of 0.5 sec, and pitch of 0.938:1.

SPECT reconstruction was performed using iterative ordered-subset expectation–maximization (OSEM) (4 iterations and 10 subsets; Q.Metrix or Q.VolumetrixMI, GE Healthcare). Attenuation correction (AC), scatter correction (SC), and resolution recovery (RR) were applied to the reconstruction of the quantitative SPECT (ACSCRR SPECT). Post-reconstruction Butterworth filter was used with cutoff frequency of 0.48 cycles/cm and order of 10. SPECT image matrix was 128x128x128 and voxel size was 3.45×3.45×3.45 mm^3. CT images were reconstructed into a 512×512×161 matrix and 0.977×0.977×2.5 mm^3 voxel size.

Pre-processing for deep-learning

The AI algorithm was trained using SPECT scans (both primary emission and scattering) as inputs, with the CT-derived μ-map serving as the label. The primary emission and scattering SPECT images were reconstructed from the respective sinograms using vendor-provided software (Q. VolumetrixMI, GE Healthcare) with correction for the collimator-detector response (i.e., resolution recovery, RR), resulting in NCRR SPECT. Here, NC indicates neither attenuation correction (AC) nor scatter correction (SC). The ordered subset expectation-maximization (OSEM) algorithm was used for SPECT reconstruction with 10 subsets and four iterations. For statistical noise reduction, a Butterworth low-pass filter (order of 10 and cutoff frequency of 0.48 cycles/cm) was applied to the scattering SPECT images. The ground truth μ-map was derived from the CT component of SPECT/CT using the software (Q.VolumetrixMI, GE Healthcare). The original matrix and voxel sizes for both SPECT images and the μ-map were 128×128×128 and 3.45×3.45×3.45 mm^3, respectively. All images were cropped to 64×128×128 to shorten the z-axis span, which was intended to ensure consistency in the training volumes along the long body axis (z-axis).

The equations for normalization

The equation for the maximum normalization is:

$$V_{norm} = \frac{V_{origin} - V_{min}}{V_{max} - V_{min}}$$

The equation for the logarithmic maximum normalization is:

$$V_{norm} = \frac{log_{10}(1 + V_{origin} - V_{min})}{log_{10}(1 + V_{max} - V_{min})}$$

where V_{norm}, V_{origin}, V_{max} and V_{min} represent the voxel values for the normalized, original, maximum, and minimum values, respectively.

Network architecture

A modified 3D U-net with 64 initial neurons and 4 skip connections was employed (Figure 2.1) (*42*). The modified architecture replaces batch normalization layer to instance normalization, and transpose convolution layer to nearest-neighbor interpolation.

The network architecture comprised contraction and expansion paths with skip connections between the two paths. During the contraction path, convolution blocks consisting of a 3×3×3 kernel, instance normalization, and rectified linear unit (ReLU) activation were consecutively used twice. Subsequently, 2×2×2 max pooling was used for down-sampling. The convolution and max-pooling layers were consecutively applied 4 times, followed by an expansion path.

In the expansion path for up-sampling, nearest-neighbor interpolation and 2 times of the same convolution blocks (3×3×3 kernel, instance normalization, and ReLU activation) were consecutively applied four times. Finally, a 1×1×1 kernel convolution layer was applied without an activation function.

We trained our networks using TensorFlow (*17*) and the Keras framework (*18*).

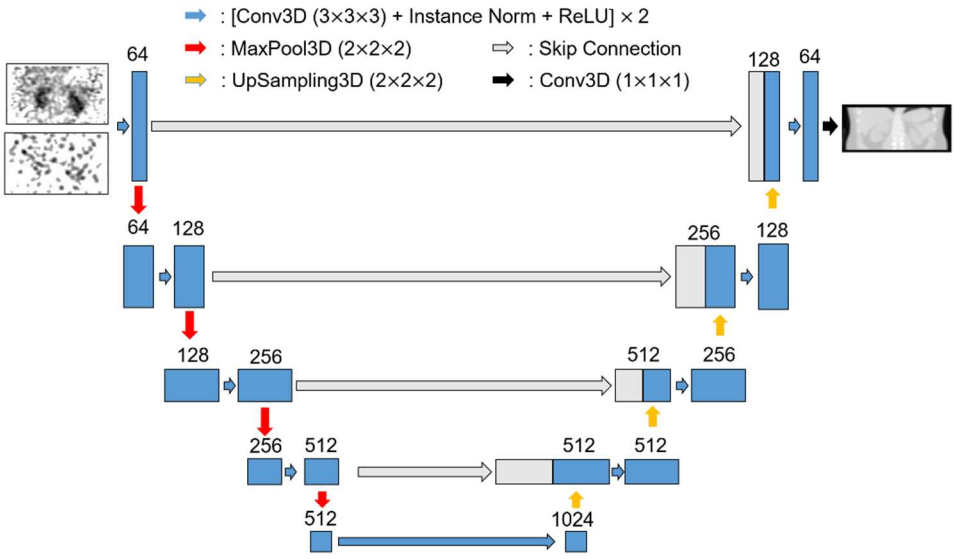

Figure 2.1. Network architecture for μ-map generation.

Loss function

The loss function for μ-map generator was defined as the combination of absolute difference loss (L_1) and gradient difference loss (L_{GDL}) with weighting factor ω.

$$L(G(X), Y) = L_1(G(X), Y) + \omega \times L_{GDL}(G(X), Y)$$

where G(X) represents generated synthetic μ-map from SPECT input X, and Y indicates ground truth of CT-derived μ-map. In this study, we did not consider the squared difference loss (that is,. L_2) because the superiority of L_1 over L_2 had been consistently reported in variable CT-related deep-learning studies such as those relating to the de-noising of low dose CT (*47*), reconstruction of micro CT (*48*), and μ-map generation from either positron emission tomography (PET) (*49*) or SPECT imaging (*42*).

The L_1 loss function was defined as:

$$L_1 = \frac{1}{N}\sum |G(X) - Y|$$

where N was the total number of voxels in the μ-map as a fixed value of 1,048,576 (= 64×128×128).

The gradient difference loss (L_{GDL}) was defined as:

$$L_{GDL}{}^n = \frac{1}{M}\sum \big||\nabla G(X)| - |\nabla Y|\big|^n$$

where M was the product of total number of voxels and the number of axes for gradients in the μ-map (3,145,728= 64×128×128×3), and ∇ was the image gradient operator. Here, n was either 1 for the absolute GDL ($L_{GDL}{}^1$) or 2 for the squared GDL ($L_{GDL}{}^2$).

The contested values of ω, the weighting factor of L_{GDL}, were 1, 3, and 5.

Training hyper-parameters

The number of training epochs was set to 100 with a batch size of eight. Early stopping rules were applied during the first 10 epochs. An adaptive moment estimation optimizer was used with a learning rate of 0.001 and an exponential decay rate of 0.96. Flip augmentation was applied along the x, y, and z axes. The training time was approximately 30 minutes per epoch. The computer hardware used for the network training was an AMD Ryzen7 5800X CPU (AMD Inc., Santa Clara, CA, USA) and an Nvidia RTX 3090 GPU (Nvidia Corp., Santa Clara, CA, USA).

Metrics for outcome evaluations

To evaluate the performance of the AI algorithm for synthetic μ-map generation, R

squared (R^2), mean squared error (MSE), and percent normalized mean absolute error (%NMAE) were used for pixel-wise comparisons of attenuation coefficients. R^2, mean squared error (MSE), and %normalized mean absolute error (%NMAE) were defined as:

$$R^2 = 1 - \frac{\sum((G(X) - Y)^2}{\sum(Y - \bar{Y})^2}$$

$$MSE = \frac{1}{N}\sum(G(X) - Y)^2$$

$$\%NMAE = \frac{1}{N} \cdot \frac{\sum|G(X) - Y|}{max(Y) - min(Y)} \times 100\%$$

where N represents the total number of voxels as 1,048,576 (=64×128×128), Y the target (i.e., original μ-map), $\bar{Y}$ the mean of Y, and G(X) the synthetic μ-map from SPECT input X.

GFR was calculated from the parenchymal radioactivity (that is,. %uptake) using the established equation: GFR (mL/min) = %uptake × 9.1462 + 23.0653 (*9*).

The definition of skewness

The skewness (S) was calculated using the following equation:

$$S = \frac{1}{N}\sum\frac{(V - V_{mean})^3}{std^3}$$

where N is degree of freedom in a given image (= 64×128×128-1), V voxel value, V_{mean} mean voxel value, and std standard deviation of V.

Statistical analysis

Parametric tests (i.e., *t*-test or analysis of variance) were performed for continuous variables when the Shapiro-Wilk test did not reject normal distribution features. Otherwise, non-parametric tests (i.e., Mann-Whitney U test or Kruskal-Wallis test) were performed. Categorical variables were compared using the chi-squared test. The Friedman test was conducted to evaluate performance under optimal AI conditions. Statistical significance was set at $p<0.05$. All analyses were performed using statistical software (MedCalc, version 22.013; Ostend, Belgium).

Results

We investigated the optimal AI working conditions in generating μ-maps, starting from the following baseline conditions: using only primary emission SPECT as input, applying maximum normalization to the SPECT input, employing the L_1 loss function, and utilizing transpose convolution in the expanding pathway of the CNN.

Input SPECTs

We first tested whether adding scattering SPECT to the primary emission SPECT would improve AI performance in μ-map generation. This is important because SPECT imaging has the advantage of easily obtaining scattering information, which is, in principle, difficult or impossible with PET imaging. The R^2 value increased whereas the MSE and %NMAE values decreased, indicating an improvement in AI performance (P alone vs. PS, Table 2.2). These findings were actually consistent with previous results, which advocated for the combined use of SPECT inputs (primary emission and scattering SPECT scans) for the μ-map generation (*24,42*).

Normalization of the input SPECT images

Next, we investigated the normalization of the input SPECT images. This step was crucial because SPECT data often exhibit characteristics of localized SPECT signals in the renal parenchyma against very low background signals, leading to a highly asymmetric data distribution (Figure 2.2). In this context, conventional maximum normalization could result in the under-representation of low signal areas in synthetic μ-map generation. Thus, we adopted a logarithmic maximum normalization method to mitigate the data scarcity or imbalance arising from the unique features of SPECT data. The application of logarithmic maximum normalization resulted in an overall greater signal strength and lower variance in the data distribution compared with conventional maximum normalization (Figure 2.2). This approach was successful across all outcome measures of R^2, MSE, and %NMAE (maximum vs. log-maximum, Table 2.2).

Table 2.2. Performance of AI algorithms for synthetic μ-map generation (n=100 testing cases)

Input	Normalization	Loss function	Up-sampling	R^2	MSE ($\times 10^{-4}$)	%NMAE
P alone	Max	L_1	TC	0.9802±0.0103	1.1081±0.5767	1.7975±0.4452
PS	Max	L_1	TC	0.9814±0.0094	1.0417±0.5367	1.7762±0.4253
PS	Log-max	L_1	TC	0.9818±0.0098	1.0216±0.5825	1.7049±0.4588
PS	Log-max	$L_1+3\times L_{GDL}$[1]	TC	0.9822±0.0096	0.9998±0.5673	1.6790±0.4315
PS	Log-max	$L_1+3\times L_{GDL}$[1]	Interpolation	0.9824±0.0098	0.9880±0.5601	1.6690±0.4315
				p<0.00001	p<0.00001	p<0.00001

P: primary emission SPECT
S: scattering SPECT
TC: transpose convolution
Max: maximum normalization
Log-max: logarithmic maximum normalization
Date are mean±standard deviation.

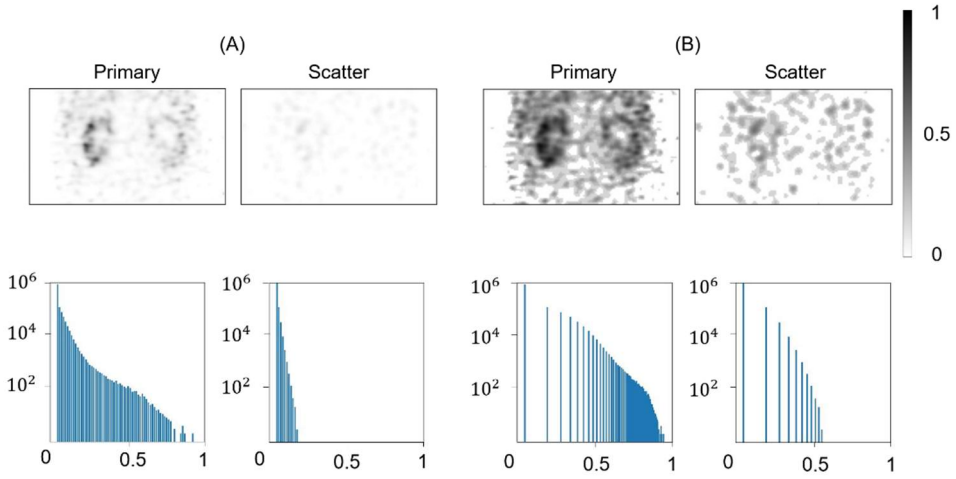

Figure 2.2. Effects of logarithmic maximum normalization on input single-photon emission computed tomography (SPECT) scans. (A) Maximum normalization of primary emission and scattering SPECT scans resulted in a highly asymmetric data distribution, exhibiting skewness values of 7.5080 and 4.8190 for primary emission and scattering SPECT scans, respectively. This approach also led to relatively weaker signal strength, with normalized median voxel value of 0.0282 and 0.0141 for primary emission and scattering SPECT scans, respectively. (B) In contrast, logarithmic maximum normalization reduced the data imbalance, indicated by skewness values of 2.0587 and 3.1611 for primary emission and scattering SPECT scans, respectively. It also enhanced the signal strength, with normalized median voxel value of 0.2569 and 0.1621 for primary emission and scattering SPECT scans, respectively.

Loss function optimization

Regarding the loss function, we tested the absolute GDL (L_{GDL}^1) versus the squared GDL (L_{GDL}^2) using three weighting factors (that is,. 1, 3, and 5) in addition to the L_1 loss function. L_{GDL}^1 with a weighting factor of three showed the best performance (Table 2.3 and Figure 2.3). The change in the loss function from L_1 alone to $L_1+3\times L_{GDL}^1$ increased R^2 and decreased the MSE and %NMAE (L_1 vs. $L_1+3\times L_{GDL}^1$, Table 2.2).

In a recent investigation, the L_{GDL} was tested without taking the absolute values of the operator (*49*); thus, we investigated different L_{GDL} with variable weighting factors but failed to show any benefit over the L_{GDL} using the absolute operator value (Table 2.4).

The gradient difference loss (L_{GDL}) was calculated using the operator without taking

absolute values, as follows:

$$L_{GDL}{}^{n} = \frac{1}{M}\sum|\nabla G(X) - \nabla Y|^{n}$$

where M was the product of total number of voxels and the number of axes for gradients in the μ-map (3,145,728= 64×128×128×3), and ▽ was the image gradient operator. Here, n was either 1 for the absolute GDL ($L_{GDL}{}^{1}$) or 2 for the squared GDL ($L_{GDL}{}^{2}$). The weighting factors investigated in these tests were 0.3, 1, and 3.

Table 2.3. Tests of gradient difference losses with variable weighting factors in addition to the L_1 loss function (n=100)

Input	Normalization	Loss function	Up-sampling	R^2	MSE ($\times 10^{-4}$)	%NMAE
PS	Log-max	$L_1+1\times L_{GDL}{}^1$	TC	0.9817±0.0101	1.0252±0.5955	1.7019±0.4593
PS	Log-max	$L_1+1\times L_{GDL}{}^2$	TC	0.9812±0.0097	1.0523±0.5579	1.7409±0.4251
PS	Log-max	$L_1+3\times L_{GDL}{}^1$	TC	0.9822±0.0096	0.9998±0.5673	1.6790±0.4315
PS	Log-max	$L_1+3\times L_{GDL}{}^2$	TC	0.9810±0.0101	1.0676±0.5873	1.7369±0.4468
PS	Log-max	$L_1+5\times L_{GDL}{}^1$	TC	0.9819±0.0098	1.0153±0.5693	1.7131±0.4283
PS	Log-max	$L_1+5\times L_{GDL}{}^2$	TC	0.9817±0.0093	1.0271±0.5490	1.6995±0.4305

Table 2.4. Other tests of gradient difference losses without taking the absolute operator values (n=100)

Input	Normalization	Loss function	Up-sampling	R^2	MSE ($\times 10^{-4}$)	%NMAE
PS	Log-max	$L_1+0.3\times L_{GDL}^1$	TC	0.9819±0.0095	1.0151±0.5661	1.7029±0.4439
PS	Log-max	$L_1+0.3\times L_{GDL}^2$	TC	0.9815±0.0097	1.0351±0.5665	1.7060±0.4280
PS	Log-max	$L_1+1\times L_{GDL}^1$	TC	0.9817±0.0105	1.0221±0.5970	1.7048±0.4384
PS	Log-max	$L_1+1\times L_{GDL}^2$	TC	0.9812±0.0097	1.0535±0.5646	1.7307±0.4396
PS	Log-max	$L_1+3\times L_{GDL}^1$	TC	0.9812±0.0095	1.0539±0.5595	1.7374±0.4381
PS	Log-max	$L_1+3\times L_{GDL}^2$	TC	0.9818±0.0092	1.0231±0.5376	1.6977±0.4272

PS: primary emission and scattering SPECT
Log-max: logarithmic maximum normalization
TC: transpose convolution

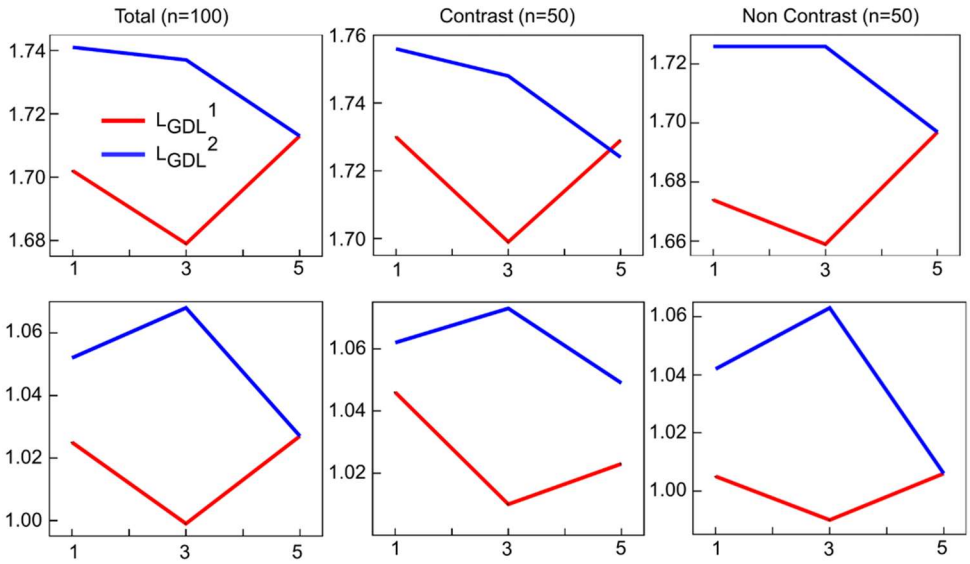

Figure 2.3. Tests for Weighting Factors of LGDL. Upper row indicates MSE (×10-4), while lower row %NMAE. Weighting factor 3 with absolute GDL loss (3×LGDL1) showed the lowest MSE and %NMAE.

Nearest-neighbor interpolation during up-sampling

The SPECT input sometimes exhibited high focal activity in the kidney, which often resulted in checkerboard artifacts in the synthetic μ-map (Figure 2.4A). Such artifacts have been reported to occur in or adjacent to high-signal areas during image generation using neural networks (*50*). In the case of kidney SPECT imaging, artifacts often appeared in both kidneys when primary emission SPECT was used alone as input (Figure 2.4A), and tended to lateralize to one of the two kidneys when scattering SPECT was additionally employed as input (Figure 2.4B). Application of log-max normalization slightly diminished the size of the artifacts (Figure 2.4C). Moreover, the addition of a $3\times L_{GDL}{}^{1}$ loss function systemically shifted the artifact location from the renal parenchyma to the central renal pelvis (Figure 2.4D). Finally, replacing the transpose convolution with nearest-neighbor interpolation completely eliminated checkerboard artifacts (Figure 2.4E), thereby improving the outcome parameters R^2, MSE, and %NMAE (TC vs. interpolation, Table 2.2). The error maps of attenuation coefficients (the ground truth minus the generated synthetic μ-maps) clearly demonstrated the sequential reduction of the checkerboard artifact (Figure 2.5). As a result, the AI-based corrected ASCSRR SPECT was indistinguishable fromthe ground truth CT-based corrected ASCSRR SPECT, with minimal differences (Figure 2.6).

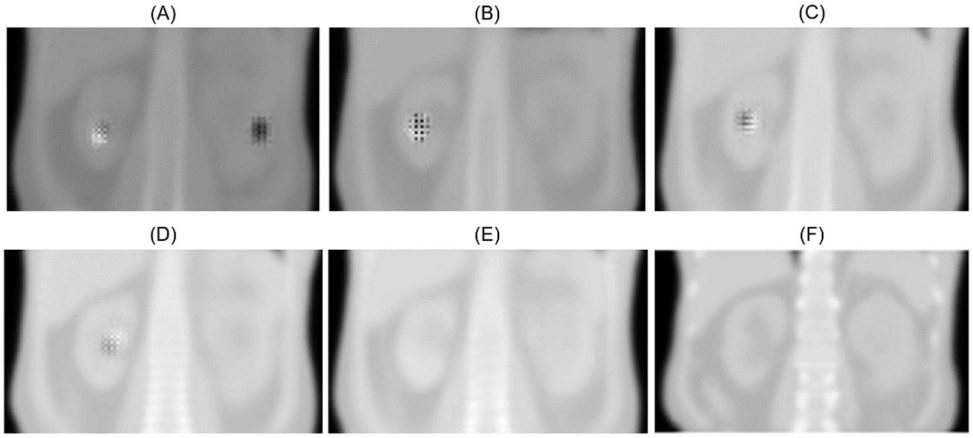

Figure 2.4. Resolution of checkerboard artefacts using optimal training conditions for μ-map generation. The sequence of applying training conditions follow the same order as presented in Table 2.2. (A) shows the result using only primary emission single-photon emission computed tomography (SPECT) as input. (B) depicts the outcome with the addition of scattering SPECT to primary emission SPECT (PS) imaging. (C) illustrates the effect of applying log-max normalization to the PS input. (D) presents the result using the additional $3\times L_{GDL}{}^{1}$ loss function to (C). (E) demonstrates the impact of applying nearest-neighbor interpolation to (D), replacing transpose convolution. (F) provides the ground truth of the CT-derived μ-map for comparison.

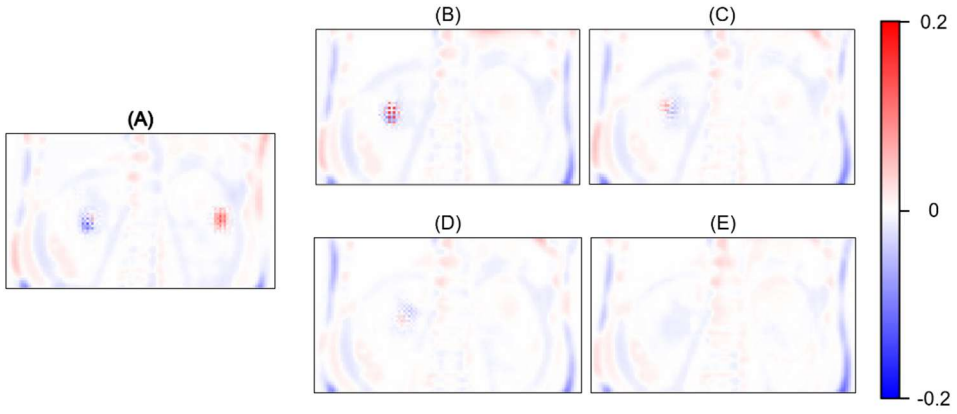

Figure 2.5. Error maps showing the resolution of checkerboard artifacts. Individual panels show the difference of attenuation coefficients between the ground truth (computed tomography-derived μ-map) vs. (A) primary emission single-photon emission computed tomography (SPECT) alone input, (B) primary emission and scattering SPECT (PS) input, (C) PS with log-max normalization, (D) PS with log-

max normalization using an additional $3\times L_{GDL}{}^{1}$ loss function, and (E) nearest-neighbor interpolation application to (D) instead of transpose convolution. The scale bar indicates the attenuation coefficients in unit of cm^{-1}.

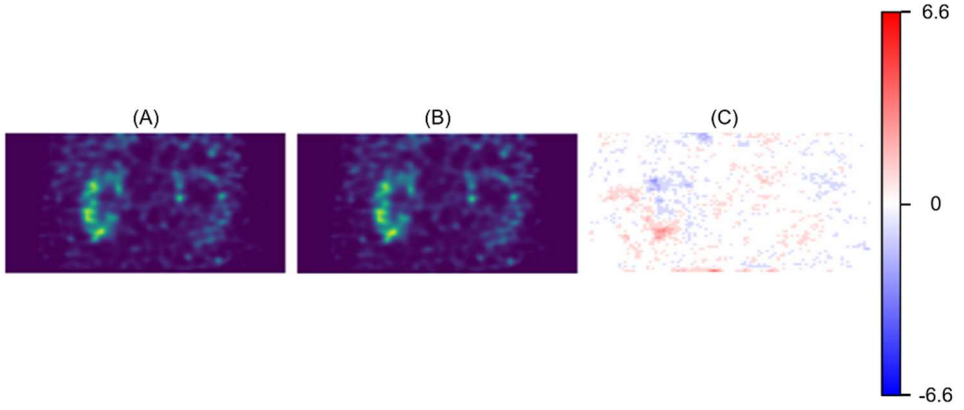

Figure 2.6. Comparison of ASCSRR (attenuation correction, scatter correction, and resolution recovery) SPECT images between the AI-based corrected SPECT (A) and the ground truth CT-based corrected SPECT (B). The differences were minimal in terms of SPECT counts/voxel (C).

The interpolation application was also tested in various ways, but modifications of the nearest-neighbor interpolation produced halo artifacts (Table 2.5 and Figure 2.7); thus, further modifications were abandoned.

Table 2.5. Tests of different interpolations for up-sampling (n=100)

Input	Normalization	Loss function	Up-sampling	R^2	MSE ($\times 10^{-4}$)	%NMAE
PS	Log-max	$L_1+3\times L_{GDL}{}^1$	Interpolation +convolution (2×2×2 kernel)	0.9827±0.0100	0.9695±0.5828	1.6858±0.4366
PS	Log-ma×	$L_1+3\times L_{GDL}{}^1$	Interpolation +convolution block*	0.9827±0.0101	0.9701±0.5806	1.6638±0.4353

*The convolution block consists of a 2×2×2 kernel, an instance normalization layer, and ReLU activation.

PS: primary emission and scattering SPECT

Log-max: logarithmic maximum normalization

Date are mean±standard deviation.

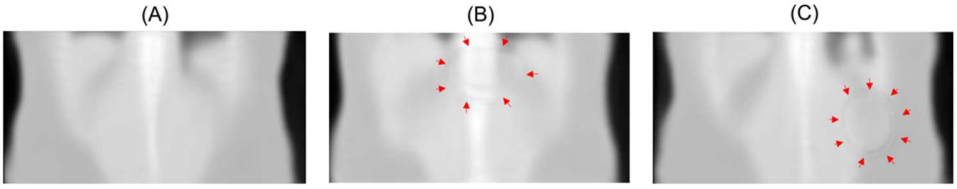

Figure 2.7. Artifacts caused by modification of nearest-neighbor interpolation. (A) nearest-neighbor interpolation only, (B) nearest-neighbor interpolation plus 2×2×2 kernel convolution, and (C) nearest-neighbor interpolation plus a convolution block (2×2×2 kernel, instance normalization, and ReLU activation). Please see the red arrows for the halo artifacts in (B) and (C).

The iodine contrast effects for μ-map generation

We divided the 100 SPECT/CT cases in the testing group into 50 cases with contrast effects from the previous iodine contrast-enhanced CT (Table 2.6) and 50 cases without these effects (Table 2.6). Overall, the same trends in AI performance improvement were observed in both subgroups using optimal training conditions for AI (that is,. PS [primary emission and scattering SPECT imaging]) input, logarithmic maximum normalization of the SPECT images, L_1 plus $3\times L_{GDL}{}^1$ combinatory loss function, and nearest-neighbor interpolation during up-sampling). One exception was found in the last step of the subgroup without the iodine contrast effect (Table 2.6). Here, the application of nearest-neighbor interpolation instead of transpose convolution slightly reduced R^2 and increased the MSE and %NMAE (Table 2.7). However, only when using the nearest-neighbor interpolation did the checkerboard artifacts completely disappear (Figures 2.4E for μ-map, and 2.5E for error map of attenuation coefficients).

Table 2.6. Performance of AI algorithms for synthetic μ-map generation in SPECT/CT cases with iodine contrast effect (n=50)

Input	Normalization	Loss function	Up-sampling	R^2	MSE ($\times 10^{-4}$)	%NMAE
P alone	Max	L_1	TC	0.9801±0.0091	1.1249±0.5004	1.8288±0.4046
PS	Max	L_1	TC	0.9818±0.0085	1.0316±0.4706	1.7831±0.3750
PS	Log-max	L_1	TC	0.9818±0.0088	1.0374±0.5042	1.7323±0.4078
PS	Log-max	$L_1+3\times L_{GDL}{}^1$	TC	0.9822±0.0080	1.0010±0.4581	1.6994±0.3645
PS	Log-max	$L_1+3\times L_{GDL}{}^1$	Interpolation	0.9827±0.0078	0.9821±0.4367	1.6780±0.3618

P: primary emission SPECT
S: scattering SPECT
TC: transpose convolution
Max: maximum normalization
Log-max: logarithmic maximum normalization
Date are mean±standard deviation.

Table 2.7. Performance of AI algorithms for synthetic μ-map generation in SPECT/CT cases without iodine contrast effect (n=50)

Input	Normalization	Loss function	Up-sampling	R2	MSE (×10-4)	%NMAE
P alone	Max	L1	TC	0.9802±0.0115	1.0912±0.6489	1.7663±0.4846
PS	Max	L1	TC	0.9809±0.0104	1.0517±0.6002	1.7693±0.4741
PS	Log-max	L1	TC	0.9819±0.0108	1.0058±0.6564	1.6776±0.5073
PS	Log-max	$L1+3\times L_{GDL}{}^{1}$	TC	0.9821±0.0110	0.9901±0.6634	1.6586±0.4924
PS	Log-max	$L1+3\times L_{GDL}{}^{1}$	Interpolation	0.9820±0.0114	0.9938±0.6656	1.6600±0.4952

P: primary emission SPECT

S: scattering SPECT

TC: transpose convolution

Max: maximum normalization

Log-max: logarithmic maximum normalization

Date are mean±standard deviation.

The AI algorithm was trained on approximately half the cases involving contrast-enhanced CT as labels (Table 2.1). In other words, the iodine contrast media was present in half of the cases of the ground truth μ-maps during the AI training. The existence of iodine contrast media was typically apparent in the renal pelvis (Figure 2.8A), but the trained AI algorithm consistently generated μ-maps without iodine contrast effects in the renal pelvis (Figure 2.8B). This was because the μ-maps were primarily created from SPECT radioactivity signals originating from the renal parenchyma. The renal pelvis is the site of urine accumulation without a functional renal parenchyma. As a result, the output of the AI algorithm was always a signal void in the renal pelvis, even in the presence of iodine contrast medium in the ground truth (Figure 2.8B). In contrast, the presence of iodine contrast media in the renal parenchyma was visually inconspicuous (Figure 2.8A) and led to a subtle increase in attenuation coefficients compared to the synthetic μ-map (Figure 2.8B), subsequently leading to over-correction of radioactivity in the renal parenchyma (arrow heads in Figure 2.8C). The levels of attenuation coefficients in the synthetic μ-maps fell within an intermediate range between those derived from contrast-enhanced and non-contrast-enhanced CT, which was indicated by the positive difference from the contrast-enhanced ground truth and the negative difference from the non-contrast-enhanced ground truth (Table 2.7). Therefore, the radioactivity associated with CT-free SPECT and the subsequent GFR values derived from the developed AI algorithm were significantly lower ($p<0.0001$) than those obtained by SPECT/CT with contrast effects (n=50), but significantly higher ($p<0.0001$) than those obtained by SPECT/CT imaging without contrast effects (n=50; Table 2.8). However, the effect of the presence of contrast media was insignificant because the maximum difference in GFR using the extreme limits for contrast CT (0.4530+1.0658 mL/min = 1.5188 mL/min) and non-contrast CT (-0.4394-0.9316 mL/min = -1.3710 mL/min) was only 2.8898 mL/min, which was only 2.78% of the mean GFR values in this study (Table 2.8). Furthermore, in a total of 100 SPECT/CT cases collectively, the sums of attenuation coefficients (1147.0796±216.4121 cm^{-1} vs. 1146.5204±215.2922 cm^{-1}), the quantitative radioactivity (6.9259±1.6659% vs. 6.9232±1.6600%), and the GFR values (104.4920±17.1096 mL/min vs. 104.4852±17.1736 mL/min) in the renal parenchyma were not significantly different between the ground truth SPECT/CT and the AI-driven CT-free SPECT ($p>0.05$). Therefore, all of the findings above can be attributed to the nearly equal contribution of contrast-enhanced and non-contrast-enhanced CT to the development of the AI algorithm for μ-map generation (Table 2.1).

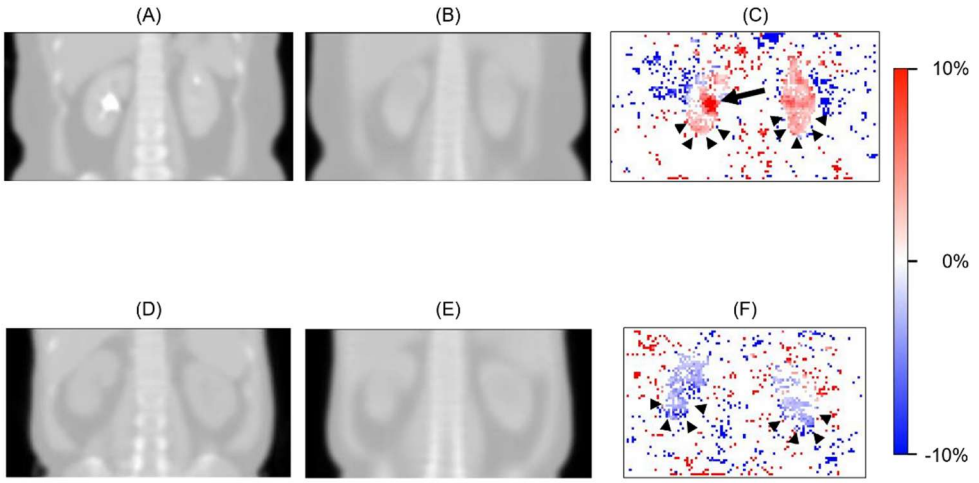

Figure 2.8. Characteristics of the artificial intelligence (AI) algorithm neutral to the iodine contrast media. (A) and (D) represent the ground truth μ-maps with and without iodine contrast media effects, respectively. (B) and (E) are the corresponding synthetic μ-maps generated by the AI algorithm. (C) and (F) show the corresponding error maps of radioactivity, comparing the ground truth single-photon emission computed tomography/CT (SPECT/CT) with CT-free SPECT imaging. Despite the presence of contrast-media in the renal pelvis of the CT-driven μ-map (A), the synthetic μ-map generated by the AI algorithm did not exhibit contrast effects (B). This can be appreciated in the intense red area of the right renal pelvis on the error map of radioactivity (long arrow) (C). The iodine contrast in the renal parenchyma, while subtle in the ground truth μ-map (A), showed slight increase of attenuation coefficients in the AI-driven synthetic μ-map (B), as evident in the error map (arrow heads) (C). In the case of the ground truth μ-map without iodine contrast (D), the AI-driven synthetic μ-map had slightly lower attenuation coefficients in the renal parenchyma (E), which was noticeable in the error map (arrow heads) (F).

Table 2.8. The difference between the SPECT/CT (the ground truth) and the AI-driven CT-free SPECT imaging according to the presence of iodine contrast media in the SPECT/CT imaging (n=100)

	Presence of contrast media (n=50)	No contrast media (n=50)	P value
Attenuation coefficients (cm^{-1})	19.8139±15.7953	-18.8138±5.9526	<0.0001
Radioactivity (%point)	0.0517±0.1167	-0.0464±0.1058	<0.0001
GFR (mL/min)	0.4530±1.0658	-0.4394±0.9316	<0.0001

Date are mean±standard deviation.

The reduction of radiation exposure to patients

Radiation exposure from SPECT/CT, which included both SPECT and CT components, ranged from 3.313 to 8.563 mSv in terms of effective dose. The SPECT component from the Tc99m-DTPA injection was 0.0049 mSv/MBq (*51*), resulting in an effective dose of 1.813 mSv for a 370 MBq injection. The effective dose from CT component varied within a range of 1.5–6.75 mSv, using a conversion factor of 15 μSv/mGy-cm (*52*). This variation was due to the variable dose-length product (100–450 mGy-cm), reflecting the differing extents of CT coverage of the abdomen and pelvis. Consequently, the potential reduction in radiation exposure by transitioning from conventional SPECT/CT to AI-based CT-free SPECT is 45.3%–78.8%

DISCUSSION

The issue of AC in nuclear medicine, specifically SPECT imaging, has been effectively addressed over the last few decades with the advent of hybrid scanners, such as SPECT/CT scanners (*38,39*). Despite the widespread adoption of these scanners, concerns regarding radiation exposure in patients have persisted in the field of nuclear medicine. Moreover, misalignment between CT and SPECT images, often resulting from patient motion, has been a significant topic of discussion regarding the accuracy of quantitative SPECT/CT (*53*). Consequently, alternatives to CT have been intensively explored.

Recent advancements in AI have shown promise for various medical imaging applications, including reducing radiation exposure to patients and enabling CT-less imaging. These studies required the acquisition of low-dose or ultra-low-dose CT,

allowing the enhancement of CT images with poor signal-to-noise ratios to the quality of usual dose CT through AI applications (*54,55*). Several other researchers have focused primarily on AI-driven AC techniques for SPECT. Those studies did not require CT acquisition, and the performance of the AI was validated using SPECT/CT as a reference, paving the way for CT-free (rather than CT-less) imaging studies (*24,56,57*).

In this study, we explored the potential use of AI as a substitute for CT in the AC of kidney SPECT. Our approach was inspired by other studies on myocardial perfusion SPECT/CT (*40,58*) or thyroid SPECT/CT imaging (*42*). In these studies, AI algorithms were trained using only SPECT images as inputs and CT-derived μ-maps as labels, thus generating synthetic μ-maps for AC of SPECT imaging. We optimized the AI working conditions (incorporating scattering SPECT with primary emission SPECT as input, applying log-maximum normalization instead of maximum normalization for SPECT input, using a combined loss function of L1 and $3\times L_{GDL}{}^{1}$ and preferring nearest-neighbor interpolation over transpose convolution in the CNN up-sampling process) and demonstrated the effectiveness of the developed AI algorithm for Tc99m-DTPA kidney SPECT.

Previous deep-learning-based studies on AC in nuclear medicine imaging have primarily focused on PET rather than SPECT (*26,27,59*). We believe that a completely different approach may be required for SPECT because scattering information is more readily obtainable for SPECT than for PET scans, and the standard OSEM reconstruction algorithm may be effective for single-bed SPECT applications such as kidney SPECT or thyroid SPECT (*42*). This contrasts with PET, which typically requires whole-body coverage and a more complicated reconstruction algorithm (*49,60*).

In this study, we applied data augmentation, specifically flip augmentation, and implemented early stopping during training to minimize the risk of overfitting. These techniques helped ensure that the model generalized well to unseen data, despite the limited dataset available.

LIMITATIONS

Despite the promising outcomes of our study, it is important to acknowledge its limitations. Firstly, our study was conducted within a single institution, which might introduce a selection bias and limit the external validity of the findings, and increase the potential for overfitting. Secondly, while our AI algorithm showed high accuracy in generating μ-maps neutral to contrast-media effects, it was trained and tested on datasets from specific CT and SPECT machines. The performance of the algorithm might vary when applied to data from different equipment or settings, necessitating additional tuning and validation. Thirdly, our study focused primarily on kidney

SPECT/CT imaging for GFR measurement; thus, the application of our findings to other organs or conditions requires further investigation. Finally, the impact of the AI algorithm on clinical outcomes was not directly assessed in this study. Future research should aim to not only replicate these findings in a multi-centre context but also explore the clinical implications of using AI-supported CT-free SPECT imaging in routine practice.

CONCLUSION

We clarified the importance of scattering information for μ-map generation in SPECT, found the effect of logarithmic maximum normalization on the input SPECTs, optimized the loss function and removed SPECT-specific checkerboard artifacts by an interpolation up-sampling. The AI algorithm was influenced equally by both contrast-enhanced and non-contrast-enhanced CT scans. As a result, it generated μ-maps with attenuation coefficients in an intermediate range, making the CT-free SPECT imaging neutral to the effects of contrast-media present in the ground truth SPECT/CT. Conventional kidney SPECT/CT imaging for GFR measurement could potentially be replaced by CT-free SPECT imaging using the developed AI algorithm.

Chapter 4. I-131 Quantitative SPECT/CT for Absorbed Dose Measurement of Blood and Tumour in Pre-Therapeutic Dosimetry for Thyroid Cancer with Multiple Bone Metastases

Background

Radioactive iodine (RAI) therapy using I-131 is a cornerstone in the management of thyroid cancer, particularly in patients with multiple metastases (*61,62*). The efficacy of this treatment, however, is tempered by the risk of bone marrow toxicity, necessitating precise dosimetric assessments to optimize therapeutic outcomes while minimizing adverse effects (*63,64*). Traditionally, blood-based dosimetry involving the gamma counting of blood samples has been the standard method for predicting bone marrow toxicity (*65,66*). However, when it comes to tumour dosimetry, no practical dosimetric assessment tools have been suggested. Therefore, without taking therapeutic efficacy into account, maximal tolerated activity has often been considered the most adequate strategy in thyroid cancer patients with multiple metastases (*67-69*).

Recent advancements in nuclear medicine imaging technologies, specifically quantitative single-photon emission computed tomography/computed tomography (SPECT/CT), offer a promising alternative to the conventional therapeutic approach (*3,11*). Quantitative SPECT/CT enables the non-invasive measurement of RAI activity over the blood pool and thyroid tumour in the SPECT/CT images (*70,71*).

In this study, we explored the feasibility of quantitative SPECT/CT for I-131 dosimetry. The reproducibility and accuracy of I-131 activity measurement were investigated by comparing the blood pool I-131 activity from SPECT/CT with that derived from gold standard blood sample gamma counting. The absorbed doses for blood and tumour were calculated by Monte-Carlo simulation using the quantitative SPECT/CT images and a simple equation is suggested to predict the tumour absorbed dose by the tumour I-131 concentration from the quantitative SPECT/CT. Our research aims to ensure the viability of I-131 quantitative SPECT/CT for pre-therapeutic planning of I-131 activity administration in thyroid cancer patients with multiple bone metastases.

Materials and methods

Patients

The study was conducted at a tertiary referral hospital located at South Korea

between March 2022 and November 2023 and involved pre-therapeutic dosimetry assessments using quantitative I-131 SPECT/CT and serial blood sampling in five thyroid cancer patients with multiple bone metastases (Table 3.1). All the patients had the primary thyroid cancer removed by total thyroidectomy prior to the I-131 SPECT/CT dosimetry and bone metastasis was confirmed by either tissue diagnosis (case nos. 1,3,4, and 5) or imaging studies such as MRI and F-18 FDG PET/CT (case no. 2). The tissue type of the primary mass was poorly-differentiated thyroid carcinoma (PDTC) in all 5 patients, but the metastatic bone tissues had follicular thyroid carcinoma (FTC) feature (n=3) or non-specified metastatic cancer with thyroglobulin (TG) expression (n=1). Before the I-131 SPECT/CT dosimetry, high activity I-131 therapy or external-beam radiation therapy were given to all but one patient (case no. 5). All the patients provided their informed consents and the institutional review board approved the study design.
The Institutional Review Board (IRB) approved the study design and the informed consent was acquired for all the participants. (Institution: Seoul National University Bundang Hospital, IRB No: B-2412-943-102).

I-131 whole-body planar scan acquisition conditions

The anterior/posterior whole-body scans were acquired using the following parameters: a peak energy of 364 keV with a ±10% window (327.6–400.5 keV), a scatter energy of 297 keV with a ±10% window (267.3–326.7 keV), a matrix size of 256x1024, and a zoom factor of 0.92.

Determination of the counting efficiency for the gamma counter

The counting efficiency of the gamma counter (Automatic Gamma Counter, HIDEX, Finland) for I-131 was determined by performing three separate tests. In these tests, an I-131 solution (approximately 0.5 mCi), measured using a dose calibrator (CRC-55tR, CAPINTEC, USA), was put into a 1 L volumetric flask that had been half-filled with tap water. The flask was then full-filled up to 1 L with tap water. With the flask opening plugged, we vigorously mixed the contents of the flask to ensure even distribution of I-131. Three 1 mL samples were taken, and gamma counting was performed for 30 min per each sample. The gamma counter efficiency was determined to be 43.98% from the average of the three tests

Table 3.1. Characteristics of thyroid cancer patients with multiple bone metastases

Case No.	Age	Sex	Tissue type of thyroid cancer	Tissue type of bone metastasis	No. of bone metastasis (sites)	Site of tissue confirmation	Prior external RT	Prior I-131 therapy (activity)
1	72	Male	PDTC	Metastatic cancer with TG expression	2 (T4, sacrum)	T4	Yes (T4, sacrum)	Yes (200mCi)
2	56	Male	PDTC	No tissue confirmation	2 (Lt. acetabulum, T2)	-	No	Yes (300mCi, 100mCi)
3	54	Female	PDTC	Metastatic FTC	6 (Lt. 9th rib, sternum, Rt. 8th rib, L3, Lt. ilium, Lt. femur)	Lt. ilium	Yes (Lt. ilium, Lt. femur)	Yes (150mCi)
4	84	Female	PDTC	Metastatic FTC	3 (C6, L3, Rt. 2nd rib)	L3	Yes (C6, L3)	No
5	65	Female	PDTC	Metastatic FTC	5 (sternum, T6, T10, L4, Lt. 8th rib)	Sternum	No	No

PDTC; poorly differentiated thyroid carcinoma, TG; thyroglobulin, FTC; follicular thyroid carcinoma, RT; radiation therapy

Table 3.2. Measurements for gamma counting efficiency (n=3)

	Test 1	Test 2	Test 3	
Injected activity (Mega Becquerel) per 1 L	14.282	16.650	20.720	
Injected activity (DPM) per 1 mL	858042	999395	1243411	
Measured counts (CPM) per 1 mL (mean)	373666	437322	554994	
Counting efficiency (%)	43.5487	43.7587	44.6348	43.9807

DPM; decay per minute, CPM; count per minute

I-131 SPECT/CT acquisition and reconstruction conditions

The acquisition and reconstruction conditions were the same for the 2 SPECT/CT scanners (NMCT670 and NMCT670pro, GE).

CT acquisition parameters were: 120 kVp voltage, 30 mA current, 20 mm (=16x1.25) collimation, 2.5 mm helical thickness, 37 mm/sec table speed, 18.75 mm/rot table feed per rotation, 0.5 sec tube rotation time, and 0.938:1 pitch. CT was reconstructed into 512x512 matrix, slice thicknesses of 2.5 mm trans-axial, 0.98 mm coronal, and 0.98 mm sagittal sections with no increment, using adaptive statistical iterative reconstruction algorithm (GE).

SPECT acquisition parameters were: primary energy of 364 keV (±10%; 327.6-400.5 keV), lower scatter energy of 318 keV (±3%; 308.5-327.5 keV), higher scatter energy of 413 keV (±3%; 400.6-425.4 keV), and step-and-shoot mode with 20 sec acquisition per step and 6-degree angular increment. Body contour option was activated without application of acquisition zoom. SPECT was reconstructed by ordered subset expectation maximization (OSEM) algorithm (4 iterations and 10 subsets) with CT attenuation correction, triple energy window scatter correction (weighting factor of 1.19), and resolution recovery into 128x128 matrix and 3.45 mm slice thickness (Q.Volumetrix AI, GE).

Determination of the system sensitivity for the SPECT/CT scanners

The following phantom study was independently conducted three times. A uniform cylinder phantom (diameter: 20 cm, length: 30 cm, and weight in empty state: 2.45 kg) was used. First, the phantom was approximately half-filled with tap water. Second, an I-131 solution (0.5 mCi) was injected into the phantom. Finally, additional water was added until the weight of the water-filled phantom reached a total maximum of 11.3 kg. The total volume of water used was 8.85 liters. The I-131 activity was measured using a dose calibrator (CRC-15tR, CAPINTEC, USA),

which is calibrated monthly with the NIST traceable standard source of Co-57. The phantom was placed at the field-of-view centre, and a 10-minute SPECT was acquired using the following parameters: 360-degree coverage using an auto-contouring step-and-shoot acquisition mode (60 projections over 360°, 180° per detector, step of 6°, 20 seconds for each projection), a peak energy of 364 keV with a ±10% window (327.6–400.5 keV), a lower scatter energy of 318 keV with a ±3% window (308.5–327.5 keV), a higher scatter energy of 413 keV with a ±3% window (400.6–425.4 keV), and a zoom factor of 1.28. A spiral CT was then performed with the following parameters: tube potential of 120 kVp, tube current of 30 mA, beam collimation of 20 mm (=1.25x16), pitch of 0.938:1, speed of 18.75 mm/rotation, and tube rotation time of 0.5 seconds. SPECT images were iteratively reconstructed using the OSEM algorithm with 4 iterations and 10 subsets. During SPECT reconstruction, triple corrections (CT-based attenuation correction, triple-energy window scatter correction with a weighting factor of 1.19, and correction of depth-dependent collimator-detector response) were applied using vendor-provided software (Q. Volumetrix AI, GE) on a dedicated workstation (Xeleris version 4DR, GE).

Table 3.3. Measurements of system sensitivity for NMCT670 (n=3)

	Test 1	Test 2	Test 3	
Injected activity (mCi)	0.561	0.408	0.429	
Measured counts (CPM) by ACSCRR SPECT (2 detectors)	65295.8	46731.1	49126.1	
System sensitivity (CPM/μCi)	58.1959	57.2685	57.2565	57.6765 CPM/μCi

Table 3.4. Measurements of system sensitivity for NMCT670pro (n=3)

	Test 1	Test 2	Test 3	
Injected activity (mCi)	0.564	0.434	0.430	
Measured counts (CPM) by ACSCRR SPECT (2 detectors)	66190.2	49519.8	49240.2	
System sensitivity (%)	58.6793	57.0505	57.2560	57.6619 CPM/μCi

CPM; count per minute
ACSCRR; attenuation correction, scatter correction, and resolution recovery applied
SPECT; single-photon emission computed tomography

I-131 SPECT/CT for dosimetry

For the I-131 SPECT/CT dosimetry, each patient received an oral administration of I-131 (approximately 3 mCi solution) (Unitech Sodium Iodide, Samyoung Unitech Co., Ltd, Korea) following a thyroid hormone withdrawal protocol (i.e., thyroid hormone changes from thyroxine to triiodothyronine for 2 weeks and then a low-iodine diet for 2 weeks). Patients were instructed to urinate before the administration of the I-131 solution. The I-131 radioactivity and the measurement time before and after administration. The time of administration were carefully checked and recorded. The patients were not allowed to urinate until 2 hrs post I-131 administration. Imaging/blood sampling were performed at 1, 2, 4, 24, 48, 72, 96, and 120 hrs post-administration. Each imaging/blood sampling consisted of planar anterior/posterior whole-body scan, blood sampling and regional SPECT/CT.

The whole-body scans were acquired using SPECT/CT scanners of 9.5-mm-thick crystals (NMCT670 or NMCT670pro, GE) equipped with high-energy general purpose collimators and the scan speeds were adjusted to the time lapse post I-131 administration: scan speed of 30 cm/min for day 1 (1, 2, and 4 hrs), 17 cm/min for day 2 (24 hrs), and 10 cm/min for days 3-6 (48, 72, 96, and 120 hrs). The whole-body counts were normalized by the scan speeds. Immediately after the whole-body scan acquisition, blood samples (2.5-3.0 mL per venipuncture) were collected in ethylene-diamine-tetraacetic acid (EDTA)-coated tubes and duplicated to two plain tubes (1 mL per each) at the time of sampling. All the blood samples were stored in room temperature until the last samples at 120 hrs were acquired. Then, gamma counting for the I-131 radioactivity in the blood was performed using a gamma counter (Automatic Gamma Counter, HIDEX, Finland) for 30 minutes per sample tube. The measured counts were normalized by the blood volume, yielding counts per minute (CPM) per mL, and then transformed to radioactivity using the counting efficiency of the gamma counter (44.0%), resulting in mCi per mL.

Without any delay after the blood sampling, quantitative SPECT/CT images were acquired using the same SPECT/CT scanners covering from the neck to the pelvis. In brief, typical quantitative SPECT images were acquired/reconstructed with CT attenuation correction, triple-energy window scatter correction, and resolution recovery upon the dedicated quantitative software (Q.Volumetrix AI, Xeleris version 5.0, GE).

Blood absorbed dose by conventional method

The gamma counting was performed in a single session when all the blood samples were collected. The gamma counts (CPM/mL) of the duplicated samples were averaged first and then transformed to I-131 radioactivity (mCi/mL) using the previously determined gamma counter efficiency (44.0%). The I-131 fraction of 1

mL blood over the administered activity was plotted against time, which was used for the estimation of blood-to-blood absorbed dose by beta-particles (Figure 3.1A). The whole-body scan counts of anterior and posterior planar images were adjusted to the scan speed and background corrected. Then the geometric mean values of the anterior and posterior planar images were obtained. The geometric mean values at the time of 1 hr post-administration were set to be equivalent to the administered I-131 activity with decay correction, and other geometric mean values afterwards were transformed to radioactivity in reference to the 1-hr geometric mean values. The I-131 fraction of the whole-body radioactivity over the administered activity was also plotted like the blood fraction, which was employed for the calculation of the whole-body-to-blood absorbed dose by gamma-rays (Figure 3.1B).

The area-under-the-curves (AUCs) of the I-131 fraction for 1 mL blood and whole body were obtained through a mono-exponential curve-fitting of the respective time-activity-curves (TACs) resulting in $\tau_{\text{mL blood}}$ and $\tau_{\text{whole body}}$, respectively (Figure 3.1). $\tau_{\text{mL blood}}$ is the residence time of I-131 in 1 mL blood and $\tau_{\text{whole\_body}}$ is that in the whole body.

Then the blood absorbed dose (D_{blood}) per unit I-131 radioactivity (A_0) was calculated using the following equation as suggested by the European Association of Nuclear Medicine (EANM) (*66*).

$$\frac{D_{blood}}{A_0}\left[\frac{Gy}{GBq}\right] = 108 \times \tau_{mL\_blood}[hrs] + \frac{0.0188}{(wt[kg])^{2/3}} \times \tau_{whol\ \_body}[hrs]$$

Residence time calculation for conventional blood absorbed dose measurements

The residence time, the total number of decays per unit administered activity, was calculated using mono-exponential curve fitting. The I-131 fraction of 1 mL blood from gamma counting and the I-131 fraction of whole body from whole-body scans were plotted against time, resulting in their respective TACs. Through mono-exponential curve fitting using spreadsheet software (Excel 2016, Microsoft), single exponential regression lines (dotted red) were obtained, and the AUC was calculated by the ratio of the intercept to the negative exponent. In the following example (case no. 5), the I-131 residence times for 1 mL blood ($\tau_{\text{mL blood}}$) and whole body ($\tau_{\text{whole body}}$)were 0.0011 hrs and 45.7 hrs, respectively.

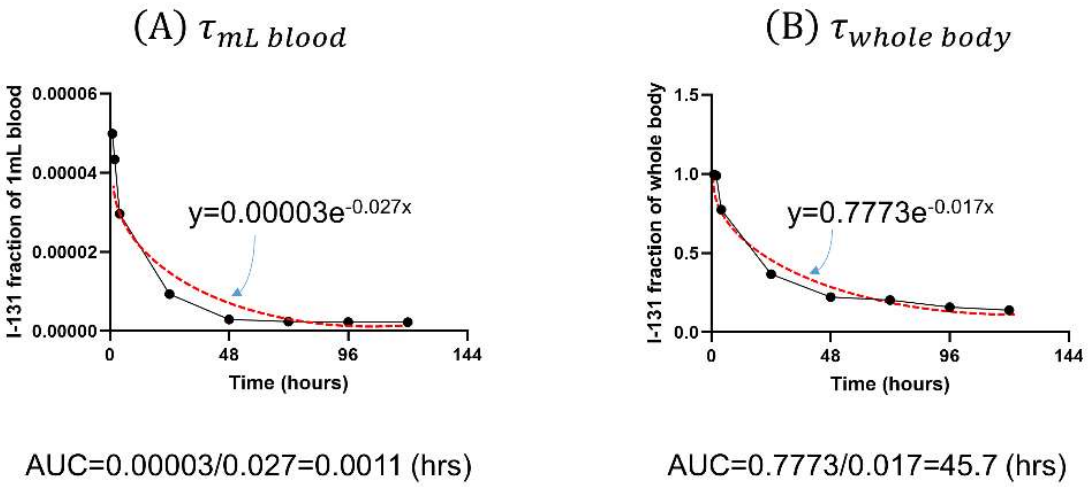

Figure 3.1. How to calculate the residence times of I-131 for 1 mL blood (A) and whole body (B).

How to place volume-of-interests (VOIs) for blood pool over the ascending aorta the CT of SPECT/CT images

Blood pool I-131 radioactivity in the quantitative SPECT/CT images was measured by placing volume-of-interests (VOIs) over the ascending aorta of CT images, where the blood pool was readily identified. The inside of left ventricle was not considered for blood pool segmentation because, without iodine-contrast enhancement, the blood pool and ventricular muscle could not be differentiated from each other

How to draw volume-of-interests (VOIs) for tumours in quantitative SPECT/CT images

The expert (DGO), a board-certified nuclear medicine physician, manually drew VOIs over the individual metastatic tumours using quantitative SPECT/CT images. The manual organ segmentation tool from the vendor-provided software (Q.Volumetrix AI, GE) on a workstation (Xeleris version 5.0, GE) was used for these tasks. The same shape and volume were maintained for a given tumour lesion, but the VOI location was slightly adjusted in images from different time points to account for inevitable motion/position changes during multiple time point image acquisitions.

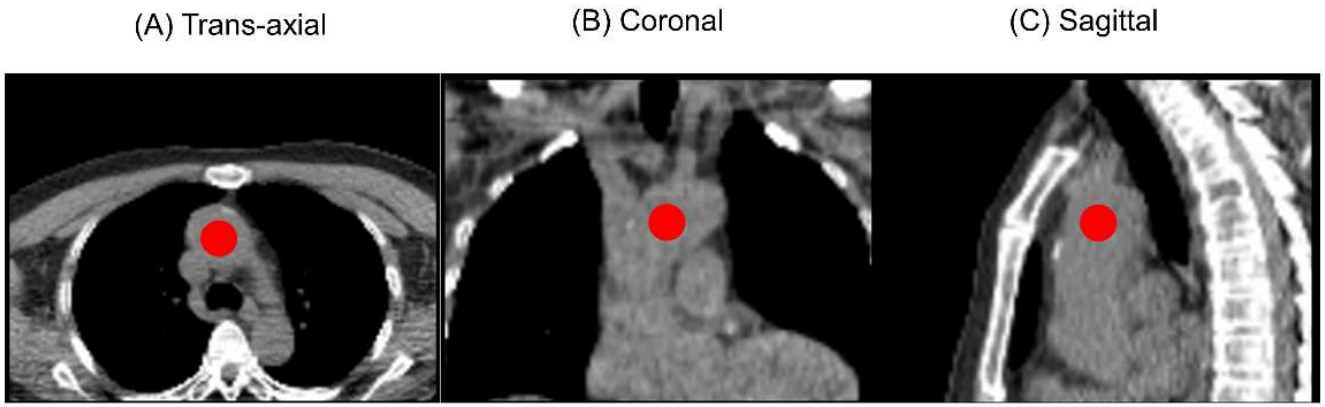

Figure 3.2. How to place VOIs for blood pool (red spheres) in the trans-axial (A), coronal (B), and sagittal (C) CT images.

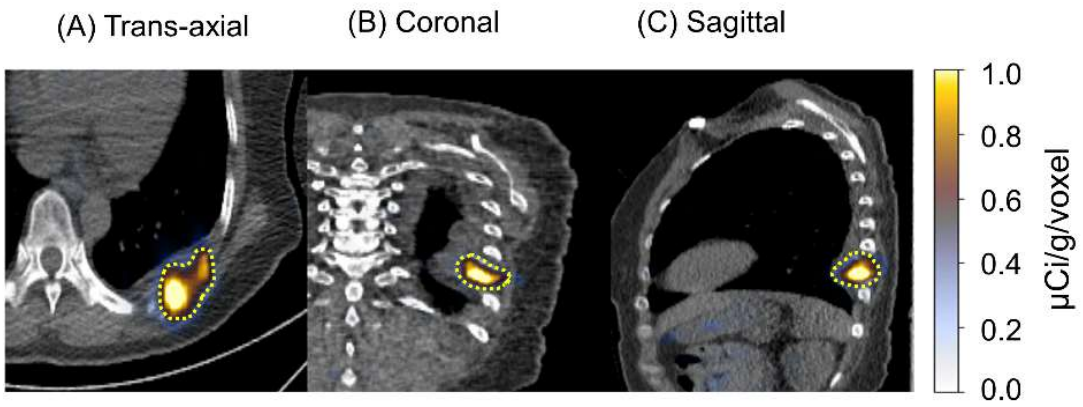

Figure 3.3. How to draw VOIs for tumours (yellow dotted lines) in the trans-axial (A), coronal (B), and sagittal (C) SPECT/CT images.

Reproducibility and accuracy of SPECT/CT for I-131 blood pool activity

The blood pool I-131 radioactivity in vivo on the quantitative SPECT/CT images was repetitively measured to prove that the SPECT/CT-derived radioactivity measurement is reproducible and accurate. This process was redundant in terms of blood absorbed dose calculation because blood I-131 radioactivity was already available by gamma counting of the blood in vitro but considered essential because the reliability of the quantitative SPECT/CT is the cornerstone for tumour absorbed dose calculation.

To obtain blood pool I-131 radioactivity, spherical volume-of-interests (VOIs) were drawn on the CT images of SPECT/CT at the centre of the ascending aorta by three investigators (DGO, JHK, and JY) who were nuclear medicine specialists (Figure 3.2). These manual drawings were tested for the reproducibility of blood pool I-131 radioactivity measurement as inter-operator agreements in the SPECT/CT. For the accuracy of I-131 radioactivity measurement, the residence time of 1 mL blood ($\tau_{ml\ blood}$) from the SPECT/CT (mean values of the 3 investigators) was compared with that from the blood gamma counting.

Tumour I-131 concentration by SPECT/CT

Using the SPECT/CT images reconstructed on the vendor-provided quantitative software (Q.Volumetrix AI, GE), the absolute radioactivity concentrations of individual tumours were measured by the expert nuclear medicine physician (DGO), who manually drew VOIs over metastatic tumour lesions (Figure 3.3). The volumes and shapes of the VOIs were kept constant for a given lesion from the 1-hr to the 120-hr time-point SPECT/CT images using the copy-and-paste function of the software, but their locations were individually adjusted to ensure that the exact lesions were analysed. The measured lesion volume (mL) was converted to lesion mass (gram) by multiplying the volume by 1.03. The measured I-131 concentrations of tumours (μCi/g) were plotted against time. Then, the AUCs for the integrated I-131 concentration (μCi/g·hrs) were obtained for the individual tumours.

Monte-Carlo simulation

The Monte-Carlo simulation was performed to estimate the ground truth absorbed doses of blood and tumour from the SPECT/CT images. The simulation was conducted using the Geant4 toolkit (version 4.11.0.3, CERN), a widely-used simulation software for particle-matter interaction, on the computer hardware conditions of Ryzen7 5800X CPU and 4x DDR4 16 GB memory. As a simulation setup, the source was defined as radiotracer distribution from the SPECT DICOM images, randomly generating primary particles of I-131 and the scoring target was the CT DICOM images harboring both Hounsfield unit value for material and voxel

spacing information for geometry. The conversion of the Hounsfield unit values to tissue parameters followed a typical example (*72*). The physics list employed was QGSP-BIC-HP with electromagnetic option 4.

The number of events for I-131 particle generation was determined to be 2 million because the absorbed dose per event (Gy/event), measured in the blood pool VOIs, showed an acceptable coefficient of variation (i.e., <5%) in preliminary uncertainly tests (n=30) (Figure 3.4). The simulation outcomes (Gy/event) were multiplied by the total number of decay events over 1 hr from the respective SPECT, resulting in the absorbed dose rate (Gy/hr), which were used for the generation of dose map.

To validate the dose rate maps, a comparative analysis with TOPAS (version 3.8) was performed using structural similarity index measure (SSIM) and normalized root mean square error (NRMSE) to assess consistency and reliability.

Simulation uncertainty tests

In preliminary sessions of the Monte-Carlo simulation, we tested the %coefficient of variation (CV) of blood absorbed doses under four different conditions of event numbers (i.e., 1 million, 2 million, 4 million, and 8 million), with each condition being simulated 30 times using different random seeds. The simulation voxel spacing was 0.9766 mm with a slice thickness of 2.5 mm. Additionally, the QGSP_BIC_HP physics list with the EM option 4 was applied. The physics range cut was set to 0.001 mm.

The VOIs drawn by one of the nuclear medicine specialists (DGO) on CT images for blood pool I-131 measurement were applied to the four different simulation conditions for I-131 particle generation. The CV was as high as 5.38% for 1 million particle generation with just a 19-minute simulation run time. This decreased to 2.90% for 2 million particle generation with a 31-minute run time. Further increasing the number of generated particles up to 8 million reduced the CV to 1.70%, but the run time drastically increased to 100 minutes. Thus the optimal number of I-131 particle generation was set to 2 million, achieving a CV of less than 5% with a reasonable run time of 31 minutes.

The possible other sources of uncertainty include the detection probability of the SPECT scanner, mis-registration between SPECT and CT images, and voxel level variations.

Table 3.5. Preliminary tests for optimal simulation conditions

No. of events		1 million	2 million	4 million	8 million
Absorbed dose of blood (Gy/event)	Average	1.60E-11	1.59E-11	1.62E-11	1.62E-11
	Standard deviation	8.60E-13	4.60E-13	3.53E-13	2.74E-13
Coefficient of variation (%)		5.3796%	2.9029%	2.1750%	1.6956%
Run time (min)		19	31	53	100

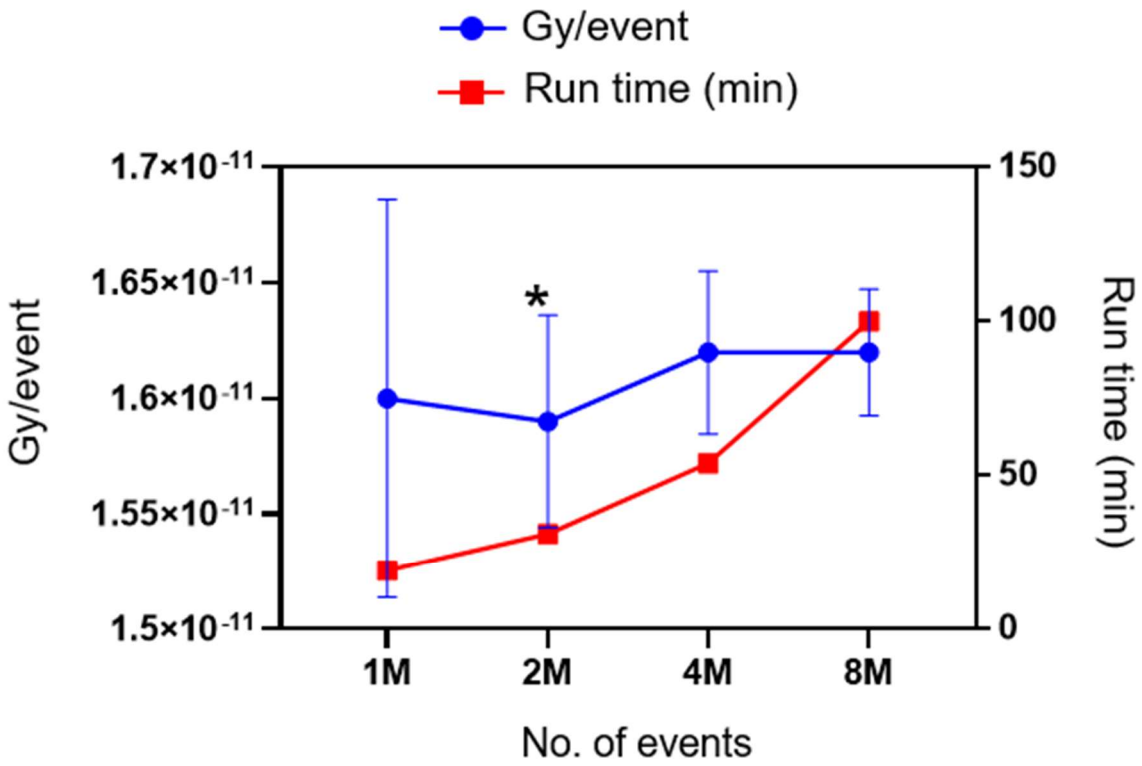

Figure 3.4. Preliminary stimulation tests for the optimal number of I-131 particle generation (*).

AUC calculations for tumour I-131 radioactivity concentration and absorbed dose rate

The curve fitting for tumour AUC was performed based on two types of curve patterns: tumour-proper type and blood-like type. The curve pattern was dichotomized by the time point of the maximum peak. If the maximum peak occurred early (≤ 4 hrs), it was labeled as blood-like, and mono-phasic curve fitting was applied. If the maximum peak occurred late (> 4 hrs), it was labeled as tumour-proper, and bi-phasic curve fitting was employed.

The tumour-proper type was observed in 11 individual tumours with higher I-131 uptake, where the maximum peak occurred around 24-48 hrs. A polynomial model was initially applied to the curve fitting. If the fitting results were unsatisfactory (i.e. R^2 <0.9), a new fitting parameter was iteratively added until the number of parameters (p) was less than the number of samples (n) minus one (i.e. $p < n-1$). If p became equal to or exceeded n-1 (i.e. $p \geq n-1$), exponential curve fitting was used. The ascending phase was successfully fitted in all instances using the polynomial model with an R^2 >0.9. However, the descending phase often required a change (in 6 out of the 11 lesions) from a polynomial to an exponential model to achieve an R^2 >0.9 (Figure 3.5A).

In contrast, the blood-like type, observed in 7 individual tumours with relatively lower I-131 uptake, resembled blood TACs. The peak uptake occurred earlier, typically at 1-2 hrs, and exponential curve fitting applied, with or without a constant term, achieving an R^2 >0.9 (Figure 3.5B). The trapezoidal method was intended to be used when exponential fitting could not achieve an R^2 >0.9. However, only one lesion required the trapezoidal method. Except for this lesion, the fitting model for both I-131 activity concentration and absorbed dose rate had the same number of parameters as the model for other tumour lesions.

Once the model for curve fitting was determined, we explored the tail AUC beyond the final time point. A tangent vector at the last time point was calculated using ROOT (version 6.27/01, CERN) software. If the slope of the tangent vector was not negative, we reverted to the previous time point to calculate the tangent vector. The tail AUC was linearly integrated from the final time point to the point where the tangent vector intersects the x-axis.

In

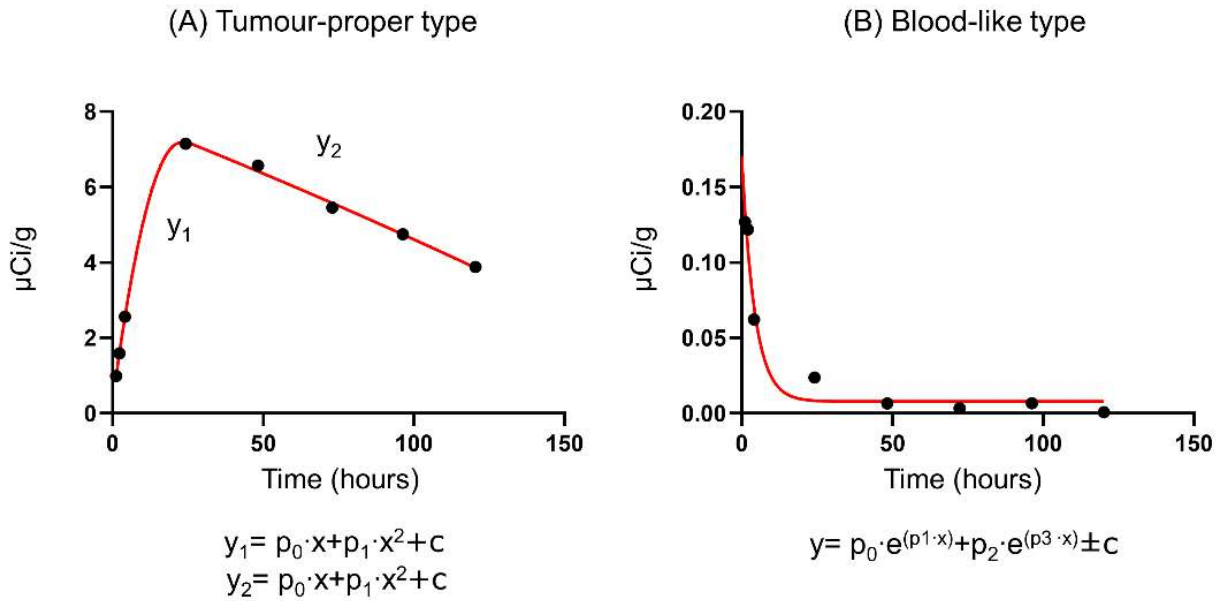

Figure 3.5. Two types of tumour radioactivity concentrations and their curve-fitting methods. (A) tumour-proper type with higher concentrations and (B) blood-like type with lower concentrations.

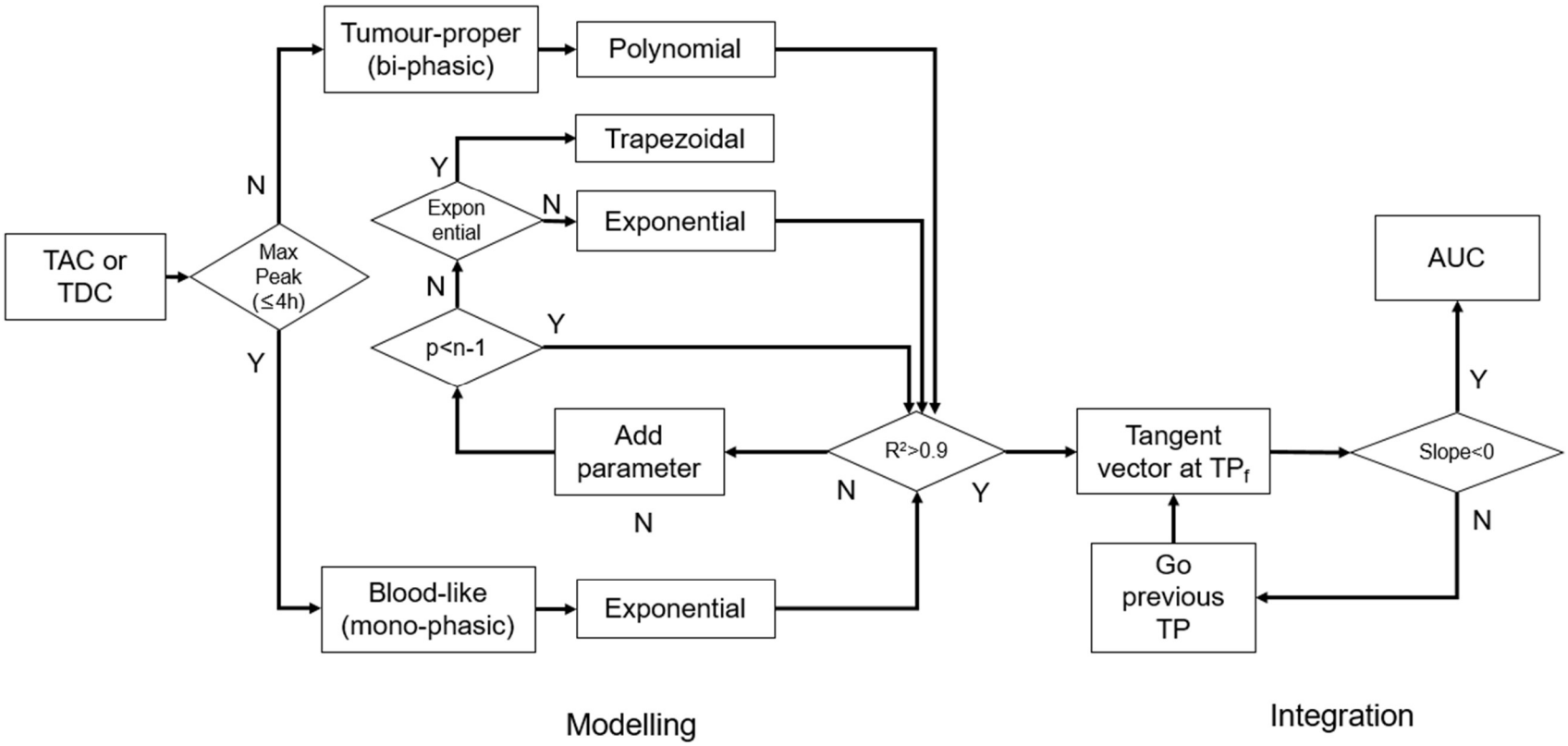

Figure 3.6. Flow chart of curve modelling and integration. TAC, time-activity-curve; TDC, time-dose rate curve; p, number of parameter; n, number of samples; TP, time point; f, final; AUC, area-under-curve.

Transformation of integrated I-131 concentration into absorbed doses for blood and tumour

The VOIs drawn for the blood pool and individual tumours by the expert nuclear medicine physician (DGO) on the quantitative software (Q.Volumetrix AI, GE) (Figure 3.2 and 3.3) were exported from the SPECT/CT as DICOM XML format and then applied to the Monte-Carlo simulation results. This process ensured that the same blood pool area and tumour lesions were used for comparing I-131 activity concentration with absorbed dose.

The AUCs for absorbed dose rate of blood were calculated using mono-exponential curve-fitting (Excel 2016, Microsoft) like the AUCs for I-131 radioactivity fraction of blood/whole body (Figure 3.1). In contrast, the AUCs for tumour absorbed dose rate and radioactivity concentration were obtained using variable curve-fitting algorithms tailored to the pattern of individual curves (ROOT, version 6.27/01, CERN). In brief, when the peak was found at the first 1-or 2-hr time point, exponential curve fitting was applied (blood-like pattern, n=7), whereas with the peak being observed beyond 2-hr time point, the ascending and descending phases were differently fitted using polynomial curve fitting (tumour-proper pattern, n=11) (Figure 3.5). For the descending phase, when either the fitting error was so high or tangent vector at the last time point resulted in greater tail AUC than the I-131 physical decay method, exponential curve fitting was employed. The methods for calculating the AUCs for both I-131 radioactivity concentration and dose rate were the same for a given metastatic lesion with excellent control of fitting errors in all cases (R^2 >0.9).

The relationship between the integrated I-131 concentrations of certain tumours (μCi/g·hrs) (AUC from the I-131 radioactivity concentration curve) and the absorbed doses of the tumours (Gy) (AUC from the dose rate curve) was investigated to generate a linear regression equation.

RAI therapy guided by the I-131 SPECT/CT dosimetry

Three patients received high activity I-131 therapy guided by the I-131 SPECT/CT dosimetry within 3 months. The determination of the I-131 activity followed the restriction rules by the maximum blood absorbed dose (less than 2 Gy) and the maximum whole body activity after 48 hrs post administration without diffuse lung metastasis (less than 120 mCi) (*73*). No patient had lung metastasis in our cohort, thus the limitation of whole body retention to 80 mCi at 48 hrs was not employed (*68*). Other 2 patients were not treated by I-131 because of either poor tumour uptake of I-131 (case no. 2) or the risk of spinal cord compression due to metastatic spinal bone lesion (case no. 4). Ten bone metastatic lesions of 3 patients (case nos. 1, 3, and 5) were used for the response evaluation after high activity I-131 administration guided by the pre-therapeutic SPECT/CT dosimetry. Tumour progression was defined as objective evidence of bone metastasis progression (i.e., pathologic fracture, size increase in MRI, or TG elevation) requiring further treatment, such as surgery, external radiotherapy, or additional RAI therapy.

Statistical analysis

The agreements of VOI drawings of the 3 investigators were assessed using the intra-class correlation coefficients (ICCs). Non-parametric Wilcoxon rank-sum test was used for both the comparison of the I-131 residence time in 1 mL blood (τ_{mL_blood}) between SPECT/CT and gamma counting, and the comparison of the blood absorbed doses between the Monte-Carlo simulation and the conventional EANM method. Kaplan-Meier survival analysis with log-rank test was performed to test differences in tumour progression according to the expected tumour absorbed doses. P value of less than 0.05 was considered statistically significant. Statistical software (MedCalc version 22.023, MedCalc Software Ltd.) was used for the analyses.

Results

In this study, five thyroid cancer patients (three females and two males, mean age 66.2 years, range 54-84) with multiple bone metastases underwent pre-therapeutic dosimetry assessments of quantitative I-131 SPECT/CT and blood sampling at 1, 2, 4, 24, 48, 72, 96, and 120 hrs post-administration of I-131. A total of 38 paired blood sampling measurements and quantitative SPECT/CT scans were collected for analyses as one patient (case no. 1) missed the 72-and 96-hr post-administration sampling/imaging.

Reliability of SPECT/CT

Overall, the blood pool I-131 activities measured by SPECT/CT were well-matched with those obtained by blood sample gamma counting. A nuclear medicine specialist (DGO) drew volume-of-interests (VOIs) over the ascending aorta in the CT of the SPECT/CT images.

The I-131 radioactivity concentrations (μCi/mL) of the blood pool were well-matched between SPECT/CT in vivo and gamma counting in vitro in all 5 cases (Figure 3.7) and the overall agreements by the 3 investigators for all the time points were excellent (Figure 3.8A). The intra-class correlation coefficient (ICC) of blood pool I-131 activity for the agreement of VOI drawing among the three nuclear medicine specialists was 0.977, indicating an extremely high level of agreement (n=5, 95% confidence interval = 0.960-0.987, $p<0.001$).

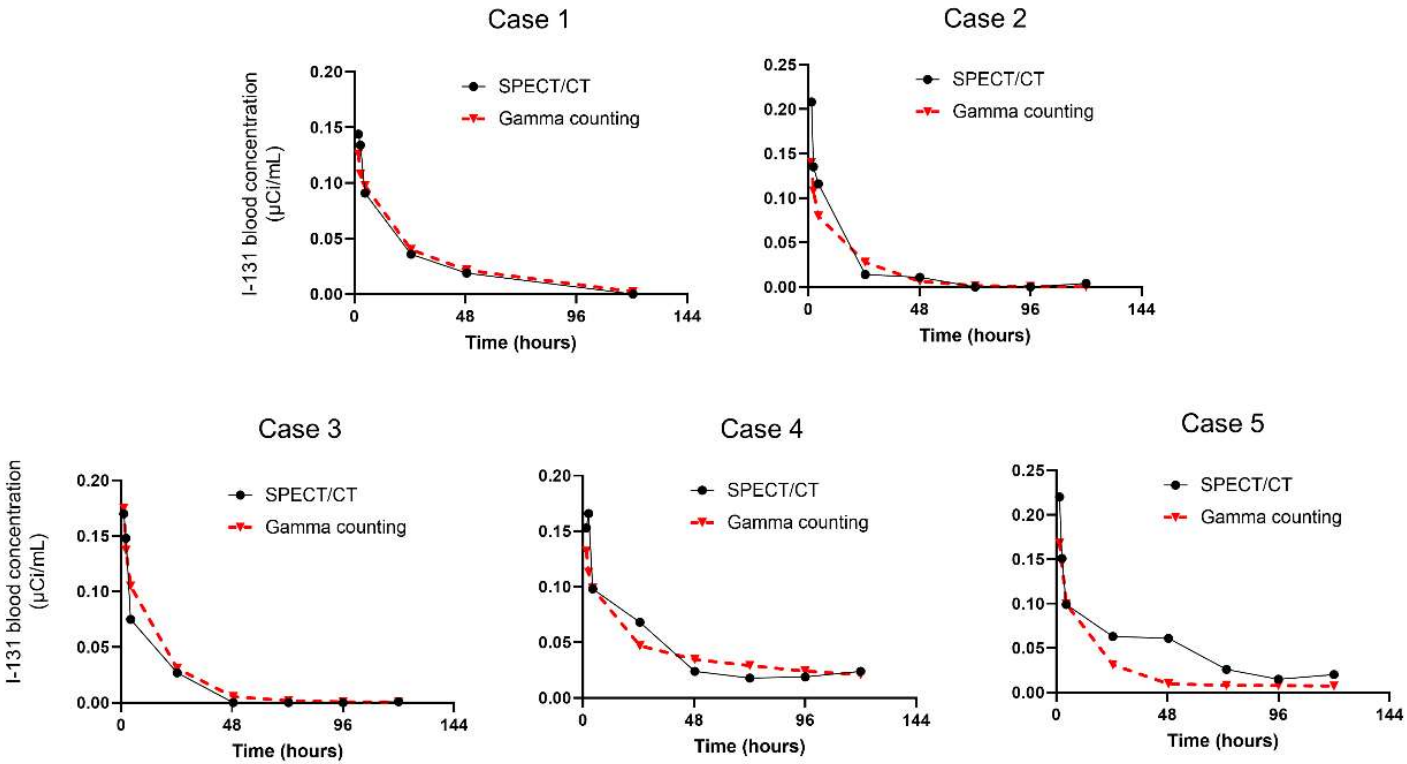

Figure 3.7. Agreements of blood I-131 radioactivity concentrations between the quantitative SPECT/CT and blood sample gamma counting in all 5 cases.

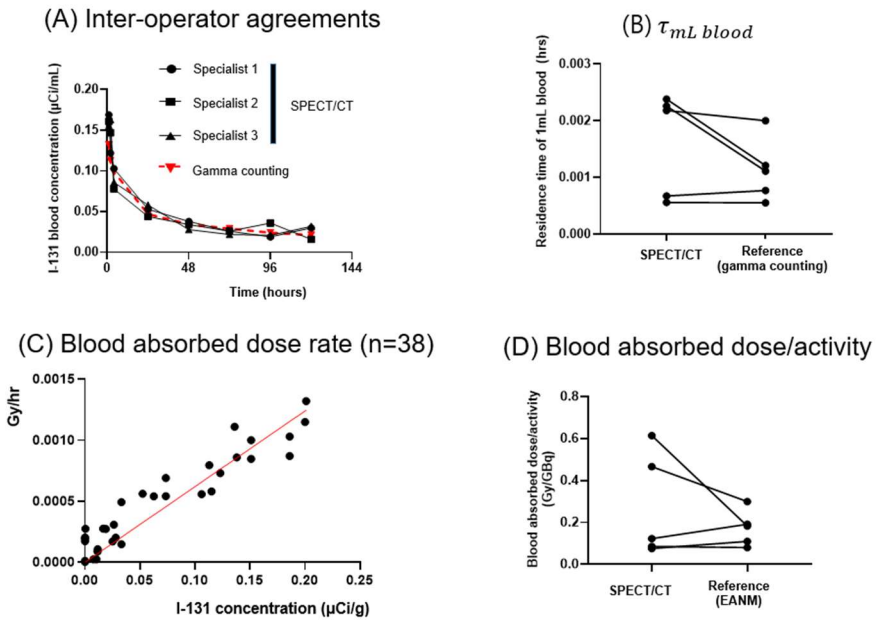

Figure 3.8. Reliability of SPECT/CT for blood RAI concentration measurement. (A) Inter-operator agreements of blood pool I-131 radioactivity measurement by 3 nuclear medicine specialists with reference to blood sample gamma counting (case number 4), (B) Residence time of 1mL blood (τ_{mL_blood}) (n=5), (C) I-131 radioactivity concentration (μCi/g) vs. absorbed dose rate (Gy/hr) (n=38 time points of the 5 patients), and (D) Blood absorbed dose/activity (n=5). EANM (European Association of Nuclear Medicine).

Blood absorbed dose by SPECT/CT

The residence time for I-131 activity in 1 mL blood (τ_{mL_blood}) in the 5 patients was calculated from the respective TACs for both SPECT/CT and blood sample gamma counting methods (Figure 3.8A). The mean $\tau_{mL\ blood}$ measured by the 3 specialists over the SPECT/CT images was 0.00127±0.00073 hrs, while the $\tau_{mL\ blood}$ from blood sample gamma counting was 0.00147±0.00091 hrs (Figure 3.8B). The blood absorbed dose per unit administered activity (D_{blood}/A_0) were measured for each method that the SPECT/CT (Monte-Carlo simulation) (0.2731±0.2502 Gy/GBq) and the conventional EANM method (*66*) (0.1724±0.0847 Gy/GBq) (Figure 3.8D). The relatively higher blood absorbed doses by the SPECT/CT (Monte-Carlo simulation) in the 2 cases (Figure 3.8B) could be attributed to the presence of high activity metastatic bone lesions (C6/right 2nd rib for case 4 and sternum/T6/T10 for case 5) close to the VOI location for the blood pool segmentation (Figure 3.9). With a low activity tumour around the blood absorbed dose measurement point, the Monte-Carlo simulation and conventional EANM method resulted in comparable blood absorbed doses (Figure 3.10). Additionally, strong correlation was observed between blood concentration at each time point and blood absorbed dose rate (Figure 3.8C).

$$Y\ \left(\frac{Gy}{hr}\right) = 0.0062 \cdot X\left(\frac{\mu Ci}{g} \cdot hrs\right), (R^2 = 0.8734, n = 38)$$

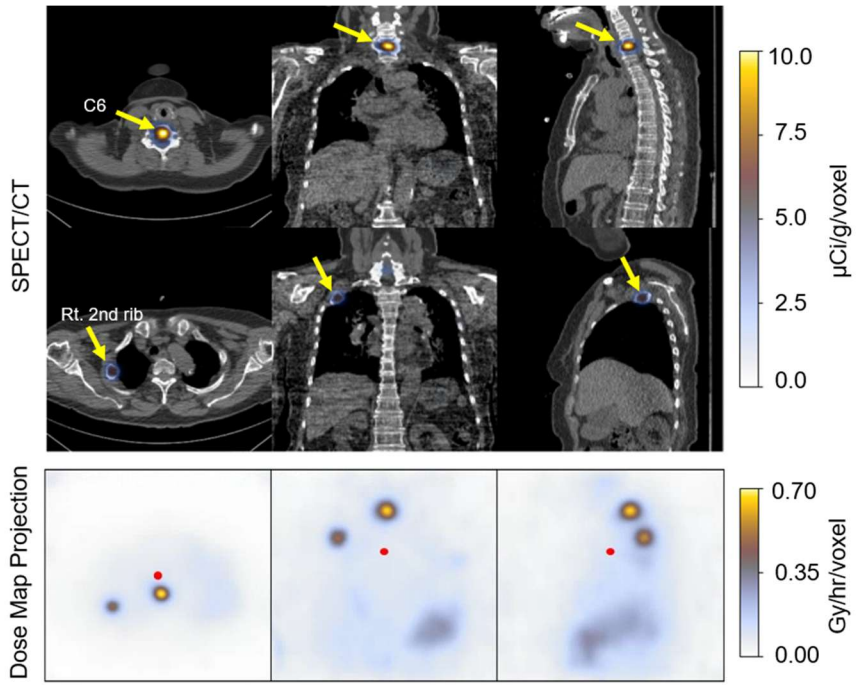

Figure 3.9. Higher blood absorbed dose (0.47 Gy/GBq) in the dose map from the Monte-Carlo simulation (bottom row) compared to the conventional reference method (0.30 Gy/GBq) could be attributed to the presence of two metastatic lesions with high uptake (C6 and right 2nd rib, yellow arrows in the SPECT/CT) close to the site of blood pool segmentation (red spheres) in the dose map (case no. 4 at 24 hrs post administration).

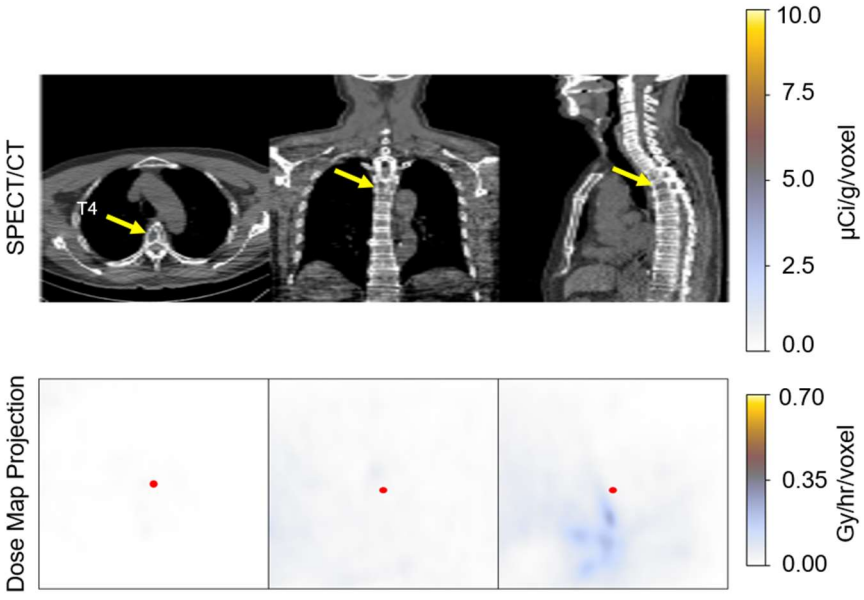

Figure 3.10. Blood absorbed dose by the Monte-Carlo simulation (0.12 Gy/GBq) was comparable to that by the conventional reference method (0.19 Gy/GBq) in this case. The metastatic tumour in the T4 (yellow arrows in the SPECT/CT) had low I-131 uptake and negligible contribution to the blood absorbed dose (red spheres) (case no. 1 at 1 hr post administration).

Tumour absorbed dose by SPECT/CT

There were 18 bone metastatic lesions from the 5 patients (Table 1). The I-131 uptake pattern could be classified as either tumour-proper type (n=10) (Figure 3.11) or blood-like type (n=8) (Figure 3.12). High agreements of curves were observed between the absorbed dose rates (Gy/hr) and I-131 concentrations (μCi/g), regardless of the type. AUCs were calculated for the integrated I-131 activity concentrations and absorbed doses (Figure 3.5 and 3.6). As a result, the integrated I-131 activity concentrations of the 18 lesions were 266.5352±375.0844 μCi/g·hrs (range: 1.5738–1260.9456 μCi/g·hrs), whereas the tumour absorbed doses by the Monte-Carlo simulation were 1.2669±1.7337 Gy (range: 0.0006–5.4720 Gy).

The simple linear regression generated an equation for the estimation of tumour absorbed dose from the integrated I-131 concentration of SPECT/CT (Figure 3.13).

$$Y\ \ (Gy) = 0.0046 \cdot X\left(\frac{\mu Ci}{g} \cdot hrs\right), (R^2 = 0.9760, n = 18)$$

$$Y\ \ \left(\frac{Gy}{hr}\right) = 0.0046 \cdot X\left(\frac{\mu Ci}{g}\right), (R^2 = 0.9918, n = 140)$$

where Y was the tumour absorbed dose or absorbed dose rate and X the integrated radioactivity concentration or radioactivity concentration.

The tumour-proper type had significantly higher values and wider range than the blood-like type, and the equation was mainly generated out of the data of the tumour-proper type (range [min-max]: 0.0407-5.472 vs 0.0102-0.0317, tumour proper vs blood like, respectively) (Figure 3.13).

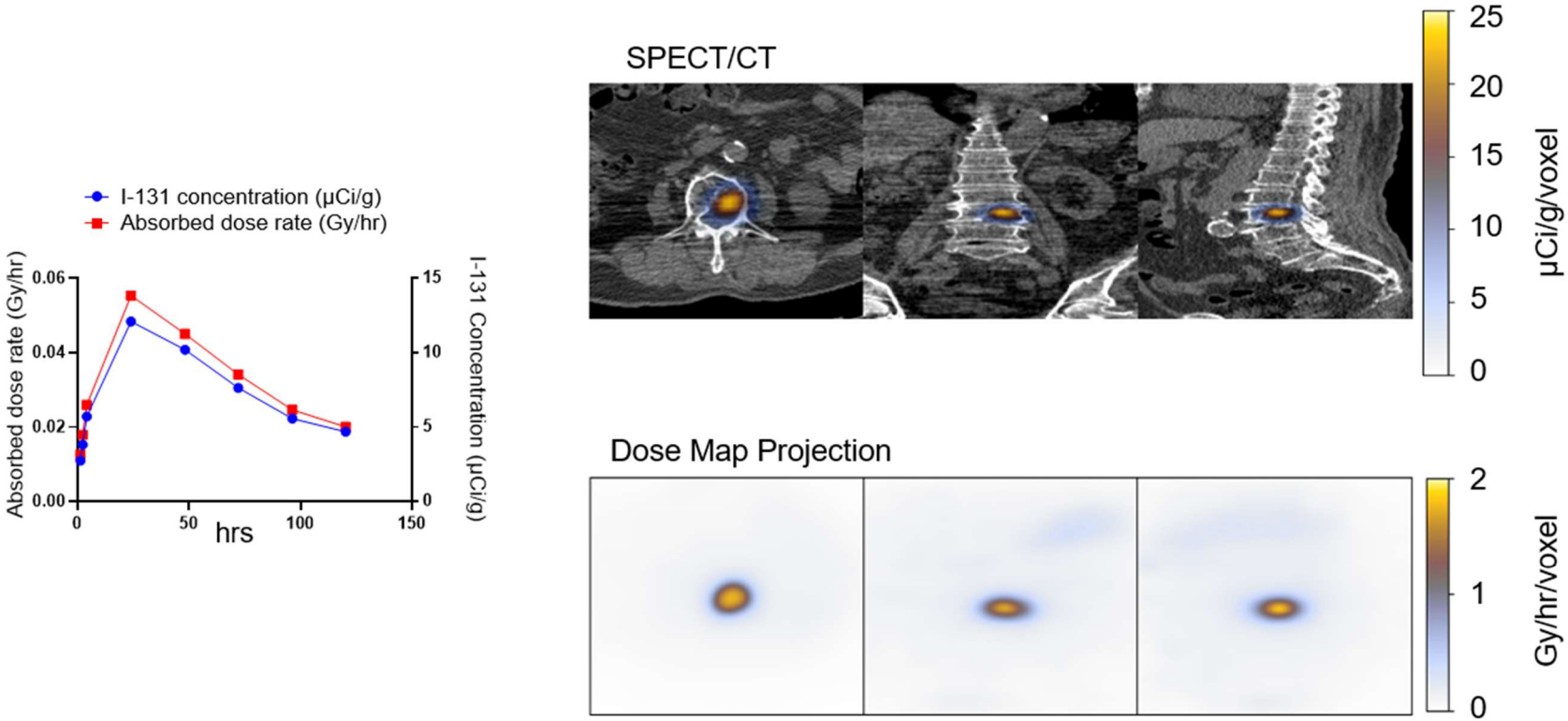

Figure 3.11. Tumour-proper type (L3 of case no. 4). SPECT/CT and dose map were at 24 hrs post administration.

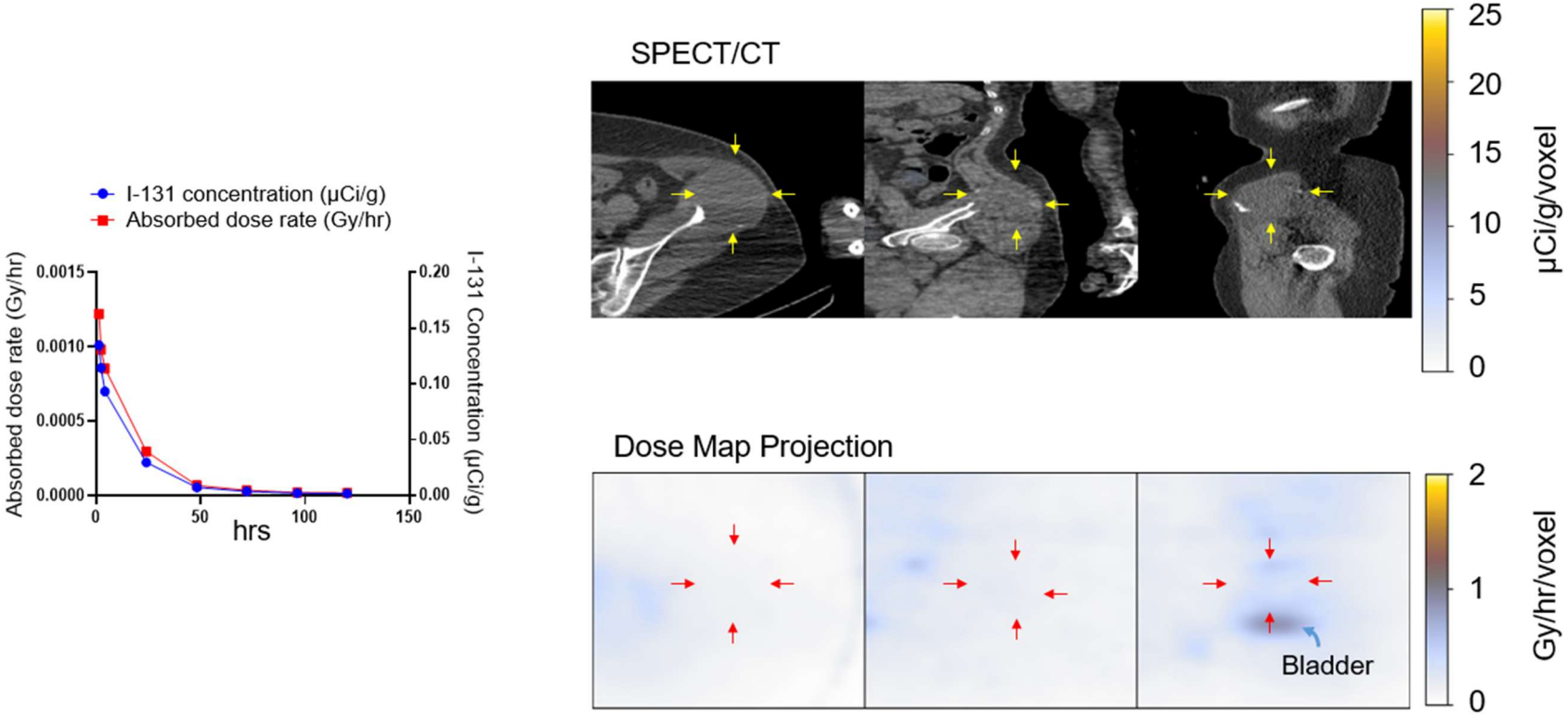

Figure 3.12. Blood-like type (left ilium of case no. 3). SPECT/CT and dose map were at 1 hr post administration.

.

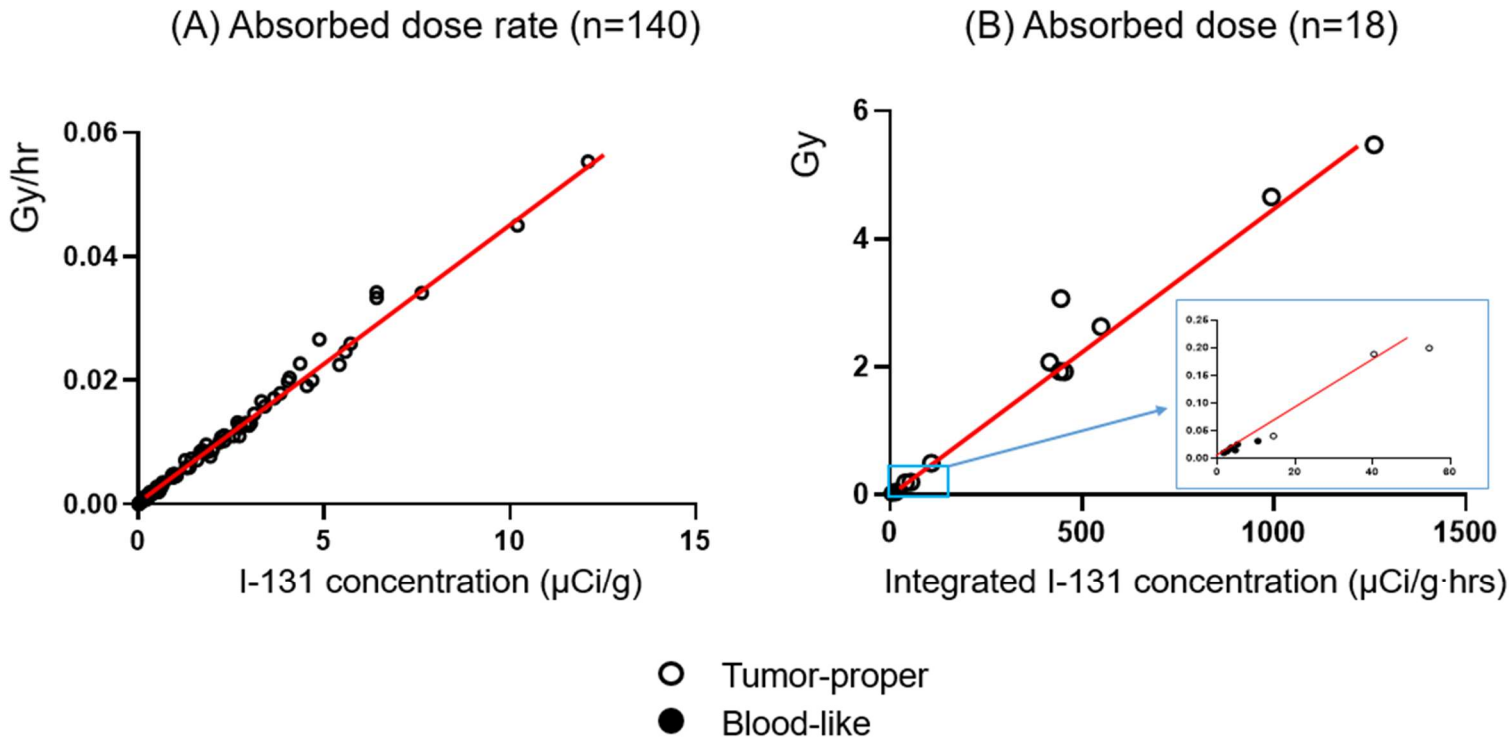

Figure 3.13. Tumour absorbed dose by SPECT/CT. (A) I-131 radioactivity concentration (μCi/g) vs. absorbed dose rate (Gy/hr) (n=140 time points of the 18 tumour lesions), and (B) Integrated I-131 radioactivity concentration (μCi/g·hrs) vs. absorbed dose (Gy) (n=18 tumour lesions).

Validation of simulation results

Table 3.6 Comparison of dose rate maps: SSIM and NRMSE metrics for whole image and VOI

	Whole image	Blood pool	Tumour
SSIM[a]	0.9917±0.0091	0.9837±0.0208	0.7036±0.3363
NRMSE[b]	0.0038±0.0022	0.1359±0.1503	0.0688±0.0259

a: structural similarity index measure

b: normalized root mean square error

Date are mean±standard deviation.

The dose rate maps of Geant4 and TOPAS were hard to distinguish at the image level (Figure 3.14). In SSIM, indicating a very high level of consistency across the whole image. This suggests that the general structures and numerical values between the two simulations are in close agreement. However, specific region showed lower agreement copmared to those for the whole image. In the tumour VOI, there was a moderate level of agreement. In contrast, the blood pool VOI exhibited a higher level of consistency and agreement (Table 3.6).

Positive correlations were observed between Geant4 and TOPAS dose rate in specific VOI (tumour VOI: R^2=0.9332, p<0.0001, n=140; blood pool VOI: R^2=0.9868, p<0.0001, n=38)

$$\text{tumour dose rate: } Y\left(\frac{\text{Gy}}{\text{hr}}\right) = 1.1156 \cdot X\left(\frac{\text{Gy}}{\text{hr}}\right)$$

$$\text{blood dose rate: } Y\left(\frac{\text{Gy}}{\text{hr}}\right) = 0.9976 \cdot X\left(\frac{\text{Gy}}{\text{hr}}\right)$$

Where Y represents dose rate from TOPAS, and X represents dose rate from Geant4. In tumour dose rate, the slope of 1.1156 represents approximately 12% higher result from TOPAS. In blood dose rate, the slope close to 1 in the correlation indicates that both simulation predict nearly identical. Furthermore, both linear equation exhibited only small deviation.

Finally, correlation between radioactivity concentration and dose rates, the R^2 value for the TOPAS was 0.9487, while for Geant4 it was 0.9918. This indicates that Geant4 provides a higher level of agreement in correlation with radioactivity concentration.

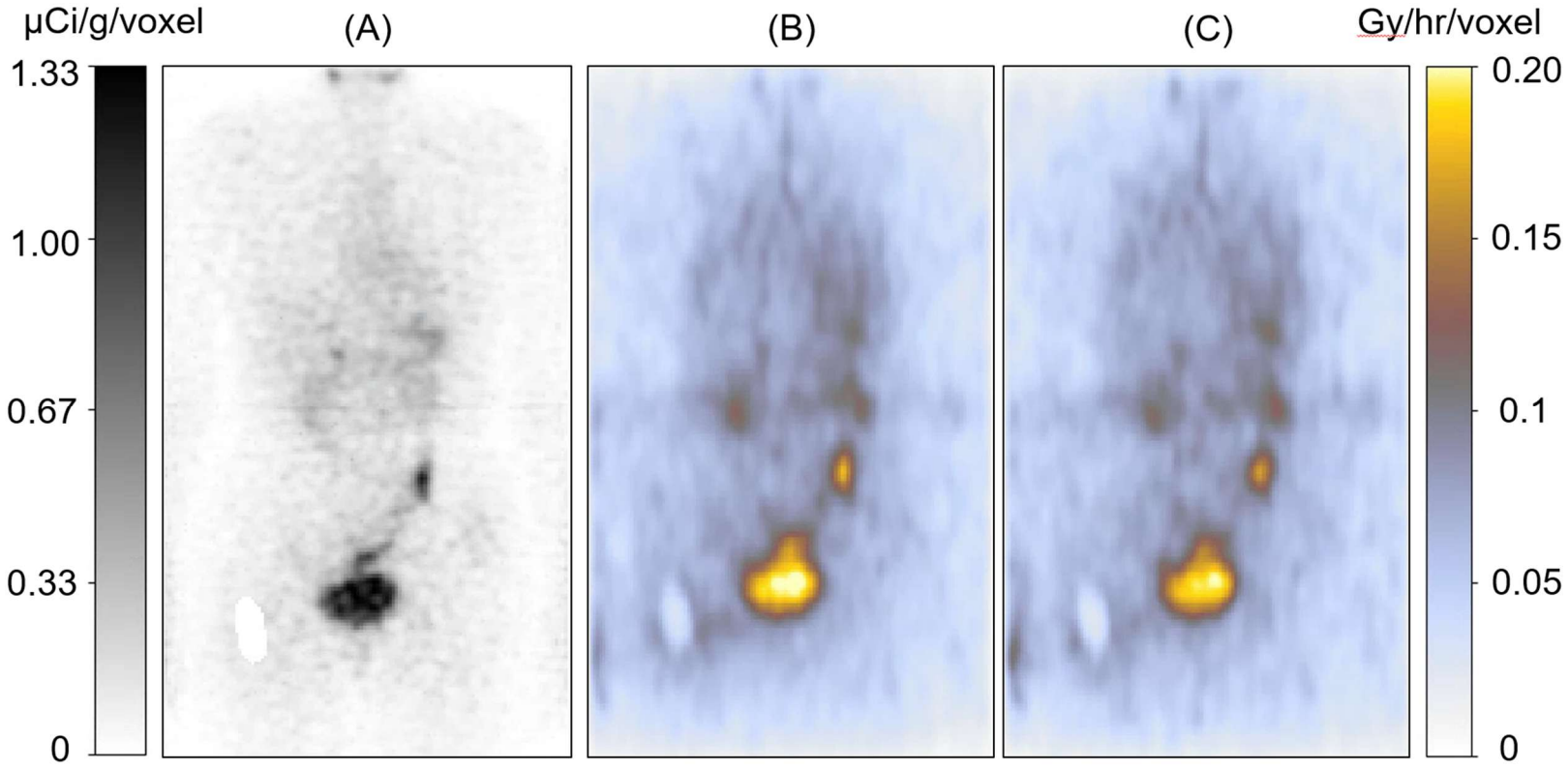

Figure 3.14. The comparison of Monte Carlo simulation toolkits between the Geant4 and TOPAS. (A) Projection of original SPECT image in coronal view. Projection of dose rate maps in coronal view: (B) Geant4, (C) TOPAS: Tool for Particle Simulation.

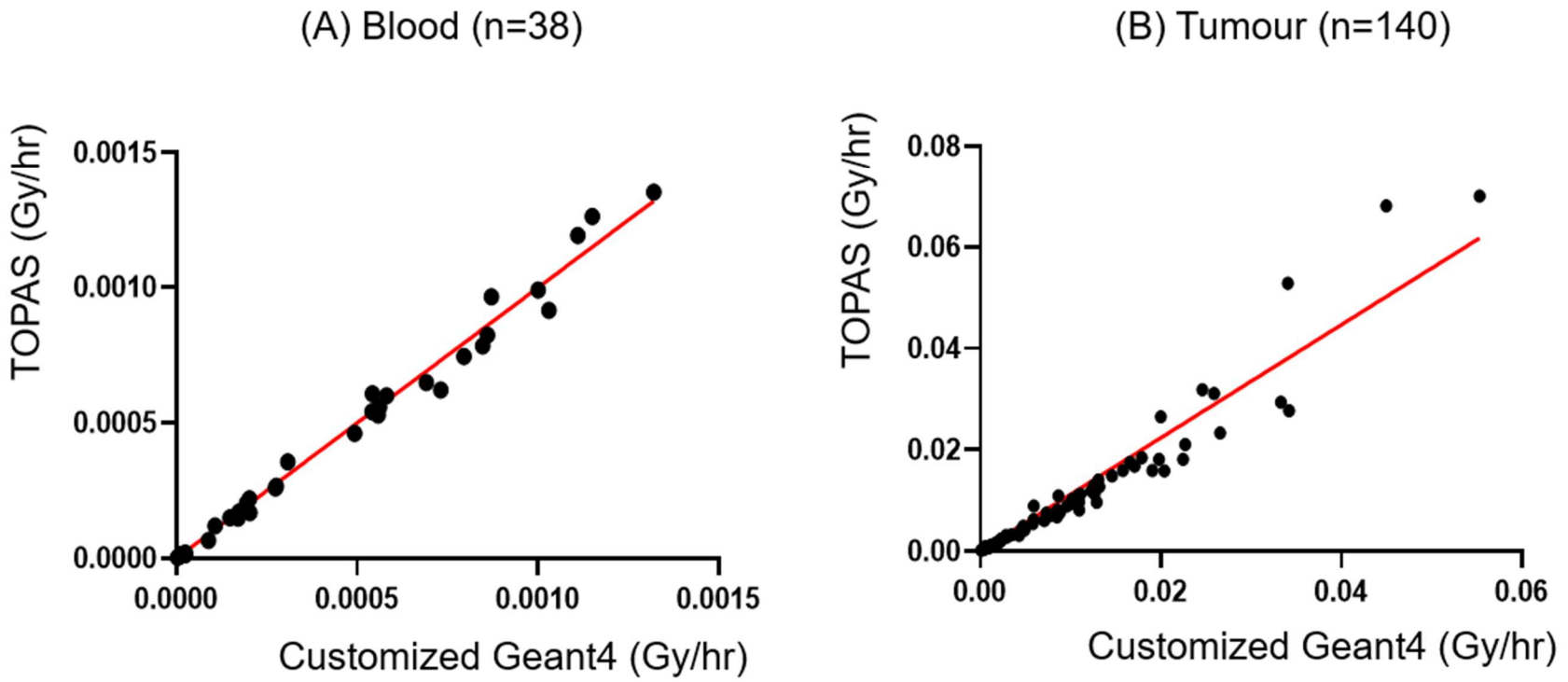

Figure 3.15. The correlation of absorbed dose rates between the customized Geant4 and TOPAS for blood (A), and tumour (B). TOPAS: Tool for Particle Simulation.

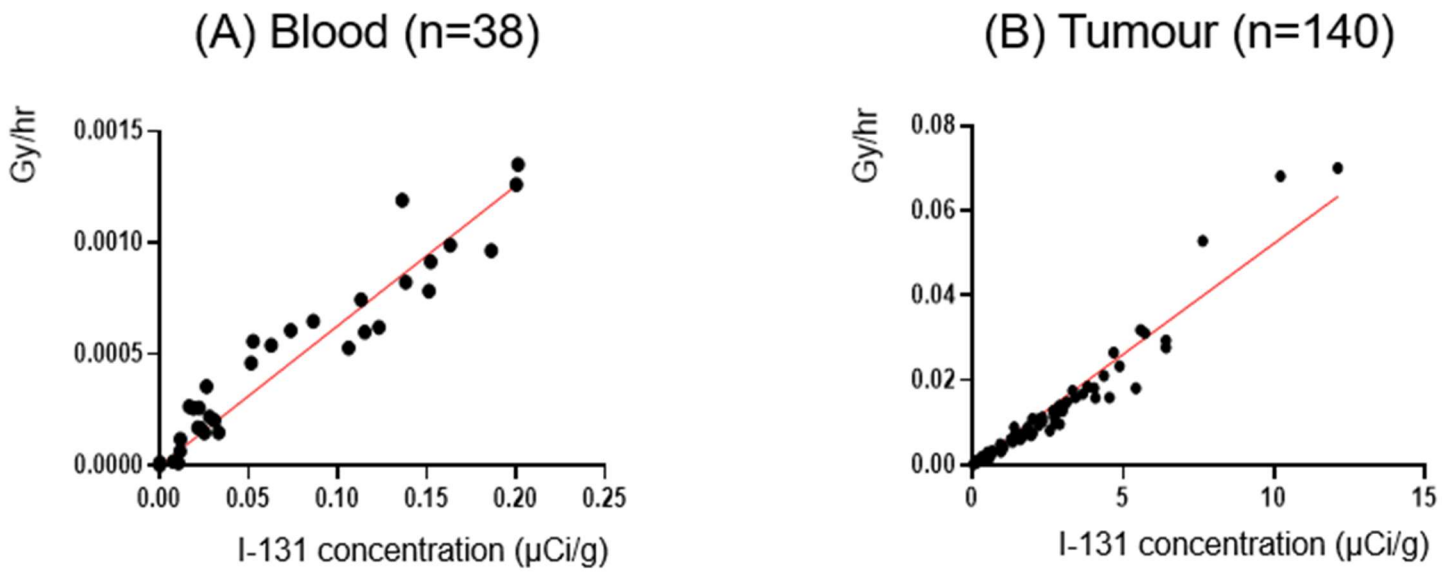

Figure 3.16 The correlations between radioactivity concentrations and absorbed dose rates by TOPAS for blood (A) and tumor (B). TOPAS: Tool for Particle Simulation.

Discussion

The findings from this study underscore the potential of quantitative SPECT/CT as a trustworthy method for the measurement of tumour absorbed doses in thyroid cancer patients with multiple bone metastases. The I-131 activity concentrations in the blood pool were measured reproducibly and accurately in the SPECT/CT. Tumour absorbed doses, calculated by Monte-Carlo simulation, could be predicted by the integrated I-131 concentration of the tumour.

The I-131 radioactivity concentrations in the blood were up to 0.2 μCi/mL at the earliest time points and down to 0.002 μCi/mL at the last time points (Figure 3.10 and 3.11), which were substantially lower than those in tumour with typical uptake pattern (more than 10 μCi/g at the peak) (Figure 3.12). The serial measurements of the blood I-131 radioactivity by the SPECT/CT were consistently accurate compared to the gold standard blood sample gamma counting, leading to in-significant difference of residence time from the gamma counting (Figure 3.8A). The high intra-class correlation coefficient (ICC) of 0.977 among the VOI delineations over the blood pool by three operators indicates that the SPECT/CT method was also free from the human errors during the measurement (Figure 3.7). This kind of reliability of quantitative SPECT/CT has never been reported at least for I-131 quantification. We believe that the tumour radioactivity measured by the SPECT/CT would be as reliable as the blood radioactivity.

The radioactivity concentrations in certain lesions must affect their absorbed doses as self-irradiation and beta-particles with short range are the typical example. However, the overall absorbed dose of the lesions may not be affected only by the self-irradiation but also by the remote irradiation from other high active sources around the point of measurement. Gamma-rays from the metastatic tumours close to the ascending aorta are such instances (Figure 3.9 and 3.10). Indeed, the conventional EANM method takes the gamma-ray effect into account for the blood absorbed dose calculation but just whole body counts are used (*66*). Relatively higher blood absorbed doses by the SPECT/CT-derived Monte-Carol simulation (Figure 3.8B) compared to those by the EANM method in the 2 cases with high activity tumours around the blood absorbed dose measurement point (Figure 3.9) may be explained by the difference of gamma-ray sources.

Tumour absorbed doses in the current study were highly correlated with integrated radioactivity concentration (Figure 3.12). The patterns of dose rate curves were almost equivalent to those of radioactivity concentrations (Figure 3.10 and 3.11), which means that the self-irradiation plays the most critical role for the tumour absorbed doses. Then the measurements of the tumour I-131 concentration by the SPECT/CT at multiple time points may be sufficient enough to predict the tumour

absorbed doses (*74*). However, in case of post-RAI therapy with high activity I-131, multiple SPECT/CT acquisitions may not be possible, especially at early time points due to radiation safety concerns to medical staffs. Moreover, high tumour concentration, which would be proportional to the administered high activity for therapy purpose, may overwhelm the count rate performance of the current SPECT scanners, resulting in dead-time count losses. Therefore, pre-therapeutic planning dosimetry using the quantitative SPECT/CT seems to be a reasonable dosimetry approach for thyroid cancer.

In fact, the way of absorbed dose measurement has been investigated intensively in the field of nuclear medicine as internal dosimetry (*77,78*) and thyroid cancer treatment using I-131 internal dosimetry with or without SPECT/CT has been also thoroughly investigated in many institutes (*75,79-86*). Our study may have advantages over other studies in that 1) accurate measurements of radioactivity was realized using the state-of-the-art quantitative SPECT/CT, 2) Monte-Carlo simulation was involved as reference standard for the SPECT/CT, and 3) the kinetics of I-131 was thoroughly investigated by 8 times of blood sampling/imaging up to 6 days post I-131 administration. More delayed time point such as 144 hrs may be needed for the proper evaluation of the late time point AUCs (*67*), which will be performed in our next study.

In the tumour VOI, the moderate agreement observed between Geant4 and TOPAS simulations may be partially attributed to the 12% higher dose values predicted by TOPAS. This discrepancy could be due to differences in the version of the Geant4 physics engine used in the two simulation (11.0.3 vs 10.7.3).

Limitation

This study has serveral limitations. First, the small sample size reduces the statistical power, leading to limited reliability of the findings that comparison of residence time between blood sample gamma counting and blood pool measurement in SPECT/CT, and blood absorbed dose calculation between EANM guideline and Geant4 method. To reduce radiation exposure from CT, additional deep learning-based quantification and tumour segmentation are required.

Conclusion

The quantitative SPECT/CT is a reproducible and accurate method for measuring I-131 activity in blood and tumour, which can be translated into accurate pre-therapeutic dosimetry for bone metastasis of thyroid cancer.

Chapter 4. Conclusion

The application of quantitative SPECT/CT in the fields of deep-learning and dosimetry has led significant advancements demonstrated across the three studies.
First, the development of CT-free quantification for thyroid and kidney successfully replaces the need of CT, thereby reducing radiation exposure from CT scans.
Second, synthetic μ-map-based organ segmentation, supported by SPECT signals, proves effective,significantly reducing both the time and human resources reuiqred for segmentation.
Third, quantitative SPECT/CT measurements are reproducible and accurate. Moreover, the integrated I-131 concentration enable precise estimation of the tumour absorbed dose, with our study confirming threshold as 90 Gy, consistent with previous reports suggesting ranges of 80 or 100 Gy. However, as these results are exploratory and based on data from a single institution, further validation through multi-centre studies is necessary.
Togher, these findings ilustrate the fromasformative potnetial of quantitative SPECT/CT and deep-learning in improving diagnostic accuracy, reducing patient burden, and enhancing the effciency of clinical workflows in nuclear medicine.

Bibliography

1. Bae S, Kang Y, Song YS, Lee WW, Group KS. Maximum standardized uptake value of foot SPECT/CT using Tc-99m HDP in patients with accessory navicular bone as a predictor of surgical treatment. *Medicine (Baltimore).* 2019;98:e14022.

2. Kim J, Lee HH, Kang Y, et al. Maximum standardised uptake value of quantitative bone SPECT/CT in patients with medial compartment osteoarthritis of the knee. *Clin Radiol.* 2017;72:580-589.

3. Suh MS, Lee WW, Kim YK, Yun PY, Kim SE. Maximum Standardized Uptake Value of (99m)Tc Hydroxymethylene Diphosphonate SPECT/CT for the Evaluation of Temporomandibular Joint Disorder. *Radiology.* 2016;280:890-896.

4. Ryoo HG, Lee WW, Kim JY, et al. Minimum Standardized Uptake Value from Quantitative Bone Single-Photon Emission Computed Tomography/Computed Tomography for Evaluation of Femoral Head Viability in Patients with Femoral Neck Fracture. *Nucl Med Mol Imaging.* 2019;53:287-295.

5. Lee Y, Oh D, Han JH, Gong HS, Lee WW. Semiquantitative single-photon-emission computed tomography /computed tomography study to evaluate concomitant ulnar impaction syndrome in patients presenting with triangular fibrocartilage complex tears. *PLoS One.* 2020;15:e0244256.

6. Kim JY, Kim JY, Park SB, Kim C, Lee WW. A retrospective multicenter study of quantitative bone SPECT/CT to predict the surgical removal of the accessory navicular bone. *Nucl Med Commun.* 2021;42:998-1004.

7. Suh HY, Na HY, Park SY, et al. The Usefulness of Maximum Standardized Uptake Value at the Delayed Phase of Tc-99m sestamibi single-photon emission computed tomography/computed tomography for Identification of Parathyroid Adenoma and Hyperplasia. *Medicine (Baltimore).* 2020;99:e21176.

8. Park J, Bae S, Seo S, et al. Measurement of Glomerular Filtration Rate using Quantitative SPECT/CT and Deep-learning-based Kidney Segmentation. *Sci Rep.* 2019;9:4223.

9. Kang YK, Park S, Suh MS, Byun SS, Chae DW, Lee WW. Quantitative

Single-Photon Emission Computed Tomography/Computed Tomography for Glomerular Filtration Rate Measurement. *Nucl Med Mol Imaging.* 2017;51:338-346.

10. Kim J, Lee H, Lee H, et al. Quantitative Single-Photon Emission Computed Tomography/Computed Tomography for Evaluation of Salivary Gland Dysfunction in Sjogren's Syndrome Patients. *Nucl Med Mol Imaging.* 2018;52:368-376.

11. Lee WW, Group KS. Clinical Applications of Technetium-99m Quantitative Single-Photon Emission Computed Tomography/Computed Tomography. *Nucl Med Mol Imaging.* 2019;53:172-181.

12. Park J, Lee JS, Oh D, Ryoo HG, Han JH, Lee WW. Quantitative salivary gland SPECT/CT using deep convolutional neural networks. *Sci Rep.* 2021;11:7842.

13. Lee H, Kim JH, Kang YK, Moon JH, So Y, Lee WW. Quantitative single-photon emission computed tomography/computed tomography for technetium pertechnetate thyroid uptake measurement. *Medicine (Baltimore).* 2016;95:e4170.

14. Kim HJ, Bang JI, Kim JY, Moon JH, So Y, Lee WW. Novel Application of Quantitative Single-Photon Emission Computed Tomography/Computed Tomography to Predict Early Response to Methimazole in Graves' Disease. *Korean J Radiol.* 2017;18:543-550.

15. Kim JY, Kim JH, Moon JH, et al. Utility of Quantitative Parameters from Single-Photon Emission Computed Tomography/Computed Tomography in Patients with Destructive Thyroiditis. *Korean J Radiol.* 2018;19:470-480.

16. Lee R, So Y, Song YS, Lee WW. Evaluation of Hot Nodules of Thyroid Gland Using Tc-99m Pertechnetate: a Novel Approach Using Quantitative Single-Photon Emission Computed Tomography/Computed Tomography. *Nucl Med Mol Imaging.* 2018;52:468-472.

17. Abadi M, Barham P, Chen J, et al. Tensorflow: A system for large-scale machine learning. Paper presented at: 12th USENIX Symposium on Operating Systems Design and Implementation, 2016; Savannah, GA, USA.

18. Chollet F, Others. Keras [Internet]. GitHub. Available from: https://github.com/fchollet/keras.

19. Cooper DS. Hyperthyroidism. *Lancet.* 2003;362:459-468.

20. Ramos CD, Zantut Wittmann DE, Etchebehere EC, Tambascia MA, Silva CA, Camargo EE. Thyroid uptake and scintigraphy using 99mTc pertechnetate: standardization in normal individuals. *Sao Paulo Med J.* 2002;120:45-48.

21. Macauley M, Shawgi M, Ali T, et al. Assessment of normal reference values for thyroid uptake of technetium-99m pertechnetate in a single centre UK population. *Nucl Med Commun.* 2018;39:834-838.

22. Giovanella L, Avram AM, Iakovou I, et al. EANM practice guideline/SNMMI procedure standard for RAIU and thyroid scintigraphy. *Eur J Nucl Med Mol Imaging.* 2019;46:2514-2525.

23. Jin M, Ahn J, Jo SG, et al. Comparison of (99m)Tc Pertechnetate Thyroid Uptake Rates by Gamma Probe and Gamma Camera Methods for Differentiating Graves' Disease and Thyroiditis. *Nucl Med Mol Imaging.* 2022;56:42-51.

24. Shi L, Onofrey JA, Liu H, Liu YH, Liu C. Deep learning-based attenuation map generation for myocardial perfusion SPECT. *Eur J Nucl Med Mol Imaging.* 2020;47:2383-2395.

25. Liu F, Jang H, Kijowski R, Zhao G, Bradshaw T, McMillan AB. A deep learning approach for (18)F-FDG PET attenuation correction. *EJNMMI Phys.* 2018;5:24.

26. Hwang D, Kim KY, Kang SK, et al. Improving the Accuracy of Simultaneously Reconstructed Activity and Attenuation Maps Using Deep Learning. *J Nucl Med.* 2018;59:1624-1629.

27. Hwang D, Kang SK, Kim KY, et al. Generation of PET Attenuation Map for Whole-Body Time-of-Flight (18)F-FDG PET/MRI Using a Deep Neural Network Trained with Simultaneously Reconstructed Activity and Attenuation Maps. *J Nucl Med.* 2019;60:1183-1189.

28. Hwang D, Kang SK, Kim KY, Choi H, Lee JS. Comparison of deep learning-based emission-only attenuation correction methods for positron emission tomography. *Eur J Nucl Med Mol Imaging.* 2022;49:1833-1842.

29. Gibson E, Giganti F, Hu Y, et al. Automatic Multi-Organ Segmentation on Abdominal CT With Dense V-Networks. *IEEE Trans Med Imaging.* 2018;37:1822-1834.

30. Liu Y, Lei Y, Fu Y, et al. CT-based multi-organ segmentation using a 3D self-attention U-net network for pancreatic radiotherapy. *Med Phys.* 2020;47:4316-4324.

31. Zhong T, Huang X, Tang F, Liang S, Deng X, Zhang Y. Boosting-based Cascaded Convolutional Neural Networks for the Segmentation of CT Organs-at-risk in Nasopharyngeal Carcinoma. *Med Phys.* 2019.

32. van Dijk LV, Van den Bosch L, Aljabar P, et al. Improving automatic delineation for head and neck organs at risk by Deep Learning Contouring. *Radiother Oncol.* 2020;142:115-123.

33. Wen X, Zhao B, Yuan M, et al. Application of Multi-Scale Fusion Attention U-Net to Segment the Thyroid Gland on Localized Computed Tomography Images for Radiotherapy. *Front Oncol.* 2022;12:844052.

34. Dong X, Wang T, Lei Y, et al. Synthetic CT generation from non-attenuation corrected PET images for whole-body PET imaging. *Phys Med Biol.* 2019;64:215016.

35. Armanious K, Kustner T, Reimold M, et al. Independent brain (18)F-FDG PET attenuation correction using a deep learning approach with Generative Adversarial Networks. *Hell J Nucl Med.* 2019;22:179-186.

36. Dong X, Lei Y, Wang T, et al. Deep learning-based attenuation correction in the absence of structural information for whole-body positron emission tomography imaging. *Phys Med Biol.* 2020;65:055011.

37. Saha K, Hoyt SC, Murray BM. Application of Chang's attenuation correction technique for single-photon emission computed tomography partial angle acquisition of Jaszczak phantom. *J Med Phys.* 2016;41:29-33.

38. Bailey DL, Willowson KP. An evidence-based review of quantitative SPECT imaging and potential clinical applications. *J Nucl Med.* 2013;54:83-89.

39. Ritt P, Vija H, Hornegger J, Kuwert T. Absolute quantification in SPECT. *Eur J Nucl Med Mol Imaging.* 2011;38 Suppl 1:S69-77.

40. Chen X, Zhou B, Xie H, et al. Direct and indirect strategies of deep-learning-based attenuation correction for general purpose and dedicated cardiac SPECT. *Eur J Nucl Med Mol Imaging.* 2022;49:3046-3060.

41. Shanbhag AD, Miller RJH, Pieszko K, et al. Deep Learning-Based Attenuation Correction Improves Diagnostic Accuracy of Cardiac SPECT. *J Nucl Med.* 2023;64:472-478.

42. Kwon K, Hwang D, Oh D, et al. CT-free quantitative SPECT for automatic evaluation of %thyroid uptake based on deep-learning. *EJNMMI Phys.* 2023;10:20.

43. Go AS, Chertow GM, Fan D, McCulloch CE, Hsu CY. Chronic kidney disease and the risks of death, cardiovascular events, and hospitalization. *N Engl J Med.* 2004;351:1296-1305.

44. Gates GF. Glomerular filtration rate: estimation from fractional renal accumulation of 99mTc-DTPA (stannous). *AJR Am J Roentgenol.* 1982;138:565-570.

45. Gates GF. Computation of glomerular filtration rate with Tc-99m DTPA: an in-house computer program. *J Nucl Med.* 1984;25:613-618.

46. Kim YI, Ha S, So Y, Lee WW, Byun SS, Kim SE. Improved measurement of the glomerular filtration rate from Tc-99m DTPA scintigraphy in patients following nephrectomy. *Eur Radiol.* 2014;24:413-422.

47. You C, Yang Q, Shan H, et al. Structurally-sensitive Multi-scale Deep Neural Network for Low-Dose CT Denoising. *IEEE Access.* 2018;6:41839-41855.

48. Leuliet T, Maxim V, Peyrin F, Sixou B. Impact of the training loss in deep learning-based CT reconstruction of bone microarchitecture. *Med Phys.* 2022;49:2952-2964.

49. Shi L, Zhang J, Toyonaga T, Shao D, Onofrey JA, Lu Y. Deep learning-based attenuation map generation with simultaneously reconstructed PET activity and attenuation and low-dose application. *Phys Med Biol.* 2023;68.

50. Odena A, Dumoulin V, Olah C. Deconvolution and Checkerboard Artifacts.

51. Radiation Dose to Patients from Radiopharmaceuticals - Addendum 3 to ICRP Publication 53. ICRP Publication 106. Ann. ICRP: ICRP; 2008.

52. European guideliens on quality criteria for computed tomography. EUR 16262. https://www.drs.dk/guidelines/ct/quality/.

53. Kennedy JA, Israel O, Frenkel A. Directions and magnitudes of misregistration of CT attenuation-corrected myocardial perfusion studies: incidence, impact on image quality, and guidance for reregistration. *J Nucl Med.* 2009;50:1471-1478.

54. Shan H, Padole A, Homayounieh F, et al. Competitive performance of a modularized deep neural network compared to commercial algorithms for low-dose CT image reconstruction. *Nat Mach Intell.* 2019;1:269-276.

55. Zhao T, McNitt-Gray M, Ruan D. A convolutional neural network for ultra-low-dose CT denoising and emphysema screening. *Med Phys.* 2019;46:3941-3950.

56. Chen Y, Goorden MC, Beekman FJ. Convolutional neural network based attenuation correction for(123)I-FP-CIT SPECT with focused striatum imaging. *Phys Med Biol.* 2021;66.

57. Chen Y, Goorden MC, Beekman FJ. Automatic attenuation map estimation from SPECT data only for brain perfusion scans using convolutional neural networks. *Phys Med Biol.* 2021;66:065006.

58. Du Y, Shang J, Sun J, et al. Deep-learning-based estimation of attenuation map improves attenuation correction performance over direct attenuation estimation for myocardial perfusion SPECT. *J Nucl Cardiol.* 2023;30:1022-1037.

59. Toyonaga T, Shao D, Shi L, et al. Deep learning-based attenuation correction for whole-body PET - a multi-tracer study with (18)F-FDG, (68) Ga-DOTATATE, and (18)F-Fluciclovine. *Eur J Nucl Med Mol Imaging.* 2022;49:3086-3097.

60. Rezaei A, Deroose CM, Vahle T, Boada F, Nuyts J. Joint Reconstruction

of Activity and Attenuation in Time-of-Flight PET: A Quantitative Analysis. *J Nucl Med.* 2018;59:1630-1635.

61. Mazzaferri EL, Jhiang SM. Long-term impact of initial surgical and medical therapy on papillary and follicular thyroid cancer. *Am J Med.* 1994;97:418-428.

62. Avram AM, Giovanella L, Greenspan B, et al. SNMMI Procedure Standard/EANM Practice Guideline for Nuclear Medicine Evaluation and Therapy of Differentiated Thyroid Cancer: Abbreviated Version. *J Nucl Med.* 2022;63:15N-35N.

63. Benua RS, Cicale NR, Sonenberg M, Rawson RW. The relation of radioiodine dosimetry to results and complications in the treatment of metastatic thyroid cancer. *Am J Roentgenol Radium Ther Nucl Med.* 1962;87:171-182.

64. Dorn R, Kopp J, Vogt H, Heidenreich P, Carroll RG, Gulec SA. Dosimetry-guided radioactive iodine treatment in patients with metastatic differentiated thyroid cancer: largest safe dose using a risk-adapted approach. *J Nucl Med.* 2003;44:451-456.

65. Van Nostrand D, Atkins F, Yeganeh F, Acio E, Bursaw R, Wartofsky L. Dosimetrically determined doses of radioiodine for the treatment of metastatic thyroid carcinoma. *Thyroid.* 2002;12:121-134.

66. Lassmann M, Hanscheid H, Chiesa C, et al. EANM Dosimetry Committee series on standard operational procedures for pre-therapeutic dosimetry I: blood and bone marrow dosimetry in differentiated thyroid cancer therapy. *Eur J Nucl Med Mol Imaging.* 2008;35:1405-1412.

67. Verburg FA, Hanscheid H, Biko J, et al. Dosimetry-guided high-activity (131)I therapy in patients with advanced differentiated thyroid carcinoma: initial experience. *Eur J Nucl Med Mol Imaging.* 2010;37:896-903.

68. Haugen BR, Alexander EK, Bible KC, et al. 2015 American Thyroid Association Management Guidelines for Adult Patients with Thyroid Nodules and Differentiated Thyroid Cancer: The American Thyroid Association Guidelines Task Force on Thyroid Nodules and Differentiated Thyroid Cancer. *Thyroid.* 2016;26:1-133.

69. Fugazzola L, Elisei R, Fuhrer D, et al. 2019 European Thyroid Association Guidelines for the Treatment and Follow-Up of Advanced Radioiodine-Refractory Thyroid Cancer. *Eur Thyroid J.* 2019;8:227-245.

70. Lee WW, Song YS, So Y. Quantitative Iodine-123 single-photon emission computed tomography/computed tomography for Iodine-131 therapy of an autonomously functioning thyroid nodule. *Eur J Hybrid Imaging.* 2023;7:4.

71. Oh D, Kim J-H, Yoo J, Kwon K, Lee WW. I-131 radioiodine blood activity measurement using quantitative SPECT/CT versus blood sample gamma counting in pre-therapeutic dosimetry for thyroid cancer. *J Nucl Med.* 2024;65 (supplement 2) 241854.

72. Schneider W, Bortfeld T, Schlegel W. Correlation between CT numbers and tissue parameters needed for Monte Carlo simulations of clinical dose distributions. *Phys Med Biol.* 2000;45:459-478.

73. Lassmann M, Reiners C, Luster M. Dosimetry and thyroid cancer: the individual dosage of radioiodine. *Endocr Relat Cancer.* 2010;17:R161-172.

74. Schlesinger T, Flower MA, McCready VR. Radiation dose assessments in radioiodine (131I) therapy. 1. The necessity for in vivo quantitation and dosimetry in the treatment of carcinoma of the thyroid. *Radiother Oncol.* 1989;14:35-41.

75. Maxon HR, Thomas SR, Hertzberg VS, et al. Relation between effective radiation dose and outcome of radioiodine therapy for thyroid cancer. *N Engl J Med.* 1983;309:937-941.

76. Freudenberg LS, Jentzen W, Gorges R, et al. 124I-PET dosimetry in advanced differentiated thyroid cancer: therapeutic impact. *Nuklearmedizin.* 2007;46:121-128.

77. Avram AM, Dewaraja YK. Thyroid Cancer Radiotheragnostics: the case for activity adjusted (131)I therapy. *Clin Transl Imaging.* 2018;6:335-346.

78. O'Donoghue J, Zanzonico P, Humm J, Kesner A. Dosimetry in Radiopharmaceutical Therapy. *J Nucl Med.* 2022;63:1467-1474.

79. Yamamoto Y, Nishiyama Y, Monden T, Matsumura Y, Satoh K, Ohkawa M. Clinical usefulness of fusion of 131I SPECT and CT images in patients with differentiated thyroid carcinoma. *J Nucl Med.* 2003;44:1905-1910.

80. Chen L, Luo Q, Shen Y, et al. Incremental value of 131I SPECT/CT in the management of patients with differentiated thyroid carcinoma. *J Nucl Med.* 2008;49:1952-1957.

81. Wong KK, Zarzhevsky N, Cahill JM, Frey KA, Avram AM. Incremental value of diagnostic 131I SPECT/CT fusion imaging in the evaluation of differentiated thyroid carcinoma. *AJR Am J Roentgenol.* 2008;191:1785-1794.

82. Schmidt D, Szikszai A, Linke R, Bautz W, Kuwert T. Impact of 131I SPECT/spiral CT on nodal staging of differentiated thyroid carcinoma at the first radioablation. *J Nucl Med.* 2009;50:18-23.

83. Spanu A, Solinas ME, Chessa F, Sanna D, Nuvoli S, Madeddu G. 131I SPECT/CT in the follow-up of differentiated thyroid carcinoma: incremental value versus planar imaging. *J Nucl Med.* 2009;50:184-190.

84. Schmidt D, Linke R, Uder M, Kuwert T. Five months' follow-up of patients with and without iodine-positive lymph node metastases of thyroid carcinoma as disclosed by (131)I-SPECT/CT at the first radioablation. *Eur J Nucl Med Mol Imaging.* 2010;37:699-705.

85. Wong KK, Sisson JC, Koral KF, Frey KA, Avram AM. Staging of differentiated thyroid carcinoma using diagnostic 131I SPECT/CT. *AJR Am J Roentgenol.* 2010;195:730-736.

86. Hassan FU, Mohan HK. Clinical Utility of SPECT/CT Imaging Post-Radioiodine Therapy: Does It Enhance Patient Management in Thyroid Cancer? *Eur Thyroid J.* 2015;4:239-245.

국 문 초 록

서론: 단일 광자 방출 전산화 단층촬영/전산화 단층촬영(SPECT/CT)은 생체 내 방사능 정량화와 종양 선량 평가에 있어 유망한 핵의학 영상 도구입니다. 최근 SPECT/CT 기술의 발전으로 인해 %섭취율, 표준 섭취 값, 방사능 농도(μCi/g)의 높은 정확도와 신뢰도 있는 측정이 가능해졌습니다. 이러한 매개변수는 진단과 치료 모두에서 중요한 역할을 합니다. 본 연구에서는 두 가지 진단 연구와 한 가지 I-131 관련 치료 연구를 소개합니다. 진단 연구는 심층 학습 기반 감쇠 보정(AC)과 장기 분할(OS)에 초점을 맞추었으며, 치료 연구는 방사성 요오드 치료(RAI)의 개인 맞춤형 치료 계획을 가능하게 하는 것을 목표로 합니다.

방법 및 결과: 갑상선 SPECT/CT 데이터를 활용하여 합성 감쇠 지도(μ-map)를 생성하고 자동 갑상선 분할을 가능하게 하는 네트워크를 개발하였습니다. μ-map 생성을 위해 주 방출 SPECT 와 산란 SPECT 를 훈련 데이터로 사용하였고, 생성된 μ-map 과 주 방출 SPECT 를 활용하여 자동 갑상선 분할을 수행하였습니다. 기능성 갑상선 질환 평가의 핵심 지표인 갑상선 %섭취율은 CT 없이 주 방출 SPECT 와 산란 SPECT 만으로 도출되었으며, 이를 통해 CT-free SPECT 를 실현하였습니다. 두 번째 부분에서는 신장 SPECT/CT 에서 CT-free SPECT 의 AC 과정을 최적화하였습니다. 성능 향상을 위해 로그 최대 정규화, 그래디언트 차 손실 최적화, 최 근접 인접 보간법을 도입하였습니다. 마지막으로, I-131 치료 전 SPECT/CT 를 조사하였습니다. SPECT/CT 로 측정한 혈액 내 I-131 방사능은 혈액 샘플 감마 카운팅과 높은 상관관계를 보였으며, 몬테카를로 시뮬레이션으로 도출한 혈액 흡수 선량은 기존 방법과 유사한 경향을 나타냈습니다. 종양의 I-131 방사능 농도는 직접 흡수선량률로 변환되었습니다. 이에 따라 SPECT/CT 를 기반으로 한 RAI 치료 전 계획이 유망한 가능성을 보여주었습니다.

결론: SPECT/CT 는 생체 내 방사능 정량화를 위한 신뢰할 수 있는 정확한 영상 기법입니다. 심층 학습 기반 CT-free SPECT 는 환자의 불필요한 방사선 노출을 줄이는 진단적 접근법으로서 가능성을 지니고 있습니다. 또한, 치료 전 SPECT/CT 는 진행성 갑상선 암의 RAI 치료 효능에 대한 귀중한 통찰을 제공할 수 있습니다.

주요어: 정량적 SPECT/CT, 심층 학습, 합성 μ-map, 감쇠 보정, 장기 분할, I-131 치료, 종양 흡수 선량

학 번: 2021-33651